

THE UNIVERSITY OF CALGARY

Design, Construction, and Evaluation  
of an  
Omegatron Mass Spectrometer

by

Peter Vjekoslav Amerl

A DISSERTATION

SUBMITTED TO THE FACULTY OF GRADUATE STUDIES  
IN PARTIAL FULFILLMENT OF THE REQUIREMENTS FOR THE  
DEGREE OF DOCTOR OF PHILOSOPHY

DEPARTMENT OF PHYSICS AND ASTRONOMY

CALGARY, ALBERTA

July, 1998

© Peter Vjekoslav Amerl 1998



National Library  
of Canada

Acquisitions and  
Bibliographic Services

395 Wellington Street  
Ottawa ON K1A 0N4  
Canada

Bibliothèque nationale  
du Canada

Acquisitions et  
services bibliographiques

395, rue Wellington  
Ottawa ON K1A 0N4  
Canada

*Your file Votre référence*

*Our file Notre référence*

The author has granted a non-exclusive licence allowing the National Library of Canada to reproduce, loan, distribute or sell copies of this thesis in microform, paper or electronic formats.

The author retains ownership of the copyright in this thesis. Neither the thesis nor substantial extracts from it may be printed or otherwise reproduced without the author's permission.

L'auteur a accordé une licence non exclusive permettant à la Bibliothèque nationale du Canada de reproduire, prêter, distribuer ou vendre des copies de cette thèse sous la forme de microfiche/film, de reproduction sur papier ou sur format électronique.

L'auteur conserve la propriété du droit d'auteur qui protège cette thèse. Ni la thèse ni des extraits substantiels de celle-ci ne doivent être imprimés ou autrement reproduits sans son autorisation.

0-612-34655-2

## Abstract

An omegatron mass spectrometer was designed and constructed using an electromagnet that was obsolete to nuclear magnetic resonance (NMR) investigations. The design of the analytical region differs from any published and consists of “long” rectangular plates with the detector positioned in the plane midway between them. There are no end plates or guard rings. In contrast to previous instruments, superior electronics included an integrating transimpedance amplifier for ion current measurement, a crystal controlled electron emission filament power regulator, a radio frequency driver, and a computer interface. To acquire data, a computer program that allows real-time interaction with and display of data from the instrument was written. Theoretical modelling of ion beam motion included ion-ion and ion-neutral interactions with gases in the analyzer region and an approximation for electric field distortions by the central ionizing electron beam. Numerically computed peak shapes and mass spectra were found to be consistent with those realized by the instrument. Tests using  $H_2$ , Ne, Ar, Kr, and Xe show that the instrument performance agrees with theory. The peaks corresponding to the stable isotopes of all these gases were resolved. The resolution of 6300 obtained at mass 3 can be exceeded. An exciting development was the formation and detection of  $KrH^+$ . Surprisingly, numerical calculations indicate that approximately 40 % of the  $Kr$  reacted with hydrogen to form  $KrH^+$ . Similarly an extremely high ratio (2:1) was observed for the  $H_3^+$ :  $HD^+$  doublet when analysing  $H_2$  in contrast to 1:10 in a typical sector mass spectrometer. Thus the omegatron appears to provide an environment which promotes hydride ion formation.

## Acknowledgements

I would like to thank Dr. Krouse for his guidance, support, patience, and the numerous helpful discussions over the past four years. Professor Stan Halas (UMCS, Lublin, Poland) is thanked for the expertise he brought and the companionship he provided during the reconstruction of the omegatron. Jesusa Pontoy-Overend, Maria Mihailescu, Nenita Lozano, and Henry Ling cheerfully helped with matters of sample preparation. Horst Fichtner was a great help in finding a good integration algorithm and for the quick equipotential calculations. Pat Irwin was integral to the development of the electronic equipment. Dr. Ranga Sreenivasan, Maurice Shevalier, Alfredo Louro, and Wolfram Neutsch helped with numerous discussions regarding the physics that occur in the omegatron. Kaare Berg helped with the installation of the fibre-optic data acquisition interface. The machinists in the Faculty Workshop are thanked for the excellent work that was done in the construction of the omegatron. Anyone else who had a hand in this work or lent a sympathetic ear during times that instrument problems and lightning storms were hindering progress is thanked gratefully.

# Dedication

This work is dedicated

To my parents for their continued support throughout my all too long Ph.D.  
Some say that it should have lasted only a year and a half. ;-)

To Marie, who patiently waited for days and suffered arctic like conditions in the  
laboratory while I was calling out, "...just five more minutes..."

Thank you for your help and understanding.

I hope that now I will again see the light of day and the colours of nature.

# Table of Contents

<b>Approval Page</b>	<b>ii</b>
<b>Abstract</b>	<b>iii</b>
<b>Acknowledgements</b>	<b>iv</b>
<b>Dedication</b>	<b>v</b>
<b>Table of Contents</b>	<b>vi</b>
<b>1 Introduction</b>	<b>1</b>
<b>2 Isotope Basics</b>	<b>4</b>
<b>3 Ion Motion In Electric and Magnetic Fields</b>	<b>8</b>
3.1 Ions in Magnetic Fields . . . . .	8
3.2 Ions in Electric Fields . . . . .	10
3.3 Ions in Electric and Magnetic Fields . . . . .	11
3.3.1 Oscillating Electric Fields . . . . .	13
3.3.2 Damped Harmonic Motion . . . . .	19
3.4 The Electric Potential Field . . . . .	23
<b>4 Instrumentation</b>	<b>28</b>
4.1 Key Components of a Mass Spectrometer . . . . .	28
4.1.1 The Source . . . . .	30
4.1.2 The Analyzer . . . . .	33
4.1.3 The Collector . . . . .	35
4.2 Dynamic Measurements using a Magnetic Sector Mass Spectrometer .	37
4.3 Previous Designs for Omegatrons . . . . .	38
4.4 Construction and Design of the Current Omegatron . . . . .	40
4.4.1 The Vacuum Chamber and Suspension Arm . . . . .	41
4.4.2 The Omegatron Interior . . . . .	45
4.5 Data Acquisition and Signal Generation . . . . .	51
4.5.1 Filament Power Regulation . . . . .	52
4.5.2 The Radio Frequency Driver . . . . .	53
4.5.3 Ion Current Amplification . . . . .	55

<b>5</b>	<b>Numerical Models</b>	<b>59</b>
5.1	Methods of Solving Ordinary Differential Equations . . . . .	59
5.2	Particle Trajectories . . . . .	61
5.2.1	Ion Trajectories in a Parallel Plate Capacitor . . . . .	61
5.2.2	Ion Trajectories in a Parallel Plate Capacitor with a Central Electron Beam . . . . .	63
5.2.3	Ion Trajectories in a Parallel Plate Capacitor with a Central Electron Beam and Long Range Forces damping the ion Motion	65
5.3	Theoretical Spectra . . . . .	67
5.4	Realistic Electric Potential Fields . . . . .	74
<b>6</b>	<b>Obtaining and Analysing Omegatron Spectra</b>	<b>79</b>
6.1	Alignment with the Magnetic Field . . . . .	79
6.2	Reducing Ion Loss due to Motion Parallel to the Magnetic Field . . .	80
6.3	Reducing Space Charge Effects . . . . .	80
6.4	Data Acquisition Procedure . . . . .	81
6.5	Data Analysis . . . . .	83
<b>7</b>	<b>Results and Discussion</b>	<b>87</b>
7.1	Performance Limitations Imposed by the Quality of the Components and Other Phenomena . . . . .	87
7.2	Resolution of $H_3^+$ and $HD^+$ . . . . .	90
7.3	Mass Spectra of Noble Gases . . . . .	93
7.3.1	Neon . . . . .	93
7.3.2	Argon . . . . .	96
7.3.3	Krypton . . . . .	98
7.3.4	Xenon . . . . .	101
7.4	Formation of $KrH^+$ . . . . .	101
<b>8</b>	<b>Conclusions and Future Possibilities</b>	<b>106</b>
	<b>Bibliography</b>	<b>112</b>
<b>A</b>	<b>Software Interface for the Omegatron.</b>	<b>121</b>
A.1	Calculating Omegatron Frequencies . . . . .	121
A.2	Controlling The Omegatron . . . . .	122
<b>B</b>	<b>Circuit Diagrams</b>	<b>132</b>
<b>C</b>	<b>Conference Presentations and Abstracts based on this Thesis</b>	<b>137</b>

## List of Tables

2.1	Stable isotopic abundance data in % for the noble gases as published in the 1993-1994 CRC Handbook of Chemistry and Physics [22] . . .	7
4.1	Summary of the most important features of previous and current omegatron designs. RECT indicates whether the analyser is rectangular, MDPD indicates that the detector is located in the mid plane between the RF plates, SS-RF indicates that a single-sided radio frequency signal is used and one RF plate is grounded, GRG indicates the use of guard rings, and HARM indicates that the design suffered from harmonic effects. Max R, and max B show the maximum radius of curvature and the maximum magnetic flux density that were possible with the instruments. Entries labelled NA indicate that the information was not available. . . . .	41
5.1	Integration parameters for the omegatron modeled as an ideal parallel plate capacitor. . . . .	62
5.2	Integration parameters for the omegatron modelled as an ideal parallel plate capacitor with a column of charge at the origin, representing the electron beam. . . . .	64
5.3	Integration parameters for the omegatron modelled as an ideal parallel plate capacitor with a column of charge at the origin, representing the electron beam and a damping term. . . . .	66



## List of Figures

3.1	The electric field configuration for an infinite parallel plate capacitor with a magnetic field aligned parallel with the plates. . . . .	14
3.2	Graph of the time evolution of the x and y components of the particle velocity as given by equations 3.31 and 3.32. . . . .	16
3.3	Phase space plot of the velocity-trajectory of a particle with a velocity given by equations 3.31 and 3.32. . . . .	17
3.4	Graph of the time evolution of the x and y components of displacement, shown in equations 3.33 and 3.34. . . . .	17
3.5	Plot of the trajectory of a particle with a velocity given by equations 3.33 and 3.34. . . . .	18
3.6	Graph of the velocity space trajectory of particles that are accelerated by an oscillating electric field perpendicular to a static magnetic field. At higher velocities, long range interactions with the background gas reduce the net acceleration that the particles experience. . . . .	22
3.7	Cross-section through the equipotential surfaces within an ideal parallel plate capacitor. A and B are the top and bottom plates. Plate A is at a potential of +10 volts while plate B is at a potential of -10 volts. The potential surfaces are labelled with their respective potentials. . .	25
4.1	Simplified Diagram of a typical 90° magnetic sector mass spectrometer with a triple collector. . . . .	29
4.2	A solid source triple filament assembly. The center filament is loaded with a sample. . . . .	31
4.3	An electron impact source . . . . .	32
4.4	Creation of a sector mass spectrometer peak. The beam moves across the slit because the mass spectrometer is used in its scanning configuration. Either the magnetic field is varied, or the energy of the ions is changed to affect a change in the ion trajectories. . . . .	34
4.5	Cross sectional view of the omegatron mass spectrometer vacuum chamber. . . . .	42
4.6	Side view of the omegatron mass spectrometer vacuum chamber. . . .	43
4.7	Suspension arm with the vacuum chamber attached, showing the rotational degrees of freedom. . . . .	44
4.8	Photograph of the “old” omegatron design. . . . .	46
4.9	Photograph of the current omegatron design showing the position of the parallel RF plates and the filament holder on the top. . . . .	47

4.10	Photograph of the current omegatron design showing the position of the detector. . . . .	48
4.11	Diagram of the omegatron as was used for the measurements acquired for this work and shown in later chapters. . . . .	49
4.12	Schematic diagram of the electronics used to operate the omegatron. The abbreviations EEFS, OSC, MS I/O stand for the electron emission filament power regulator, the synthesized frequency generator, and the mass spectrometry interface board respectively. . . . .	52
4.13	Schematic diagram of the filament power regulator. Electron emission is regulated by controlling the filament temperature through a phase comparison of the frequency converted trap current, and an adjustable frequency reference. . . . .	53
4.14	Block diagram of the RF-Driver that generates a ground-isolated push-pull signal from the ground referenced signal provided by the signal generator . . . . .	54
4.15	Circuit diagram of the amplifier configuration used for conventional mass spectrometers. . . . .	55
4.16	Operational schematic diagram of the IVC102 integrating transimpedance amplifier. . . . .	57
5.1	Trajectory of a resonant particle in the omegatron modelled as an ideal parallel plate capacitor. . . . .	62
5.2	Trajectory of a resonant particle in the omegatron modelled as an ideal parallel plate capacitor with a column of charge at the origin of the x-y plane and aligned along the z-direction, representing the electron beam. . . . .	64
5.3	Trajectory of a resonant particle in the omegatron modelled as an ideal parallel plate capacitor with a column of charge aligned along the z-direction, representing the electron beam at the origin of the x-y plane. Drag forces from ion-ion and ion-neutral interactions result in smaller changes of the radius at higher ion speeds (greater radii). . .	66
5.4	Graph showing the path length as a function of the applied angular frequency. Comparison of the ideal ppc in red, the ppc with the column of charge shown in green, and the ppc with the column of charge and the damping term in yellow. . . . .	68
5.5	Probability of particles reaching the detector as a function of the applied angular frequency for a mean-free path that is 20% of the minimum path length. Comparison of the ideal ppc, the ppc with the column of charge, and the ppc with the column of charge and the damping term. . . . .	70

5.6	Normalized probability of particles reaching the detector as a function of the applied angular frequency for a mean-free path that is 20% of the minimum path length. Comparison of the ideal ppc, the ppc with the column of charge, and the ppc with the column of charge and the damping term. . . . .	71
5.7	Probability of particles reaching the detector as a function of the applied angular frequency for a mean-free path that is 100% of the minimum path length. Comparison of the ideal ppc, the ppc with the column of charge, and the ppc with the column of charge and the damping term. . . . .	72
5.8	Normalized probability of particles reaching the detector as a function of the applied angular frequency for a mean-free path that is 100% of the minimum path length. Comparison of the ideal ppc, the ppc with the column of charge, and the ppc with the column of charge and the damping term. . . . .	73
5.9	Contour plot of a cross section of the equipotential planes inside a finite three dimensional omegatron. The presence of the detector mount and the detector between the RF-plates (right side of top view), strongly distorts the equipotential planes. The numbers shown reflect the potential ( $V$ ). . . . .	77
5.10	Contour plot of the equipotential planes inside a finite three dimensional omegatron. A smaller detector mount on the right side of the top view, results in the field geometry approaching that of the ideal omegatron. The non-linear distribution of the fields due to the finite extent did not change. The numbers shown reflect the potential ( $V$ ). . . . .	78
6.1	Flow chart showing the interaction and data flow paths between the acquisition, the real-time control, and the display update threads. . .	82
6.2	Diagram of successive frequency scans during the acquisition of a neon spectrum. Starting from the left, the peaks are $^{22}\text{Ne}$ , $^{21}\text{Ne}$ , and $^{20}\text{Ne}$	83
6.3	Diagram of the approximate peak shape. Calculation of the peak-area involves consistently defining the background and tail regions. . . .	85
7.1	Plot of the $H_3^+$ and $HD^+$ mass peaks resolved by the omegatron with a magnetic flux density of approximately 1.12 T and a radio frequency accelerating electric field of 125 V/m. . . . .	91
7.2	Example of the frequency shift observed due to a slow drift of the magnetic field for $H_3^+$ and $HD^+$ peaks. . . . .	92

7.3	Neon isotope spectrum. All three stable isotopes are visible even though the $^{21}\text{Ne}^+$ peak almost vanishes in the background, and the peaks are asymmetric. . . . .	94
7.4	Semi-logarithmic graph of the neon spectrum shown in Figure 7.3. Here the $^{21}\text{Ne}^+$ peak is clearly visible. . . . .	95
7.5	Mass spectrum of Argon. Only the dominant $^{40}\text{Ar}$ peak is clearly visible for the particular instrumental settings. . . . .	96
7.6	Semi-logarithmic graph of the argon spectrum shown in Figure 7.5. The $^{36}\text{Ar}^+$ peak is barely visible. . . . .	97
7.7	Krypton isotope spectrum measured with an ion collector distance of 1.3 cm from the electron beam. The peak tops are rounded and the sides rise rapidly. . . . .	98
7.8	Krypton isotope spectrum with the ion collector at a distance of 1.8 cm from the electron beam. Sharp peak tops with smoothly rising sides are observed. . . . .	99
7.9	Semi-logarithmic graph of the krypton isotope spectrum shown in Figure 7.7. The change in scale, allows the identification of the $^{78}\text{Kr}$ mass peak. . . . .	100
7.10	Xenon isotope spectrum. At high magnetic flux densities (1.12 T) and low acceleration potentials the Xenon isotopes are almost completely resolved. . . . .	101
7.11	Spectrum observed after admitting krypton gas that contained some water vapour into the sample storage bellows and vacuum chamber that previously contained hydrogen gas. The additional peaks that occur one atomic mass unit higher than the krypton isotopes suggest that this mass spectrum most likely corresponds to a mixture of $\text{Kr}^+$ and $\text{KrH}^+$ . . . . .	102
7.12	Comparison of $\text{Kr}^+$ and $\text{KrH}^+$ spectra. The spectrum in blue corresponds to the mixture of $\text{Kr}^+$ and $\text{KrH}^+$ ions. The spectrum in purple is that of $\text{Kr}^+$ obtained earlier. The peaks coloured in green were obtained by assuming that 40% of the Kr reacted with the $\text{H}_2$ and subtracting this contribution from the spectrum of the mixture. . . . .	104
A.1	The omegatron frequency and mass calculator. . . . .	122
A.2	Data acquisition program just after it has been started. . . . .	123
A.3	Starting the initialization of the data acquisition procedure. . . . .	124
A.4	Display of the dialog box that allows the selection of a manually configured data acquisition procedure, or a previously stored acquisition procedure. . . . .	125

A.5	Selecting the initialization file from the available files. If the file does not exist (manual configuration), it will be created. . . . .	126
A.6	Specification of the number of frequency ranges. If the same frequency range is to be scanned repeatedly three times, the range should be entered as three regions. . . . .	127
A.7	The starting and end frequencies, the frequency step size, amplitude, and other parameters for one frequency sweep are entered using this dialog box. . . . .	128
A.8	To start a data acquisition, the Data Acquisition option must be selected from the file menu. . . . .	129
A.9	Control panel that allows direct control of the omegatron. During a data acquisition sequence, the user may intervene to halt the program, abort a segment, or change the voltage to frequency converter gain. .	130
A.10	View of the program as it acquires data. The progress bar shows the current frequency location relative to the end points of the frequency scan. . . . .	131
B.1	Schematic diagram of the integrating transimpedance amplifier with a sample-and-hold circuit to give a continuous voltage output. . . .	132
B.2	Switch timing circuit for the integrating transimpedance amplifier. . .	133
B.3	Electron emission current controller . . . . .	134
B.4	Feedback signal conditioner for the electron emission supply. . . . .	135
B.5	Radio frequency driver schematic diagram . . . . .	136

# Chapter 1

## Introduction

Human nature encompasses the desire to understand the forces that shape the universe. To gain this understanding, humanity has explored and developed methods to learn more. One method among millions is measurement of the isotope composition of noble gases. These data can be used to trace ground water flow [1], study magmatic processes [2], [3], metamorphic events [4] and processes in oil and gas reservoirs [5]. Noble gas isotope analysis of meteorites provide information on the history of our solar system and cosmic ray reactions [6]

The above applications have one common requirement, the need for precise and accurate instruments for the measurement of isotopic abundance ratios. The work presented in this dissertation, re-introduces the Omegatron developed by Hipple, Sommer, and Thomas in 1949 [7] as a chemical composition and an isotope abundance measurement mass spectrometer. In the 1960's, omegatrons were used to determine residual gases in vacuum tubes and ion pumps [8], [9], [10], [11] and [12]. Ions up to 50 atomic mass units were successfully resolved, collected, and recorded. In 1963, Bloom *et.al.* [13] compared an omegatron with a 90°sector-type mass spectrometer. Although the ion current of the omegatron was orders of magnitude smaller, its resolution surpassed the sector instrument for low masses. The omegatron excelled by better resolving the isotopes of krypton with the same magnetic flux density and physical size comparable to the sector instrument.

In this Thesis, differences between the omegatron and the commonly used mag-

netic sector mass spectrometer are described and techniques for the creation of ions common to both types of instruments are outlined. A simple omegatron, similar to that used by van der Waal [10] has been constructed using 316 grade stainless steel and ceramic insulating components. Currently, the maximum radius of curvature for the ion trajectories is 2 cm. This is over twice the radius previously used in similar instruments. The instrument is housed in a bakeable stainless steel vacuum-tight enclosure that has two rotational axes that allow the accurate alignment of the omegatron with the magnetic field. The magnetic field is generated by a 30.5 cm diameter electromagnet with pole pieces that are separated by 6.4 cm. It can produce a maximum magnetic flux density of 1.2 tesla. Under these conditions, the maximum resolution of the new instrument should be approximately an order of magnitude greater than that of the omegatron of Sommer *et. al.* in 1951 [14].

Electric equipotential lines are mapped and numerical calculations for ion trajectories presented for (1) the ideal parallel plate capacitor model of the omegatron (2) an ideal parallel plate capacitor with a central column of charge, representing the electron beam that ionizes the gas sample and (3) an ideal parallel plate capacitor that includes both an electron beam and drag due to interactions among neutral atoms, molecules, and ions. The calculations are used to find the path length of ions undergoing acceleration in a RF electric field over a range of frequencies. The path lengths are then used to calculate a peak shape.

Mass spectra for  $H_2$ , neon, argon, krypton, and xenon were obtained. All isotopes of the noble gases up to xenon were resolved. The inverse mass dependence of the resolution gives this instrument the advantage of being capable of resolving the  $HD^+$  and  $H_3^+$  doublet by increasing the magnetic flux density and decreasing the

RF acceleration field.

There is strong evidence for  $KrH^+$  formation in a gas mixture of  $Kr$ ,  $H_2$ , and possibly water vapour inside the operating omegatron. A model whereby 40% of the krypton combines with hydrogen, has been used to reconstruct a pure krypton spectrum with good accuracy from that of the  $KrH^+$  -  $Kr^+$  mixture.



## Chapter 2

### Isotope Basics

The word isotope comes from the two Greek words *isos* *topos*, meaning **the same place** [15]. The place that is referred to, is the location of the atom in the periodic system of the elements. The reason for this placement is that different isotopes of one element react chemically in the same manner and thus belong in the same “box” in the periodic table. Isotopes of an element have the same number of protons,  $Z$ , but different numbers of neutrons,  $N$ , in their nuclei. The atomic mass<sup>1</sup> of an atom,  $A$ , is given by the sum of the numbers of neutrons and protons.

Most of the very light isotopes and elements, such as  $^1H$ ,  $^2H$  (and some  $^4He$ ) originate from the primordial components of the universe [16]. The heavier elements, including most of the observed  $He$ , are produced by nucleosynthesis in stars [17]. The isotopes of lithium, beryllium, and boron seem to be the exception to the rule, as they are believed to form mostly from cosmic ray interactions with the lighter elements [18]. Some isotopes, such as  $^{14}C$  found on earth are formed by the interaction of high energy particles in the atmosphere [19]. Other isotopes are formed by the decay of radioactive nuclei such as isotopes of uranium, thorium, and plutonium [20].

Although it is debatable whether the basic components of this planet may have started as a homogeneous mixture of the elements and isotopes, large variations in isotope abundances of elements have been generated in geological and biological sys-

---

<sup>1</sup> Atomic masses are often specified as multiples of the atomic mass unit, *amu*, that is equivalent to  $1.66057 \times 10^{-27} kg$ . Neutrons and Protons have masses that are very close to that of the atomic mass unit.

tems. In some cases, variations resulted from radioactive decay, but most arise from mass dependent fractionation processes. Fractionation may occur as a consequence of kinetic isotope effects, where the mass difference causes the lighter isotopes to leave a reservoir (evaporate, chemically react, etc.) with a rate constant that is higher than that of the heavier ones, thus relatively depleting the reservoir of the lighter isotope. Isotope exchange reactions, whereby isotopes of an element are exchanged between two or more molecular species or states of one molecular species cause the participants to differ in isotope composition. Isotope fractionation is found in physical [21], chemical, and biological processes. For example, photo-synthetic pathways of different plant species favour the lighter isotope of carbon ( $^{12}\text{C}$ ) from atmospheric  $\text{CO}_2$  to different degrees.

Magnetic sector mass spectrometers are usually used to measure isotopic abundances of the elements. Few if any of these instruments can be free of systematic measurement errors. These errors pose potential problems with the compilation, comparison, and analysis of data acquired from different laboratories. To avoid these difficulties, a relative measurement technique has been developed. This technique requires a standard isotope abundance ratio for an element to be defined and accepted globally. For hydrogen and deuterium, the historical reference standard for the  $D/H$  ratio was defined as that for a mixture of ocean water samples known as standard-mean-ocean-water (SMOW). Since the original standard was soon exhausted, a replacement (V-SMOW) nearly identical to SMOW was prepared by the International Atomic Energy Agency in Vienna. For argon, the atmospheric  $^{40}\text{Ar}/^{36}\text{Ar}$  abundance ratio is accepted as 295.5 [2]. The isotopic ratio of an unknown sample may then be used in conjunction with the isotopic abundance ratio

of a standard to define a measurement scale insensitive to systematic instrumental errors, the del (or delta) scale,

$$\delta {}^nX = 1000 \left( \frac{\left( \frac{{}^nX}{{}^mX} \right)_{sample}}{\left( \frac{{}^nX}{{}^mX} \right)_{standard}} - 1 \right), \quad (2.1)$$

where  ${}^nX$  represents the heavier isotope and  ${}^mX$  is the lighter isotope of the element  $X$ . The unit of measurement for this scale is the per mil, ‰, which presents a difference of one part in one thousand between the ratio of the unknown and the standard. By measuring both the sample and the standard under identical conditions and expressing the data in terms of equation 2.1, systematic measurement errors are reduced. A vast array of standards for many elements have been amassed. The isotopic abundances that have been adopted for the stable noble gases, He, Ne, Ar, Kr, Xe, are given in Table 2.1.

Since the isotope abundance ratios of elements that have one or more radioactive or radiogenic isotopes change with time, this system may not be entirely suitable. For radiogenic isotopes, delta scales can be defined preferably with the abundance of a non-radiogenic isotope in the denominator. For radioactive materials, alternate schemes have been adopted.

Element	Isotope Mass	Abundance (%)
Helium	$^3\text{He}$	0.00000137
	$^4\text{He}$	99.99987
Neon	$^{20}\text{Ne}$	90.48(3)
	$^{21}\text{Ne}$	0.27(1)
	$^{22}\text{Ne}$	9.25(3)
Argon	$^{36}\text{Ar}$	0.337(3)
	$^{38}\text{Ar}$	0.063(1)
	$^{40}\text{Ar}$	99.600(3)
Krypton	$^{78}\text{Kr}$	0.35(2)
	$^{80}\text{Kr}$	2.25(2)
	$^{82}\text{Kr}$	11.60(1)
	$^{83}\text{Kr}$	11.5(1)
	$^{84}\text{Kr}$	57.0(3)
	$^{86}\text{Kr}$	17.3(2)
Xenon	$^{124}\text{Xe}$	0.10(1)
	$^{126}\text{Xe}$	0.09(1)
	$^{128}\text{Xe}$	1.91(3)
	$^{129}\text{Xe}$	26.4(6)
	$^{130}\text{Xe}$	4.1(1)
	$^{131}\text{Xe}$	21.2(4)
	$^{132}\text{Xe}$	26.8(5)
	$^{134}\text{Xe}$	10.4(2)
	$^{136}\text{Xe}$	8.9(1)

Table 2.1: Stable isotopic abundance data in % for the noble gases as published in the 1993-1994 CRC Handbook of Chemistry and Physics [22]

## Chapter 3

### Ion Motion In Electric and Magnetic Fields

The functioning of stable isotope abundance ratio mass spectrometers depend on interactions of charged particles with magnetic and electric fields. To explain the design and operation of such instruments, an overview of the underlying theory is provided. The discussion that follows will highlight important concepts that govern ion motion.

#### 3.1 Ions in Magnetic Fields

The force that ions experience in a magnetic field is given by

$$\vec{F}_{Magnetic} = q\vec{v} \times \vec{B}, \quad (3.1)$$

where  $F_{Magnetic}$  is the force that the particle experiences,  $q$  is its charge,  $\vec{v}$  is the velocity of the particle, and  $\vec{B}$  is the magnetic flux density. This force always acts perpendicular to both the ion's direction of motion and the magnetic field. Thus, the equation may be rewritten as

$$F_{\perp} = qvB \quad (3.2)$$

for  $\vec{v} \perp \vec{B}$  and implies that an ion will follow a circular path within a magnetic field. To determine the radius of curvature and the frequency of a particle's motion, the

force expression may be restated as

$$F_{\perp} = m \frac{v^2}{r}, \quad (3.3)$$

where  $m$  is the mass of the ion and  $r$  is the radius of curvature of the ions motion. Combining equations 3.2 and 3.3, it is possible to solve for the radius of curvature of the ion trajectory in terms of its speed.

$$r = \frac{mv}{qB} \quad (3.4)$$

The tangential speed of a particle moving in a circular orbit of radius  $r$ , can be expressed in terms of the angular frequency of rotation,  $\omega$ , as  $\omega = v/r$ . This allows equation 3.3 to be rewritten as

$$F_{\perp} = m\omega^2 r. \quad (3.5)$$

Substituting equation 3.5 into equation 3.2, and solving for the angular frequency,  $\omega$ , one obtains the expression for the cyclotron frequency (the natural frequency of precession) for a particle with a charge to mass ratio,  $q/m$ , located in a magnetic field  $B$ .

$$\omega_c = \frac{qB}{m} \quad (3.6)$$

A  $N_2$  molecule ( $28 \text{ amu}$ ), at a temperature of  $300 \text{ K}$  in a  $0.5 \text{ T}$  magnetic field would move on a circular path with a radius of curvature of approximately  $0.2 \text{ mm}$  and have a cyclotron frequency near  $270 \text{ kHz}$ .

### 3.2 Ions in Electric Fields

Charged particles exposed to electric fields, experience a force that is proportional to their net charge, and the electric field strength. This force is parallel or anti-parallel to the field lines depending on whether the charge is positive or negative.

$$\vec{F}_{Electric} = q\vec{E}, \quad (3.7)$$

where  $\vec{F}_{Electric}$  is the force that acts on the particle and  $\vec{E}$  is the electric field vector. The particle will experience an acceleration consistent with Newton's 2<sup>nd</sup> law of motion,

$$\vec{d}'' = \frac{\vec{F}}{m} = \frac{q\vec{E}}{m}. \quad (3.8)$$

In equation 3.8,  $\vec{d}''$ , denotes the acceleration of the particle and  $m$  its mass. Substituting the acceleration into the kinematic expression for the velocity,

$$\vec{d}' = \vec{d}'_o + \vec{d}''t, \quad (3.9)$$

where  $t$  is the time that the particle experiences the acceleration,  $\vec{d}'$  is the velocity after time  $t$ , and  $\vec{d}'_o$  is the initial velocity at time  $t_o = 0$ . Substituting equation 3.8 into 3.9 yields

$$\vec{d}' = \vec{d}'_o + \frac{q\vec{E}t}{m}. \quad (3.10)$$

Thus, the velocity of a particle in an electric field is changed only along the direction of the electric field.

### 3.3 Ions in Electric and Magnetic Fields

The motion of ions in electric and magnetic fields can be expressed by the Lorentz force [23] expression

$$\vec{F} = q\vec{E} + q\vec{v} \times \vec{B} \quad (3.11)$$

The two terms that comprise the Lorentz equation are the magnetic force from equation 3.1 and the electric force from equation 3.7.

It is convenient to separate the Lorentz force expression into its Cartesian coordinate components.

$$F_x = q(E_x + (\vec{v} \times \vec{B})_x) \quad (3.12)$$

$$F_y = q(E_y + (\vec{v} \times \vec{B})_y) \quad (3.13)$$

$$F_z = q(E_z + (\vec{v} \times \vec{B})_z) \quad (3.14)$$

To simplify the expression, one may assume that the magnetic field is pointing in the positive z-direction.

$$\vec{B} = B_z \hat{k} \quad (3.15)$$

In the case, that the electric field is aligned parallel to the magnetic field, the electric field simply accelerates the particles along the magnetic field lines. A more interesting situation arises when the applied electric field is aligned perpendicular to the magnetic field.

$$\vec{E} = E_x \hat{i} \quad (3.16)$$

These two conditions from equations 3.15 and 3.16 reduce the Lorentz force expres-



sions to

$$F_x = q(E_x + v_y B_z) \quad (3.17)$$

and

$$F_y = q(-v_x B_z). \quad (3.18)$$

The motion can now be separated into two distinct, yet simultaneous components. The first component, the oscillating part is governed by equations 3.17 and 3.18. It is useful to express this component in terms of the spatial derivatives, which are commonly used to solve numerical models. Substituting the Newtonian force expression,  $\vec{F} = m\vec{d}''$  in its component form into 3.17 and 3.18, produces the differential equations,

$$x'' = \omega_c \left( \frac{E_x}{B_z} + y' \right) \quad (3.19)$$

and

$$y'' = \omega_c (-x'). \quad (3.20)$$

The second component, the motion of the centre of mass (gyro center) is obtained by setting the left hand side of the Lorentz force equation 3.11 to zero. The remaining expression is

$$0 = \vec{E} + \vec{v} \times \vec{B}. \quad (3.21)$$

Taking the cross product with  $\vec{B}$  from the right, and using the vector identity

$$\vec{a} \times (\vec{b} \times \vec{c}) = \vec{b}(\vec{a} \cdot \vec{c}) - \vec{c}(\vec{a} \cdot \vec{b}) \quad (3.22)$$

equation 3.23 is obtained.

$$\vec{v}_D = \frac{\vec{E} \times \vec{B}}{|\vec{B}|^2} \quad (3.23)$$

This equation shows the direction and speed at which the the centre of mass of a precessing ion drifts when crossed electric and magnetic fields are present. The velocity  $\vec{v}_D$  is called the drift velocity. A striking feature of equation 3.23, is that the particle does not accelerate, rather, it moves at a constant speed in a direction perpendicular to the fields. The drift velocity is also independent of the mass and charge of the particle.

### 3.3.1 Oscillating Electric Fields

Solutions to the Lorentz equation for time dependent, oscillating electric fields show how ions gain energy. As is discussed in later chapters, the omegatron employs an alternating electric field to accelerate ions and allows those with specific charge to mass ratios to reach a detector. The discussion in this section will be limited to simple (ideal) field geometries that have exact solutions.

Let a charged particle be initially at rest between two infinite parallel plates. A magnetic field is applied parallel to the plates and an oscillating electric field exists between the two plates, as is shown in Figure 3.1.

The equations of motion of a particle located in between the plates may still be expressed by equations 3.19 and 3.20 if one expresses the electric field,  $E_x$ , in terms of its oscillatory behaviour. A sinusoidal function is choosen as these are used in the

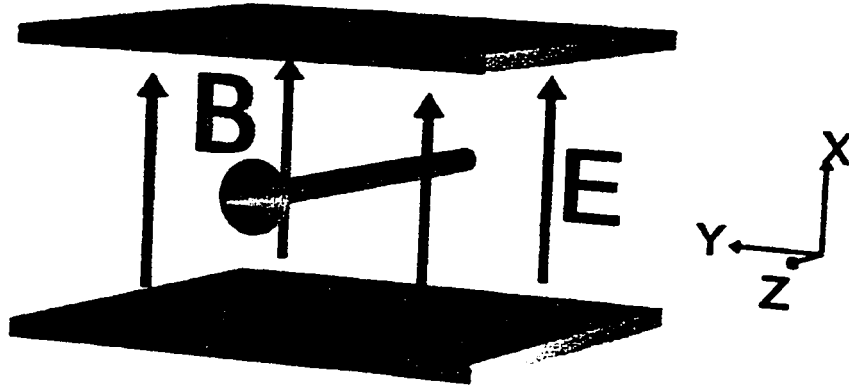


Figure 3.1: The electric field configuration for an infinite parallel plate capacitor with a magnetic field aligned parallel with the plates.

omegatron to gather data.

$$\vec{E} = E_x \hat{i} = E_o \cos(\omega t) \hat{i}. \quad (3.24)$$

Here  $E_o$  is the amplitude,  $\omega$  is the angular frequency of the electric field, and  $t$  is the time. Incorporating equation 3.24 into the equations of motion, 3.19 and 3.20, the equations of motion for forced oscillations are obtained.

$$x'' = \omega_c \left( \frac{E_o \cos(\omega t)}{B_z} + y' \right), \quad (3.25)$$

and

$$y'' = \omega_c (-x'). \quad (3.26)$$

Solutions to these equations may be obtained by differentiating equation 3.26, substituting it into equation 3.25, followed by applying the method of undetermined coefficients [24] on the resulting inhomogeneous equation. The solutions below, are

derived for the case that at  $t = 0$ ,  $y = x = y' = x' = 0$ .

$$x' = \frac{qE_o}{m} \frac{\omega_c \sin(\omega_c t) - \omega \sin(\omega t)}{\omega_c^2 - \omega^2} \quad (3.27)$$

$$y' = \frac{qE_o}{m} \frac{\omega_c (\cos(\omega_c t) - \cos(\omega t))}{\omega_c^2 - \omega^2} \quad (3.28)$$

The corresponding equations for the spatial coordinates are given by

$$x = \frac{qE_o}{m} \frac{-\cos(\omega_c t) + \cos(\omega t)}{\omega_c^2 - \omega^2} \quad (3.29)$$

and

$$y = \frac{qE_o}{m} \frac{\sin(\omega_c t) - \frac{\omega_c}{\omega} \sin(\omega t)}{\omega_c^2 - \omega^2}. \quad (3.30)$$

A mathematical limitation of equations 3.27 through 3.30 is that they are not valid expressions when the driving frequency,  $\omega$  equals the cyclotron frequency,  $\omega_c$ . Equations for the special case when the two frequencies are equal, can be derived by applying L'Hôpital's rule [25]. One obtains

$$v_x = x' = \frac{E_o}{2B} (\sin(\omega_c t) + \omega_c t \cos(\omega_c t)), \quad (3.31)$$

$$v_y = y' = \frac{qE_o}{m} t \sin(\omega_c t), \quad (3.32)$$

$$x = -\frac{E_o}{2B} t \sin(\omega_c t), \quad (3.33)$$

and

$$y = \frac{E_o}{2B} \left( \frac{\sin(\omega_c t)}{\omega_c} - t \cos(\omega_c t) \right). \quad (3.34)$$

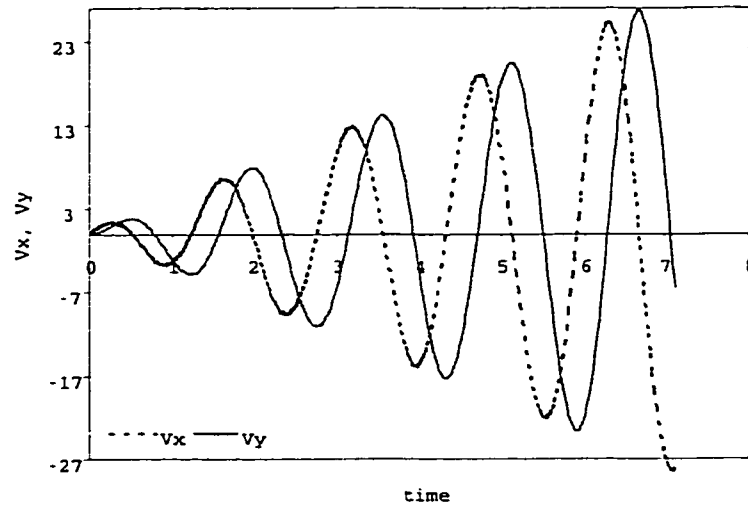


Figure 3.2: Graph of the time evolution of the x and y components of the particle velocity as given by equations 3.31 and 3.32.

The time dependence of equations 3.31 and 3.32 is shown in Figure 3.2. A constant increase in the velocities can be observed. Figure 3.3 shows the same result in velocity space. A similar behaviour is observed in the displacement. Figure 3.4 shows the time evolution of the x and y components of the displacement as described by equations 3.33 and 3.34. Figure 3.5 shows the trajectory that an initially stationary particle at the origin follows when subjected to the sinusoidally varying electric field from equation 3.24.

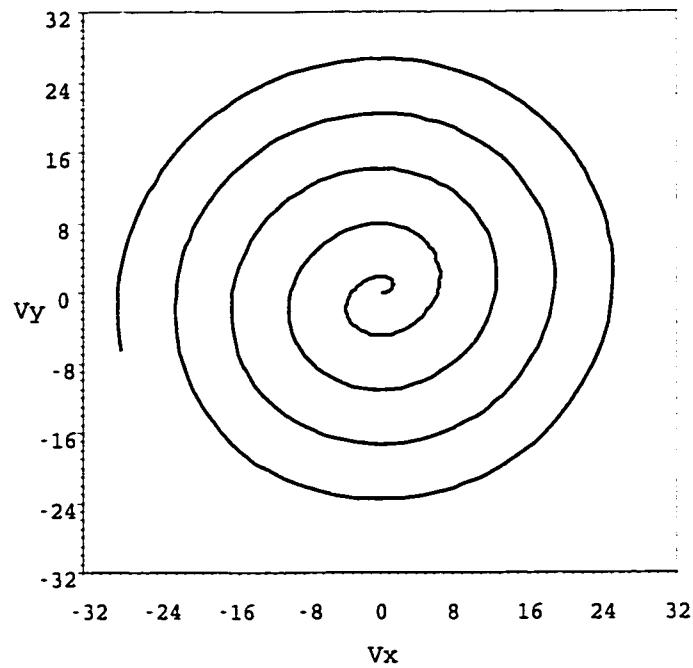


Figure 3.3: Phase space plot of the velocity-trajectory of a particle with a velocity given by equations 3.31 and 3.32.

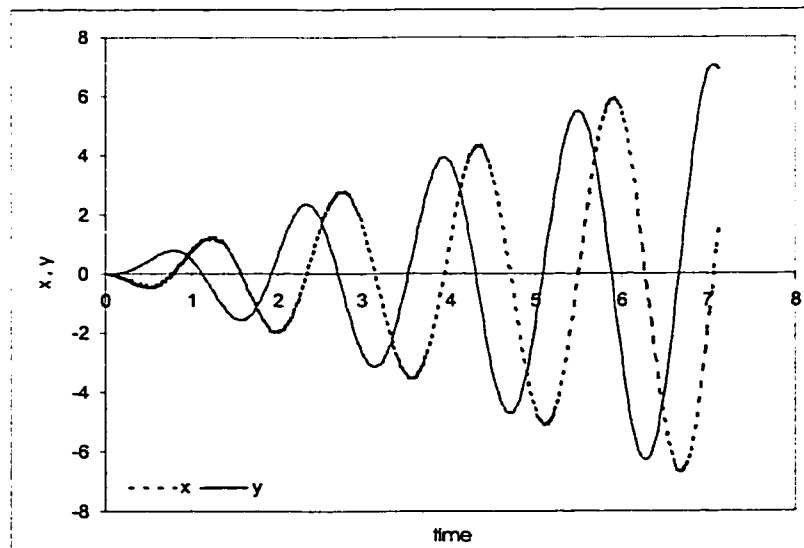


Figure 3.4: Graph of the time evolution of the  $x$  and  $y$  components of displacement, shown in equations 3.33 and 3.34.

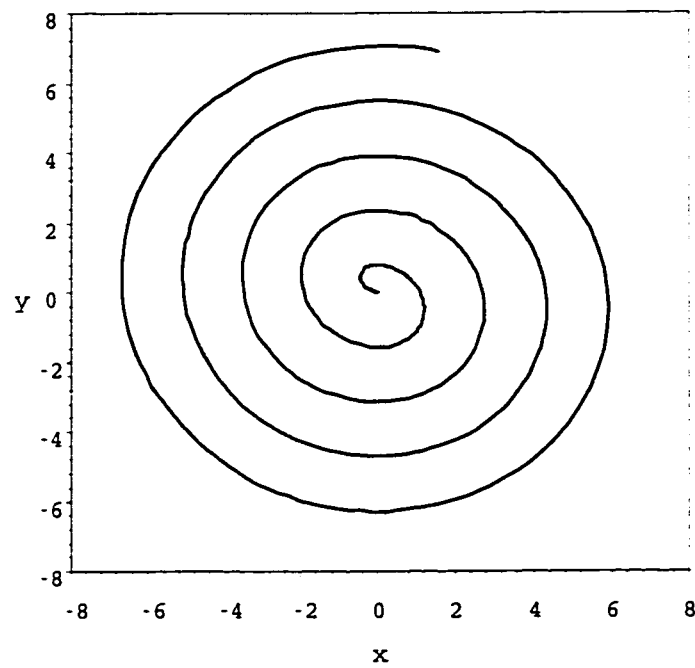


Figure 3.5: Plot of the trajectory of a particle with a velocity given by equations 3.33 and 3.34.

One finds that with these forced oscillations, the radius a particle reaches will be greater, the closer the driving frequency is to its cyclotron frequency. If driven by a frequency other than the resonance frequency, the charged particle accelerates for only a few revolutions. After that time, it lags the electric field in phase so that it experiences a decrease in acceleration resulting from the phase difference between its motion and the electric field. This behaviour is synonymous with the amplitude modulation that is heard upon tuning musical instruments with a tuning fork. The particle's radius of motion will "beat" at a frequency equal to the difference between its cyclotron frequency and that of the radio frequency electric field.

### 3.3.2 Damped Harmonic Motion

One is unlikely to encounter a harmonic oscillator that is not losing energy to its surroundings. This loss of energy is referred to as damping or drag. The mechanism by which this damping occurs, is often friction or air drag. For mass spectrometers, any deceleration of the ions is usually caused by electron-ion, ion-neutral, and ion-ion interactions [23]. Direct collisions do occur, but are less likely than long range interactions. Electron-ion and ion-ion interactions proceed via coulombic interaction forces. Interactions between ions and neutral particles, occur as a result of polarization of the neutral particles and collisions. These effects will be much smaller than those of ion-ion interactions, since the electric potential of a dipole decreases with the square of the distance from the dipole [26] instead of linearly with distance as does the coulombic potential. To derive equations of motion that include these interactions, one needs to insert a damping term into the Lorentz equation 3.11. At this point, the Lorentz equation is that of a parcel of particles rather than a single



particle [27]. By this method one can express the interaction effect as an average, rather than dealing with individual collisions [28].

$$\frac{\vec{F}}{m} = \frac{q}{m} (\vec{E} + \vec{v} \times \vec{B}) - \gamma_j^* \vec{v} \quad (3.35)$$

The damping term,  $\gamma_j^* \vec{v}$ , is velocity dependent, such that the energy loss from collisions with ions and molecules will increase with difference between the orbiting particles' speed, and the speed of the background particles. Since the background particles are at room temperature, their thermal energies are a fraction of an electron-volt. The accelerated ions gain energy quickly, and have in excess of one hundred electron-volts of energy at the end of their trajectories. Thus it is safe to assume that the velocity of the background particles is negligible when compared to that of the accelerated ions. Furthermore, the low temperature of the gas implies that the level of ionization of gas is extremely low [28]. This means that the most important particle interactions will be limited to those that involve ions and neutral particles. Neglecting direct collisions, one may then determine the energy loss and the effect that these collisions will have on the trajectories of the moving ions as a function of collision frequencies. The collision frequency,  $\gamma_j^*$ , is the sum of the collision frequencies between the accelerated ions,  $j$ , and all other species,  $i$ , present in the background gas,

$$\gamma_j^* = \sum_i \gamma_{ij}. \quad (3.36)$$

The Lorentz equation then becomes

$$x'' = F_o \cos(\omega t) + \omega_c y' - \gamma_j^* x' \quad (3.37)$$

and

$$y'' = -\omega_c x' - \gamma_j^* y', \quad (3.38)$$

where  $F_o = qE_o/m$ . Solutions to equations 3.37 and 3.38 can be found as indicated in the previous section for the case without damping. The resulting equations of motion are

$$\begin{aligned} y = & e^{-\gamma_j^* t} \xi \left( 2\gamma_j^* \omega_c \cos(\omega_c t) + (\gamma_j^{*2} - \omega_c^2 + \omega^2) \sin(\omega_c t) \right) \\ & + \frac{\omega_c}{\omega} (\omega_c^2 + \gamma_j^{*2} - \omega^2) \xi \left( \sin(\omega t) - 2 \frac{\gamma_j^* \omega \cos(\omega t)}{\omega_c^2 + \gamma_j^{*2} - \omega^2} \right) \end{aligned} \quad (3.39)$$

$$\begin{aligned} y' = & e^{-\gamma_j^* t} \xi \left( \omega_c (\omega^2 - \omega_c^2 - \gamma_j^{*2}) \cos(\omega_c t) - \gamma_j^* (\gamma_j^{*2} + \omega_c^2 + \omega^2) \sin(\omega_c t) \right) \\ & + \xi (\omega_c (\omega_c^2 + \gamma_j^{*2} - \omega^2) \cos(\omega t) + 2\gamma_j^* \omega \sin(\omega t)) \end{aligned} \quad (3.40)$$

$$\begin{aligned} x = & e^{-\gamma_j^* t} \xi \left( (\omega_c^2 - \gamma_j^{*2} - \omega^2) \cos(\omega_c t) + 2\gamma_j^* \omega_c \sin(\omega_c t) \right) \\ & + \xi \left( (\gamma_j^{*2} + \omega^2 + \omega_c^2) \cos(\omega t) - \frac{\gamma_j^*}{\omega} (\gamma_j^{*2} + \omega^2 + \omega_c^2) \sin(\omega t) \right) \end{aligned} \quad (3.41)$$

$$\begin{aligned} x' = & e^{-\gamma_j^* t} \xi \left( \gamma_j^* (\gamma_j^{*2} + \omega^2 + \omega_c^2) \cos(\omega_c t) + \omega_c (\omega^2 - \omega_c^2 - \gamma_j^{*2}) \sin(\omega_c t) \right) \\ & - \xi \left( \gamma_j^* (\omega_c^2 + \omega^2 + \gamma_j^{*2}) \cos(\omega t) + \omega (\gamma_j^{*2} - \omega^2 - \omega_c^2) \sin(\omega t) \right) \end{aligned} \quad (3.42)$$

The damping term limits the maximum radius that an ion may attain. This effect may be seen in Figure 3.6. The energy loss is more pronounced at higher particle velocities. These interactions may thus be compared to the viscosity of a fluid. The

transient solution vanishes when the energy gain from the electric field is balanced by the energy loss from the interactions with the surrounding particles. Low gas

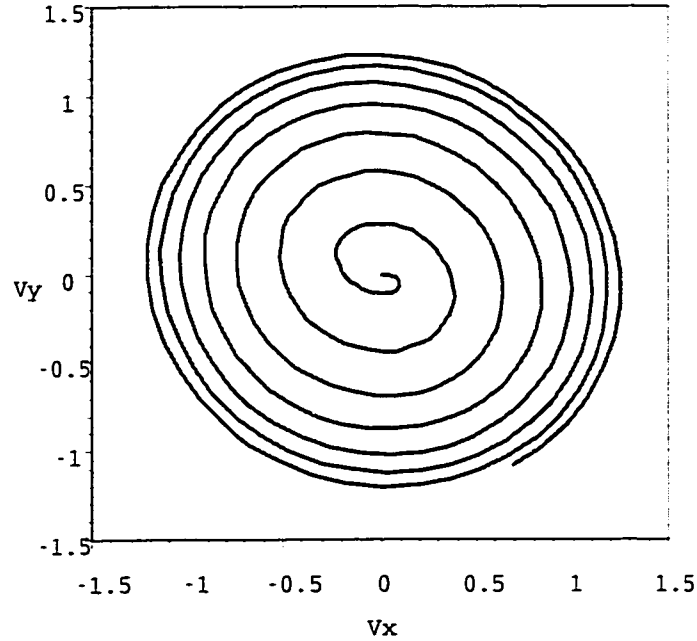


Figure 3.6: Graph of the velocity space trajectory of particles that are accelerated by an oscillating electric field perpendicular to a static magnetic field. At higher velocities, long range interactions with the background gas reduce the net acceleration that the particles experience.

pressures that are used for mass spectrometric measurements ( $10^{-6}$  Torr to  $10^{-8}$  Torr), imply that the collision frequencies will be low. Thus slight damping should be observed and the damping effects should not be as strong as those seen in Figure 3.6.

The effect of direct collisions that result in a loss of ions from the beam of accelerating particles may be accounted for by the use of probabilities. The probability that a particle will not collide with a background gas depends on the path length

that the particle traverses within the gas and its mean-free path in the gas.

$$P_i = e^{-\frac{L}{\lambda}}, \quad (3.43)$$

where  $P_i$  is the probability that an ion will not collide,  $L$ , is the particles path length, and  $\lambda$  is the mean-free path.

The combination of the long range interactions and collisions that particles experience will remove more particles from the beam than collisions alone would. This must come about because the particles lose some of the energy that they gain to the background gas while being accelerated. To reach a collector that is mounted some distance from the centre, the particles require a greater number of revolutions, therefore a longer path length to reach the detector than for the undamped case.

### 3.4 The Electric Potential Field

In the previous sections, the emphasis has been on ion motion in electric and magnetic fields. It is important to look at these fields in more detail. An electric field can completely be described by the electric potential. The relationship between the electric field,  $\vec{E}$  and the electric potential,  $\Phi$  is

$$\vec{E} = -\vec{\nabla}\Phi. \quad (3.44)$$

The differential form of Gauss's law,

$$\vec{\nabla} \cdot \vec{E} = \frac{\rho}{\epsilon_0}, \quad (3.45)$$

where  $\rho$  is the volume charge density and  $\epsilon_o$  is the permittivity of free space, states that a static electric field cannot be present without some charge to source it. Combining equations 3.44 and 3.45, The Poisson equation is obtained.

$$\nabla^2\Phi = \frac{\rho}{\epsilon_o} \quad (3.46)$$

In regions of space, where no charges reside, the Poisson equation becomes Laplace's equation,

$$\nabla^2\Phi = 0. \quad (3.47)$$

The Laplace's equation is commonly used to calculate the potential distribution within a bounded region of space. The electric potential for the infinite (ideal) parallel plate capacitor described in previous sections, can be found using Laplace's equation and the corresponding boundary conditions. A cross-section through the equipotential surfaces within an ideal parallel plate capacitor are shown in Figure 3.7.

The potential is determined by a charge distribution. A cylindrical beam of electrons, can be roughly approximated by an infinitely long column of stationary charges. Applying the integral form of Gauss's Law, one obtains two expressions for the electric field strength. The magnitude of the electric field at a point inside the column is given by

$$E = \frac{\rho r}{2\epsilon_o}, \quad (3.48)$$

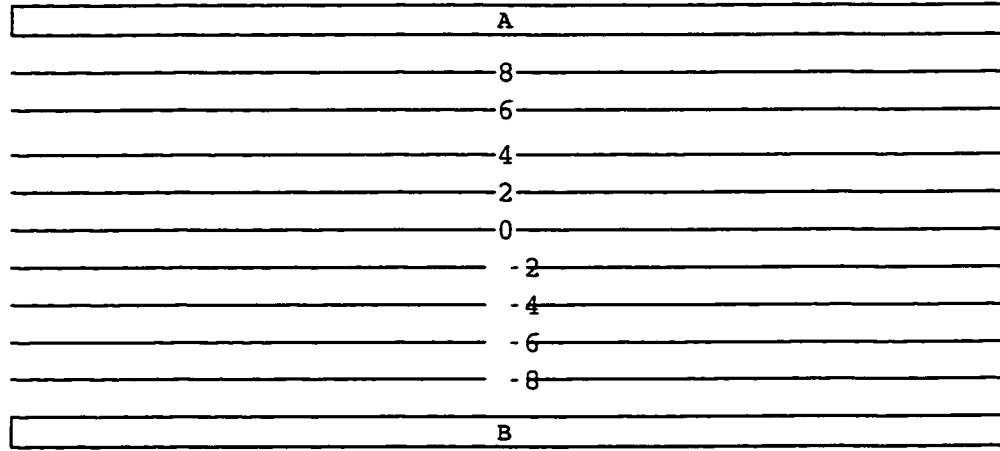


Figure 3.7: Cross-section through the equipotential surfaces within an ideal parallel plate capacitor. A and B are the top and bottom plates. Plate A is at a potential of +10 volts while plate B is at a potential of -10 volts. The potential surfaces are labelled with their respective potentials.

while the magnitude of the electric field outside the column of charge is given by

$$E = \frac{\rho d^2}{8\epsilon_0 r}, \quad (3.49)$$

where  $\rho$  is the volume charge density,  $r$  is the distance to the centre of the charge column,  $d$  is the diameter of the charge column, and  $\epsilon_0$  is the permittivity of free space. For an electron beam (a singly charged plasma), the current density,  $J$ , can be defined as

$$J = e\eta v, \quad (3.50)$$

where  $e$  is the charge of the particles,  $\eta$  is the particle density, and  $v$  is the speed of the particles. The current density can be expressed in terms of the cross sectional area of the beam,  $\pi d^2/4$ , and the current that is flowing,  $I$ . Furthermore,  $e\eta = \rho$ .

Equation 3.50 may thus be rewritten as

$$I = \frac{\rho v \pi d^2}{4}. \quad (3.51)$$

Solving for  $\rho$  and substituting the charge density into equations 3.48 and 3.49 returns the electric field magnitude for an electron beam of a diameter,  $d$ , current,  $I$ , and speed,  $v$ .

$$E_{r < d/2} = 2 \frac{I r}{v \pi d^2 \epsilon_o}, \quad (3.52)$$

and

$$E_{r > d/2} = \frac{1}{2} \frac{I}{v \pi \epsilon_o r}. \quad (3.53)$$

It may prove convenient to express the magnitude of the electric field in terms of the kinetic energy of the charges creating it.

$$E_{r < d/2} = \frac{I r}{\sqrt{\frac{T}{2m}} \pi d^2 \epsilon_o} \quad (3.54)$$

and

$$E_{r > d/2} = \frac{1}{4} \frac{I}{r} \frac{1}{\sqrt{\frac{T}{2m}} \pi \epsilon_o}, \quad (3.55)$$

where  $T$  is the kinetic energy and  $m$  is the mass of the particles.

However, one should realize that the above derived equations for the electric field of the charged cylinder, are approximations because Gauss's Law implies that the electric field at an infinite distance from the cylinder falls off to zero. Where conductive, grounded walls surround the charges, the potential fields must change more rapidly with the radius.

Even more complicated situations arise when a finite parallel plate capacitor is considered. The equi-potential planes are not parallel. Near the edges, the potential surfaces are curved. To accelerate particles as discussed in sections 3.3.1 and 3.3.2, and to determine their trajectories using exact solutions would at best be extremely difficult. Since empty cubic regions of space cannot yield significant insights into the physics of nature, one usually must insert some form of a measurement device that will further distort the field. Chapter 5 shows some numerical solutions to the electric fields and particle trajectories, as they apply to the omegatron. Reality dictates that these derived equations are only a first approximation to the behaviour of ions and neutrals in mass spectrometers. Space charge build up, engineering limitations affecting magnetic and electric fields, and vacuum components, and low partial pressures of the desired ions may all result in significant changes. Numerical models that include approximations of some of these imperfections in real systems may allow deeper insights into the operation of an instrument.



# Chapter 4

## Instrumentation

Instruments that yield reliable results, must be carefully designed to reduce systematic and random errors. Although the measurement scale shown in equation 2.1 eliminates some systematic errors, those that change between the measurement of the sample and standard are not removed. Throughout history, different methods of measuring isotopic ratios have been developed. Many of these employ similar principles to separate ions according to their charge to mass ratios.

### 4.1 Key Components of a Mass Spectrometer

A mass spectrometer can be described by the operation and interaction of three different components; the source, the analyzer, and the collector. Recently, with the availability of fast computers, a fourth component, the data acquisition system, can be added to this list. Figure 4.1 is a schematic diagram of a typical magnetic sector mass spectrometer. The task of the source is to create and accelerate ions. To accelerate the ions, an electric field is used. Ions are commonly accelerated through potential differences of 3000 to 10000 volts. The region between the poles of a permanent or electro-magnet is called the analyzer. Ion beams are separated according to their charge to mass ratios as they traverse the analyzer. In the example, the ion's exit direction is deflected  $90^\circ$  from the entrance direction. The collection of a desired ion species is performed by the collector(s).

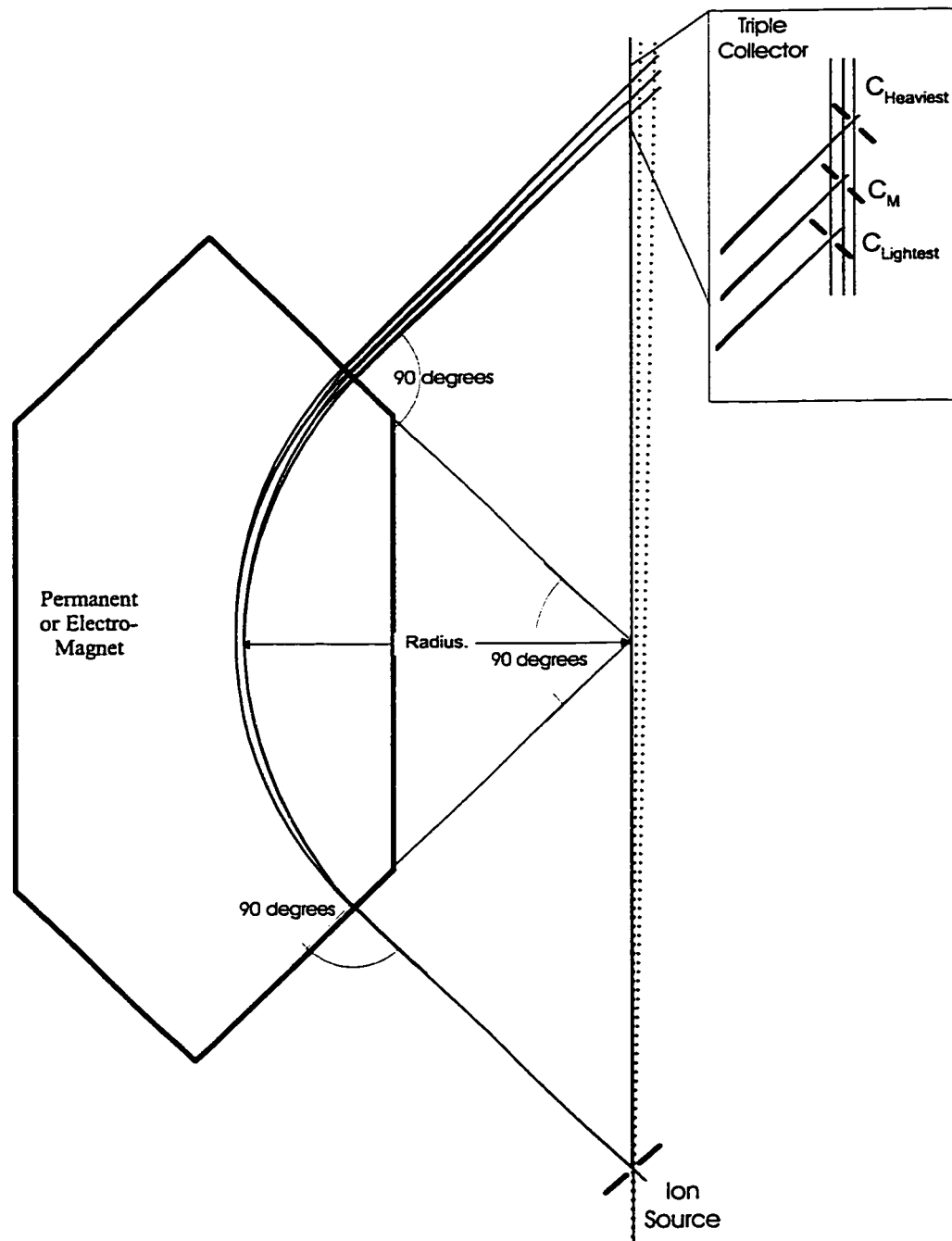


Figure 4.1: Simplified Diagram of a typical 90° magnetic sector mass spectrometer with a triple collector.

#### 4.1.1 The Source

The type of analysis and compound that is to be studied often determines the type of ion source in an instrument. The most common sources are the gas discharge source, the thermal emission (filament) source, and the electron bombardment source.

Gas discharge and spark sources employ a high potential difference between two electrodes that produces an electric discharge [29]. The heat from the discharge evaporates and ionizes a small part of the electrodes, metals or salts that have been placed on the electrodes, or any gases between the electrodes. With this ion source, the isotopic and chemical composition of the samples can be determined. The ions are then accelerated toward the analyzer region by an electric field. Ions created by a gas discharge or spark source have a large thermal energy spread and are often multiply charged. This variability poses difficulties for single focusing mass spectrometers that require of mono-energetic ions. As a result, this type of source is used in conjunction with velocity filters, or double focusing mass spectrometers.

Surface emission ionization, is the process in which a salt deposited onto a metal filament is evaporated and ionized through electrical heating of the filament. Langmuir and Kingdon [30] have shown that both positive and negative ions may be formed by this ionization process. The formation of positive ions is governed by the relation

$$\frac{N_+}{N_o} \propto e^{\frac{q(W-\phi)}{kT}}, \quad (4.1)$$

where  $N_+$  is the number of positive ions created,  $N_o$  is the number of neutral atoms present,  $W$  is the work function of the filament material,  $\phi$  is the ionization potential of the sample,  $k$  is the Boltzmann constant, and  $T$  is the absolute temperature of



Figure 4.2: A solid source triple filament assembly. The center filament is loaded with a sample.

the filament.

For negative ions, the relation changes since the ability of the sample to attract and bind electrons becomes more important than its work function.

$$\frac{N_-}{N_o} \propto e^{\frac{q(A-\phi)}{kT}}, \quad (4.2)$$

where  $N_-$  is the number of negative ions created, and  $A$  is the electron affinity of the sample.

Ionizing samples in this manner, often results in significant portions of the sample having evaporated without ionization. To overcome this problem, triple filament assemblies, where two extremely hot filaments ionize the cloud of evaporated material that was placed on a cooler, central filament, have been developed. One of the greatest disadvantages of this method, is that isotopic fractionation of the salt occurs during the evaporation. Among others, Hitoshi Kanno in 1971 [31] attempted to construct a theory to correct for this fractionation. Moore, Heald, and Filliben [32] expanded on this investigation in 1978 and developed a much more complicated but

also more satisfying model for the observed fractionation.

The electron impact ionization source, was first used by Dempster in 1918 [29] and is suited best to the analysis of gases. A thin filament (Tungsten or Rhenium wire) is heated to high temperatures. This heating imparts sufficient thermal energy to the electrons in the metal to overcome the work function of the material and be emitted. The electrons are then accelerated through an electric potential difference. Typically, the electron energies range from  $70\text{ eV}$  to  $130\text{ eV}$ . The atoms and molecules in the electron beam's path are ionized by coulombic interactions with the electrons. Walter Bleakney [33] improved the ion production by more than an order of magnitude by introducing a magnetic field parallel to the electron beam to reduce the spreading of the beam as it traverses the ionization region. When a low pressure gas is ionized

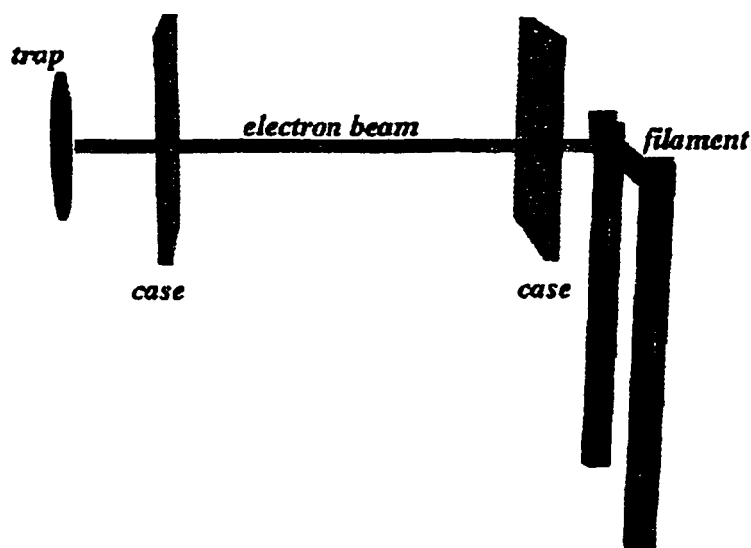


Figure 4.3: An electron impact source

by the electron beam, only a small portion of the electrons are involved in electron-atom or electron-molecule collisions. As a consequence, high electron beam currents are required to produce a significant ion beam. A byproduct of the high electron densities result in multiple electron-ion collisions. A consequence of these and the high kinetic energies of the electrons are doubly, even triply ionized gas species. Further complications arise because the electrons often fragment molecules of the gas. An adverse result of these effects is that some ion fragments of one gas may interfere with the analysis of another gas species whose fragments have similar charge to mass ratios [29]. Electrons may also be captured to form negative ions [29]. Figure 4.3 shows a simplified diagram of the electron emission source. The case is often a cage that surrounds the ionizing region on 6 sides (the 6<sup>th</sup> side has an exit slit for the ions) and is biased positively with respect to the filament (70 to 130 V). In turn, the trap is biased positively (20 V) with respect to the case to avoid the re-entry of electrons into the ionizing region.

#### 4.1.2 The Analyzer

The analyzer of a magnetic sector mass spectrometer separates ions according to equation 3.1. Figure 4.1 shows a spreading ion beam emitted by the ion source entering the magnetic field at a right angle. In what is termed simple geometry the beam is deflected and leaves the magnetic field at a right angle (for the geometry of Figure 4.1) and is refocused at the collector. This property is called direction focusing and can be achieved by designing an instrument such that the source exit slit, centres of curvature of the ion paths, and the collectors lie in the same planes. Extended geometry mass spectrometers, where the angle at which the ions exit the magnetic

field is different from the entry angle are also possible. With appropriate choices of angles, focusing may be realized in the  $z$  direction [34] (perpendicular to the diagram in Fig 4.1 ). The resolution of such<sup>1</sup> a mass spectrometer can be described by the convolution of the ion beam width with the collector slits. As a first approximation, one can assume that the spreading of the ion beam is negligible (or that focusing is very good), so that the beam width upon arrival at the collector slit is the same as the source slit width. Figure 4.4 shows how an ion beam of uniform density swept across the collector slit produces a peak. The peak shape shown represents the ideal

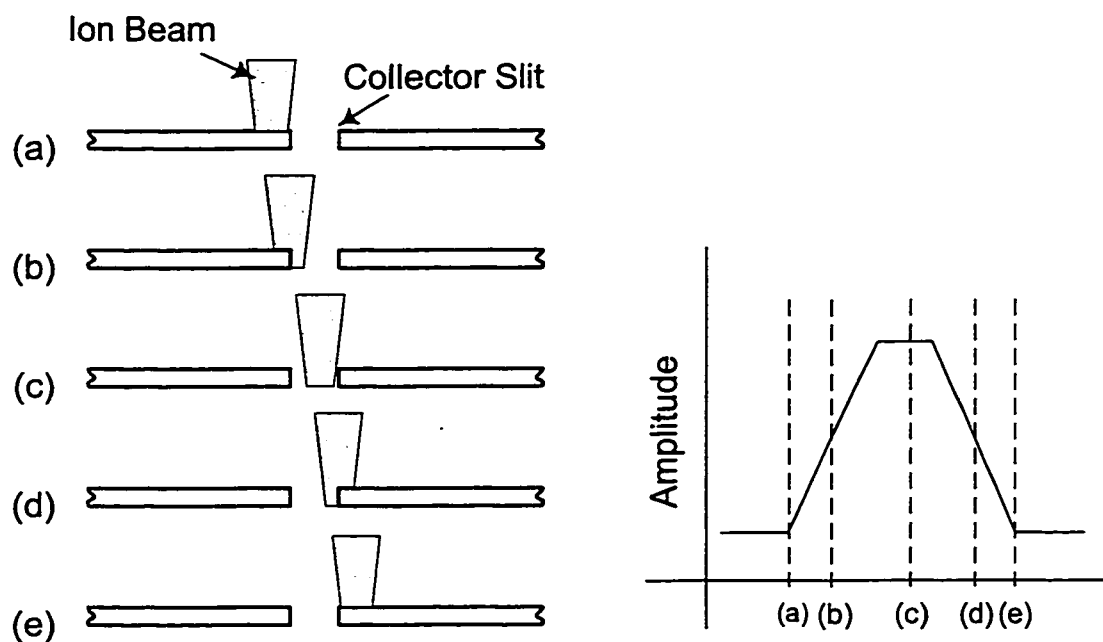


Figure 4.4: Creation of a sector mass spectrometer peak. The beam moves across the slit because the mass spectrometer is used in its scanning configuration. Either the magnetic field is varied, or the energy of the ions is changed to affect a change in the ion trajectories.

case where the beam has a uniform density along its cross section. Any plasma or ion

<sup>1</sup>This would also hold for mass spectrometers other than sector instruments so long as a beam is swept across a collector slit.

beam that is not neutral as a whole, must experience repulsive coulomb forces that will result in a non-uniform ion beam density. The non-uniformity changes the peak shape such that the tops lose the sharp edges, the slopes become curved, and the peaks acquire tails at the baseline. The resolution for the ideal case can be expressed using the simplified expression

$$\frac{M}{\Delta M} = \frac{2R}{S + C}, \quad (4.3)$$

where  $M/\Delta M$  represents the mass resolution,  $R$  is the radius of curvature of the ion trajectories,  $C$  is the collector slit width, and  $S$  is the source slit width.

Equation 4.3 can be arrived at using Figure 4.4. The width of the peak base is given by  $S + C$ . Thus, to resolve the next closest mass, it must be at least a distance  $S + C$  from the first. The equation shows that to effect a change in the resolution of a magnetic sector mass spectrometer, the physical dimensions of the source and collector slits would need to be changed. As will be shown later, mechanical alterations are not necessary to change the resolution of an omegatron mass spectrometer.

#### 4.1.3 The Collector

Before the turn of the century, the lack of low current detectors forced scientists to use fluorescent screens for mass spectroscopy. More importantly, in 1886, Goldstein [29] is claimed to have discovered “positive rays” by the fluorescence that he observed in glass. This lead to J.J. Thomson in 1910 developing his positive ray parabola apparatus in conjunction with a fluorescent screen, to separate and detect



the isotopes of neon. After the turn of the century, the advent of sensitive photographic plates resulted in isotope abundance measurements derived from the opacity changes of these plates. The impact of ions caused the photosensitive coating to darken. Problems with this method of mass spectrography, ranged from different particle energies causing differing darkening of the plates, to the fact that saturation through over-exposure required replacement of the plate. Photo-multiplier tubes, although developed much later, suffer from non-linear current production with increasing ion masses.

Collection of ion currents is usually done using a Faraday cup that is typically a 2cm deep rectangular metal box placed behind the collector slit. The first electrical detection of ions was performed using electrometers. As thermionic valves became known in about 1930, Metcalf and Thomson [35] developed a method to use these as amplifiers. Vibrating reed electrometers were also quite popular as it was generally easier to amplify a small alternating current signal, than to keep a direct current amplifier system stable over the long periods of time that were required for the measurements.

Recent technological advances have resulted in metal oxide field effect transistors (MOSFET). These devices have extremely high input resistance and good stability. Packaged as integrated circuits, the MOSFET's are generally incorporated in the design of operational amplifiers (OPAMP). OPAMP's are now the basic building blocks of most electrical detection schemes in commercial mass spectrometers.

## 4.2 Dynamic Measurements using a Magnetic Sector Mass Spectrometer

The magnetic sector mass spectrometer may be used statically, such that more than one faraday cup collect ion beams. In that configuration, the magnetic flux density and the ion energy are kept constant. Operating a mass spectrometer in this way, is often called “simultaneous collection”.

If only one faraday cup is available, one may scan a mass spectrum by changing either the magnetic flux density, or the ion’s energy. Using this method, a significant length of time may pass between the measurement of consecutive mass peaks. This requires equipment that is stable over long time periods, and insensitive to sample pressure changes, or room temperature changes.

Over the past decade, gas chromatographs used as “front-ends” to mass spectrometers (GC-MS) have gained popularity. In these units, a gas sample is prepared by a variety of methods, including combustion. The sample is “pushed” into a long capillary column using a carrier gas. The carrier gas depends on the analyses that are performed, but in most cases helium is used. In the capillary column, different gases are adsorbed and re-released at different times. Thus a time separation of gases such as  $CO_2$ ,  $SO_2$ , and  $NO_2$  is achieved. These time separated gases are then admitted into a magnetic sector mass spectrometer. A computer generally switches the magnetic flux density or the electric field strength that accelerated the ions to accommodate the mass of the species.

Gas source mass spectrometers may also be used in a “static” mode whereby a small amount of gas is admitted to the instrument which is then isolated from

the evacuation line. This is often used in rare gas measurements to gain sensitivity. From the electromagnetic view point, the instrument is “dynamic” in that the peaks are scanned by changing either the magnetic flux density or the potential through which the ions gain energy.

### 4.3 Previous Designs for Omegatrons

In 1949, Hipple *et. al.* [7] developed an instrument based on the cyclotron resonance principle to measure the Faraday and named it the *Omegatron*. It is similar to the cyclotron in that the ions follow circular paths and are accelerated by radio frequency electric fields. It differs in that the ions do not cross regions of high electric fields (as in the gaps between the cyclotron dee’s) that appear as pulses to the ions, resulting in acceleration of ions at a base frequency and its harmonics. Rather, in the omegatron the ions never leave a sinusoidally varying electric field between two metallic parallel plates.

Sommer *et. al.* [14] describe the design of this instrument. Their omegatron was cubic in shape and contained a potential divider connected to metal guard rings that surrounded the analyzing region. These guard rings were used to reduce the curving of the electric field lines near the edges of the analyser region. The radio frequency electric field was applied by holding one plate at ground while applying a sinusoidal voltage to the second plate. The ion collector was installed immediately above the grounded plate, thereby distorting the geometry of the electric field. The resolution of the instrument was affected by space-charge buildup within the omegatron. Investigations on the operating characteristics of this omegatron design were described

by Klopfer and Schmidt [36] in 1960. Early attempts at explaining how the motion of ions is affected by the space-charge build up, and the central, ionizing electron beam were performed by Schuchhardt [37]. The basic cubic design of the omegatron analyser region was widely used [11], [38], and [39] with some slight changes to the trapping potentials or the number of potential-divider guard rings. A radical approach to reduce the memory of the mass spectrometer was used by Batrakov and Kobzev [12]. The cubic design was modified to create an “open” omegatron that had a much smaller surface area. The resulting instrument required shorter bake-out times. Gentsch [40] simplified the design of Sommer *et. al.* and Klopfer and Schmidt with the removal of the guard rings and improved the sensitivity of the omegatron.

In 1963, van der Waal [10] slightly modified the original design by extending the parallel plates in a direction perpendicular to both the applied electric and magnetic fields thereby improving the geometry of the electric field. The guard rings were also omitted to improve the sensitivity of the instrument. The end plates were retained. A disadvantage of this design was the appearance of mass peaks at harmonics of the resonance frequencies of the ion species. Bijma [41] experienced similar harmonic problems with the extended/long design.

The first indication that removing the end plates may have advantages, seems to come from Marklund and Danielsson [42]. A basic cubic geometry was used but end plates and guard rings were neglected. A similar instrument was later employed by Engelmann *et. al.* [45]. One advantage of this design is that the uniformity of the electric fields in the analyser may be improved.

Brubaker and Perkins [43] appear to be the only researchers who placed the

detector in the mid-plane of the parallel plates. The potential on the plates was established by a push-pull sinusoidal signal so that the detector was in a plane near earth potential.

The above designs are summarized in Table 4.1.

Analysis of microwave plasma sources using an omegatron was done as late as 1991 by Friedmann *et. al.* [48]. The instrument that this group used was essentially that of Sommer *et. al.* with the exception that no guard rings were used. The novelty of this design was that instead of using electrostatic ion trapping parallel to the magnetic field, the magnetic field itself was shaped to form a “magnetic bottle”. The magnetic field lines were “pinched” at the walls of the omegatron so that ions travelling parallel to the magnetic field experienced an increase in the magnetic flux density and consequently a force in the opposite direction of their motion, returning most ions to the centre of the analyser.

Further attempts to improve the resolution of the omegatron were performed by Petley and Morris [44]. Their omegatron used hyperbolic RF electrodes, and contained no guard rings. A serious problem with this design was the appearance of harmonic peaks. Petley and Morris suggested that these may be removed with the addition of a hyperbolic guard ring structure.

#### 4.4 Construction and Design of the Current Omegatron

The popularity of the omegatron seems to have declined since the 1960's and 1970's. During that time, small commercial units could be bought from well known vacuum-tube manufacturers such as Philips. Manufacturers apparently ceased production

Refs.	RECT	MDPD	SS-RF	NSP	GRG	HARM.	max R	max B
[7] [14]	*		*		*	*	$< 1\text{ cm}$	$0.47\text{ T}$
[10]			*				$< 1.5\text{ cm}$	$0.44\text{ T}$
[40]			*				NA	NA
[42] [45]			*				$< 1.2\text{ cm}$	$0.4\text{ T}$
[43]	NA	*					NA	NA
Philips commer.							$\sim 1\text{ cm}$	$\sim 0.4\text{ T}$
This Work	*	*		*			$1.8\text{ cm}$	$1.2\text{ T}$

Table 4.1: Summary of the most important features of previous and current omega-tron designs. RECT indicates whether the analyser is rectangular, MDPD indicates that the detector is located in the mid plane between the RF plates, SS-RF indicates that a single-sided radio frequency signal is used and one RF plate is grounded, GRG indicates the use of guard rings, and HARM indicates that the design suffered from harmonic effects. Max R, and max B show the maximum radius of curvature and the maximum magnetic flux density that were possible with the instruments. Entries labelled NA indicate that the information was not available.

as the instruments are no longer commercially available. Thus, an omegatron was designed and constructed as one aim of the project described in this dissertation.

#### 4.4.1 The Vacuum Chamber and Suspension Arm

A Harvey-Wells Corporation L-128A nuclear magnetic resonance electromagnet and a Harvey-Wells HS-1050 magnet power supply were available for the construction of the omegatron. The size and great mass of this magnet created a number of design constraints on the mounting system and the geometry of the vacuum chamber. The gap between the 30.48 cm (12") diameter pole pieces of the magnet is 6.4cm (2.52"). The vacuum chamber must fit between the pole pieces, leaving sufficient space to align the instrument in the magnetic field by rotating the chamber and also allow easy access to the instrument for cleaning or replacing filaments. Figure 4.5 shows



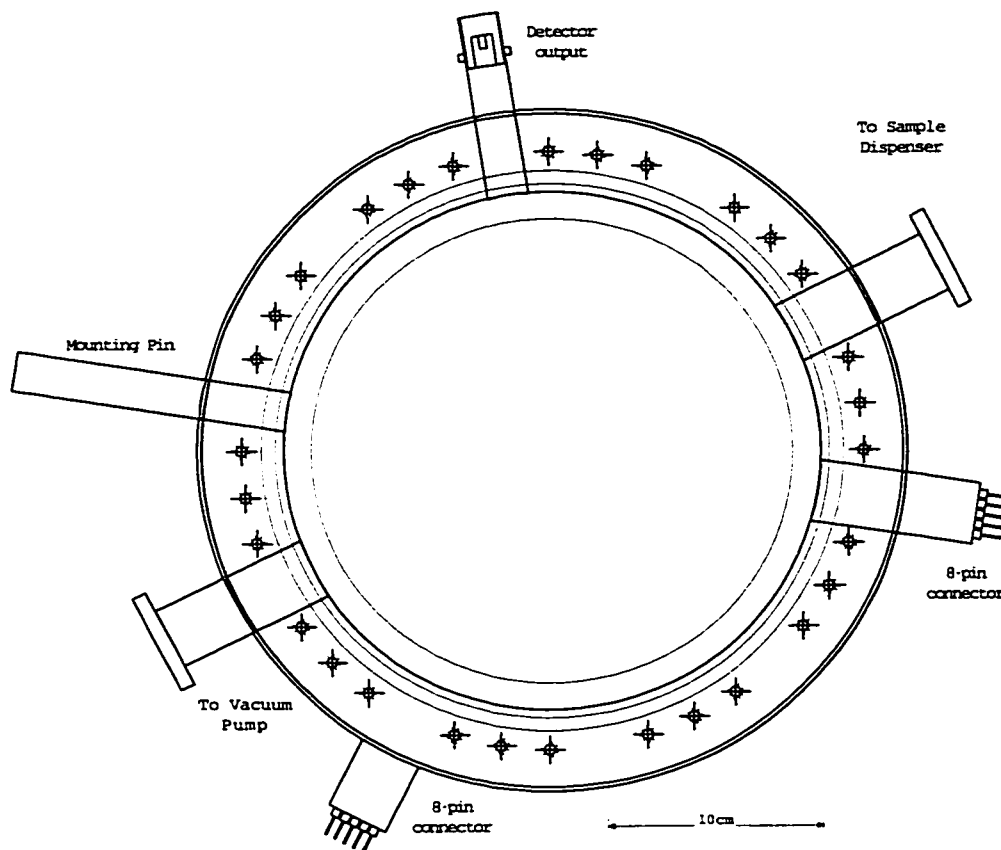


Figure 4.6: Side view of the omegatron mass spectrometer vacuum chamber.

a cross-sectional view of the vacuum chamber and lid. A side view is shown in Figure 4.6. Since the chamber needed to be rugged and chemically non-reactive, it has been constructed of 316 grade stainless steel. This material was chosen for its extremely low magnetic permeability ( $\mu = 1.02 \text{ N/A}^2$ ) and high strength. Other 300 grade stainless steels do not possess the same ability to keep their shape when under pressure or vacuum. Con-flat knife edges were machined into the bottom section of the chamber and the lid to accommodate a standard size 30.48 cm (12") vacuum flange copper gasket. Thirty counter-sunk stainless steel bolts provide the pressure for the metal-to-metal seal. The bolt spacing has been arranged so that each bolt is



spaced  $9^\circ$  from the next, with every fourth bolt omitted to permit larger diameter power feedthroughs and vacuum pipes. The current configuration consists of two



Figure 4.7: Suspension arm with the vacuum chamber attached, showing the rotational degrees of freedom.

3.34 *cm* diameter (1.33") flanges on opposite sides of the diameter. One flange is connected to a 75 *l/s* Varian Star-Cell Ion Getter Pump by a valve attached to a flexible bellows vacuum hose, while the second serves to rough pump the chamber, and admit gas samples for analysis. The electrical connections consist of one coaxial BNC feedthrough, and two eight-pin molybdenum power feedthroughs. Since the power feedthroughs are rated at 500 volts and 10 amperes per pin, they are suitable

for all electrical connections, including the power for electron emission filaments that may require as much as 4 amperes of current.

The mounting bracket that supports the vacuum chamber must be (1) rigid to prevent movement during measurements, (2) allow the chamber to be rotated, to align the omegatron with the magnetic field, and (3) easily removed. Figure 4.7 shows the mounting arm, that has been suspended from a sliding platform, that allows easy removal of the vacuum chamber from between the magnet's pole pieces. The vacuum chamber is attached to the mounting arm by a polished 1.9 cm ( $3/4$ " ) diameter stainless steel pin that allows rotation about a horizontal axis. To have complete control over the alignment, the arm may be rotated about its (and the vacuum chamber's) vertical axis. To reduce weight and magnetic interference, the mounting bracket has been constructed of aluminum.

#### 4.4.2 The Omegatron Interior

The striking difference between the omegatron and conventional mass spectrometers is that the source, analyzer, and the detector occupy the same volume. Yet the functioning of each component has strong similarities with conventional mass spectrometers. Whereas the magnetic sector mass spectrometer accelerates ions through a static electric field, then it separates them in a static magnetic field, the omegatron is designed such that the separation of the ions begins right at the moment of the initial ionization, and ends with the ion striking the detector. The ions gain energy from an oscillating electric field applied perpendicular to a static magnetic field as described in the previous section on the theory of ion motion. The advantage of this scheme is that the instrument can reach extremely high resolution for low particle

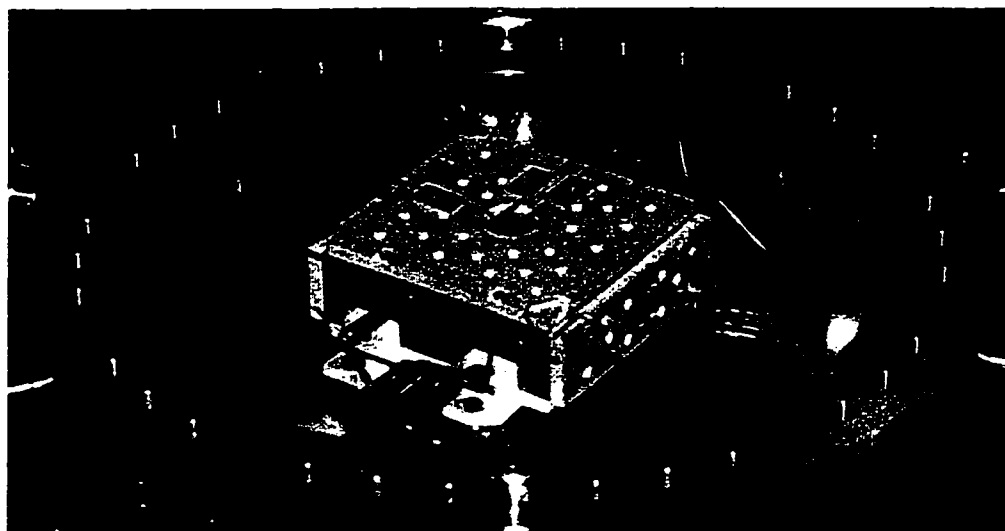


Figure 4.8: Photograph of the “old” omegatron design.

masses.

The resolution of the omegatron is strongly dependent on the homogeneity of the electric and magnetic fields that determine the ion motion. For this reason, the focus of the first attempt to construct an omegatron for this dissertation, was to improve the electric field homogeneity. A geometry similar to, but larger than that of Sommer *et.al.* [14] was designed. Grooved ceramic plates were used to support a resistive wire grid, that was used instead of the guard rings to reduce the warping of the electric field lines near the edges of the analyzing region (Figure 4.8). Sixty rows of wire were used on each of the four sides enclosing the analyzing region. Opposing wire grids were connected in parallel to allow independent control of the trapping potentials parallel and perpendicular to the magnetic field, as discussed by Masica [38]. This geometry was equivalent to that of an analyser region surrounded by sixty guard rings. Measurements that were taken with the unit were not consistent. Subsequent measurements showed that the resolution of the instrument decreased as a function

of the time that the omegatron was operated. This reduction became so extreme, that it was not possible to observe any mass peaks. After long periods outside the magnetic field, and with the ionizing electron beam turned off, operation could be resumed for short time periods. The reason for this behaviour is consistent with surface charge build up on the exposed ceramic surfaces. It is likely that over long periods of time, the charge build up on the walls of the instrument created electric fields comparable to or greater than the applied radio frequency electric fields.

A second, much simplified instrument was designed and built (Figure 4.11). The current omegatron is a long (rectangular) design similar to that constructed by van der Waal [10] in 1963, but differs significantly in having no side plates or guard rings [14], and the collector positioned in the midplane



Figure 4.9: Photograph of the current omegatron design showing the position of the parallel RF plates and the filament holder on the top.

between the RF acceleration plates (Figures 4.9 and 4.10). The analyzer region is



Figure 4.10: Photograph of the current omegatron design showing the position of the detector.

3 cm deep by 4 cm high by 9cm wide. The ion collector may be positioned at a distance of up to 3 cm from the electron beam. The position of the radio frequency plates allows a maximum collector distance of 2 cm but the plates may be moved further apart. As seen in Table 4.1, this design is a unique combination of features in previous designs.

A trapping potential parallel to the magnetic field that prevents the ions from moving along the magnetic field lines and impacting with the walls of the analyzer region can be applied but a perpendicular trapping field is not possible because of the absence of end plates perpendicular to the magnetic field. Guard-rings or wire grids were not incorporated to reduce the surface area available for adsorption of gases. The advantage of a long (rectangular) design is that the electric field lines, in the middle region, that are used to accelerate ions are more uniform than in the classical cubic design. Thus, the ion orbits are more circular and the resolution of the instrument is improved. The detector and the detector support block cause

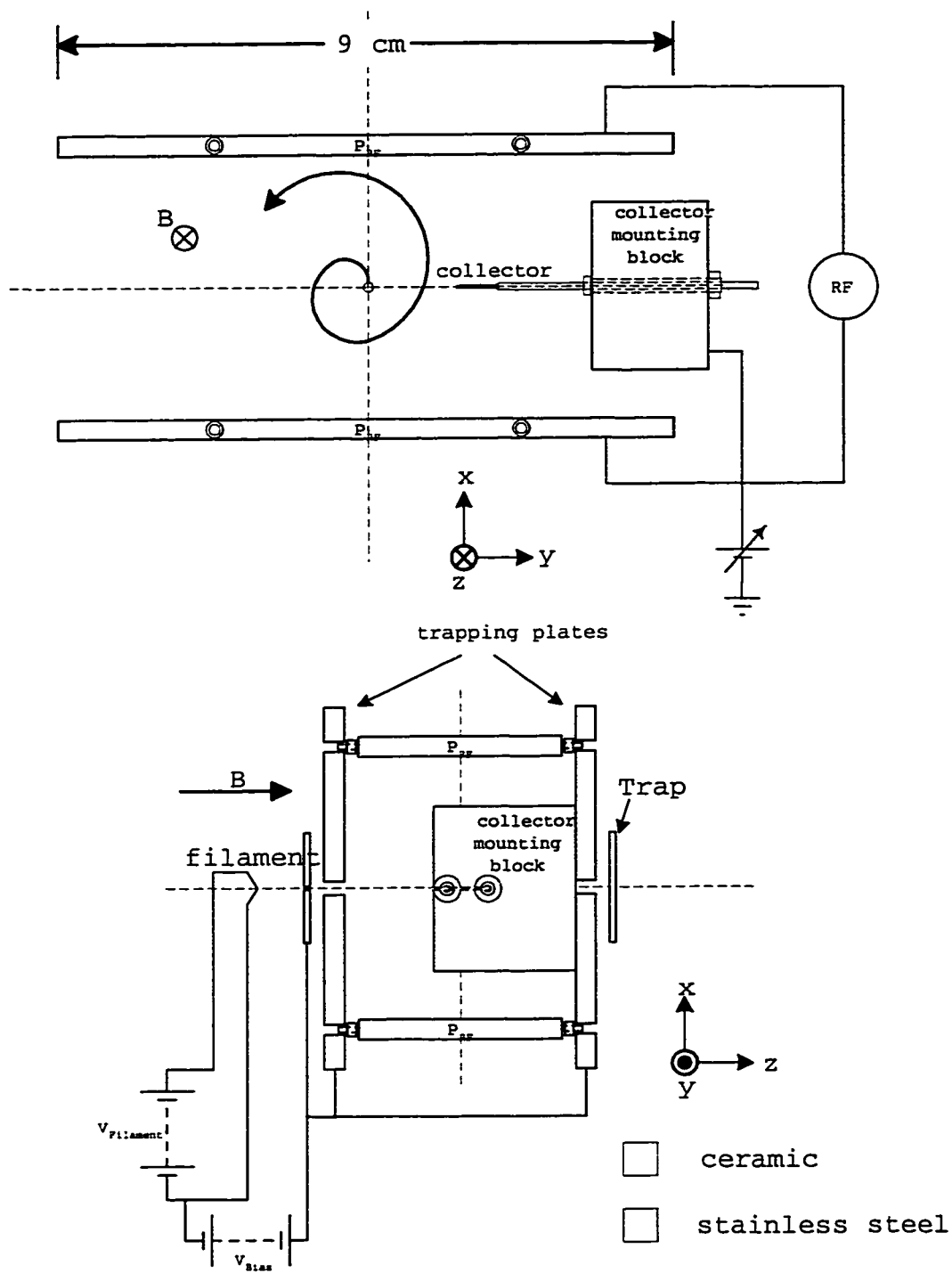


Figure 4.11: Diagram of the omegatron as was used for the measurements acquired for this work and shown in later chapters.

the greatest disturbance of the electric field geometry. Many omegatrons that were used [14], [41], [45], [46], placed the detector close to a grounded radio frequency plate, where it could greatly affect the electric potential fields. The current design, places the collector in the middle between two radio frequency plates. Since the mid-plane between the radio frequency plates is at ground potential and the collector's potential (determined by the amplifier) is only a few milli-volts removed from ground, this arrangement results in the least change to the electric field. The extended design also improves the electric field geometry so that the side plates may be left off as in the design of Marklund and Danielsson [42] . A further advantage of this design is that one need not perforate any of the remaining walls as was done by Wang *et.al.* [39] and by Friedmann *et.al.* [48], since the transmission of gas into the analyzing region is much higher without the side plates.

The omegatron was constructed of 304 grade non-magnetic stainless steel. Insulating materials were used only where it was absolutely necessary and then the insulating surfaces that face any portion of the analyzing region were minimized to reduce charge accumulation. Spacers made of Makor machinable ceramic align and support the metal plates to which the radio frequency is applied. The ion collector also is insulated from its support structure by ceramic sleeves.

The ionizing electron beam is created with a 0.12 mm diameter Rhenium-Tungsten alloy<sup>2</sup> filament. The first filaments were made of 0.05 mm diameter tungsten but proved to be extremely sensitive to vibrations that often resulted in breakage of the filament. The alloy has a much higher electric resistivity than pure tungsten, allowing the use of thicker wire while keeping the current required for electron emission

---

<sup>2</sup>The alloy contains 75% W and 25% Re.

low. Custom built filament posts were used to position the filament, as commercially available filament posts are often constructed using magnetic materials that would experience large stresses within strong magnetic fields and cause inhomogeneities of the magnetic fields at the analyzer.

## 4.5 Data Acquisition and Signal Generation

To improve reproducibility and reduce the chance of user introduced errors, the omegatron has been designed to operate almost entirely by computer control. Only vacuum components such as valves and pumps need to be operated manually. A mass spectrometry computer interface designed by Kaare Berg and Michael Wieser [49] and Kaare Berg *et. al.* [50] is used for the data acquisition. Figure 4.9 shows a block diagram of the electronic components used for generating and acquiring mass spectra. The electron beam that ionizes the samples is stabilized by amplifying the trap current and converting it to a frequency. This frequency is monitored and used as the feed-back signal for the electron emission filament power regulator. The ionized gases are accelerated using a push-pull RF-driver that receives a frequency signal from a Wavetek 395 synthesized frequency generator. This frequency synthesizer is computer controlled through a serial communications port. The mass spectra ion currents are amplified and converted to a frequency. The computer records the trap current and ion signal that the mass spectrometry interface receives via its fiber optic couplers.



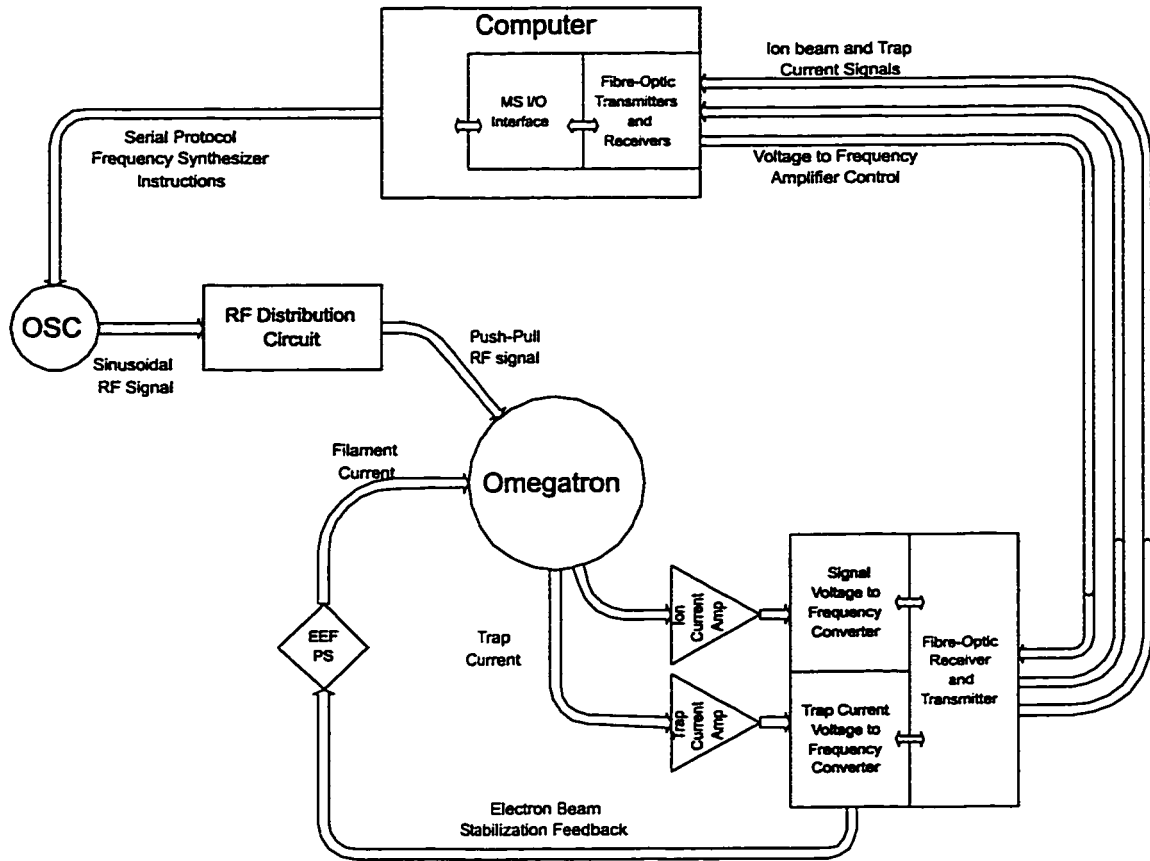


Figure 4.12: Schematic diagram of the electronics used to operate the omegatron. The abbreviations EEF PS, OSC, MS I/O stand for the electron emission filament power regulator, the synthesized frequency generator, and the mass spectrometry interface board respectively.

#### 4.5.1 Filament Power Regulation

The filament power regulator has been designed so it can be connected to any floating DC power source of up to 30 volts. In conjunction with the trap-current pre-amplifier and the voltage to frequency converter, it functions as a phase lock loop. A phase comparator, receives both the opto-isolated feed-back signal, and a digitally selectable crystal generated frequency reference. The output of the comparator, a voltage that is proportional to the time average of the phase difference of the two

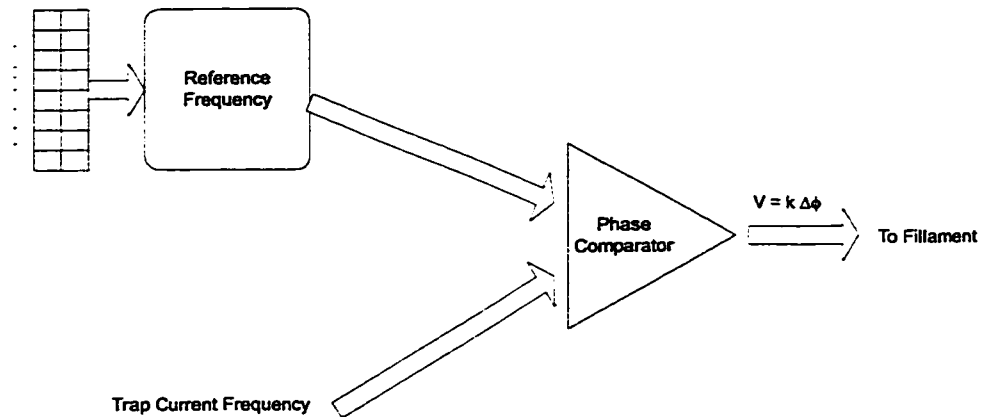


Figure 4.13: Schematic diagram of the filament power regulator. Electron emission is regulated by controlling the filament temperature through a phase comparison of the frequency converted trap current, and an adjustable frequency reference.

frequencies, regulates the power supplied to the electron emission filament. Figures B.3 and B.4 in Appendix B display detailed electrical diagrams of the circuitry.

#### 4.5.2 The Radio Frequency Driver

Since this design needs a push-pull sinusoidal signal and the signal from the generator is grounded on one side, a frequency driver is required. The first generation frequency driver was a toroidal transformer with its primary driven by the Wavetek, and the RF signals were taken from its secondaries. The secondary for the RF plates was center tapped and grounded while the other connections were center tapped and connected to a variable voltage power supply. Although sufficient for preliminary tests, this method did not allow for computer control of DC offset during data acquisition and was limited to the power output of the synthesized signal generator.

With this in mind, a second circuit was designed (Figure 4.14). This circuit, a block diagram is shown in Figure 4.11, uses one LM6181 high speed operational

amplifier as a differential amplifier, to isolate the ground of the omegatron from the signal generator ground. Thereafter, two LF6181 op-amps are used to provide one inverted and one non-inverted signal. Each of these high-speed current-feedback amplifiers is designed to provide a potential difference of  $10V$  into a  $100\Omega$  load. The

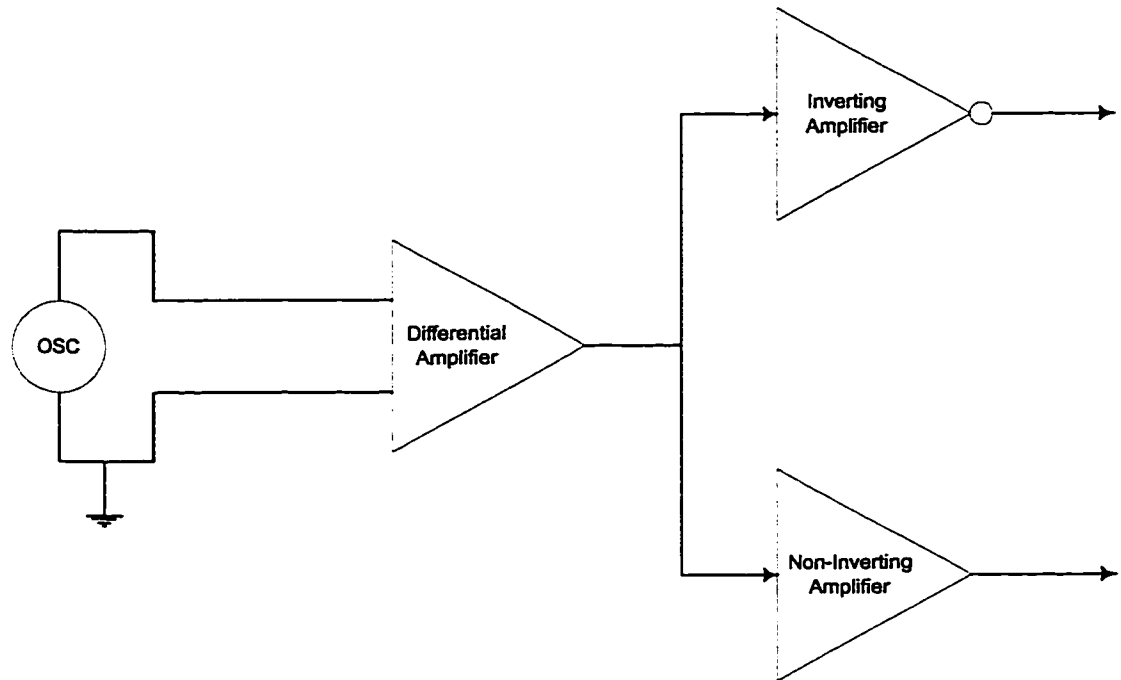


Figure 4.14: Block diagram of the RF-Driver that generates a ground-isolated push-pull signal from the ground referenced signal provided by the signal generator

driver thus acts as a phase splitter and power booster for the RF signal. The synthesized signal generator cannot supply more than  $5V$  into a  $50\Omega$  load (or  $250mW$ ). The maximum output of one amplifier is  $1W$ . To keep the amplifier from oscillating, it must not drive a capacitive load. If the load is capacitive, as with coaxial cables, the amplifier must be back-terminated. A  $50\Omega$  load may be back-terminated with a  $50\Omega$  resistor, thus reducing the usable power to  $1/2W$  per amplifier. A realistic

value for the power gain is a factor of four greater,  $1W$ , when compared with that of the Wavetek 395.

### 4.5.3 Ion Current Amplification

Finally, the amplification of the small currents produced when ions impact the collector is required. For positive ions, the currents that one amplifies stem from the electrons that move from the earth through the amplifier into the detector to neutralize the charge imbalance at the detector. Magnetic sector mass spectrometers often measure ion currents from  $10^{-8}$  to  $10^{-12} A$ . Operational amplifiers, serving as transimpedance devices, convert these low currents into signals ranging typically from  $1 mV$  to  $10 V$  which serve as inputs to other devices such as voltage to frequency converters. As DC signals are usually measured, noise may be reduced with a band-width reducing capacitor, as shown in Figure 4.12. To measure the small

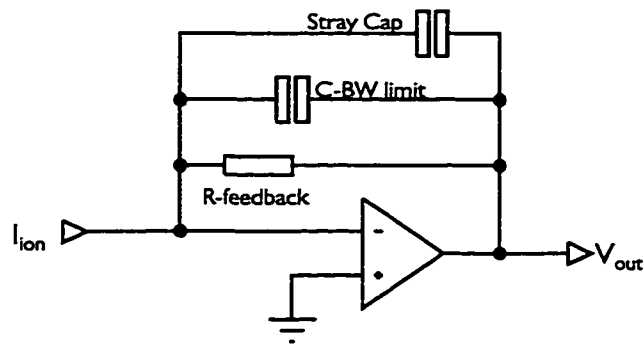


Figure 4.15: Circuit diagram of the amplifier configuration used for conventional mass spectrometers.

currents without much interference from voltage noise (including Johnson noise, amplifier noise, triboelectric effects in transmission lines, commonly of the order of  $10^{-5}$

to  $10^{-6} V$ ), the resistances must be between  $10^9 \Omega$  and  $10^{11} \Omega$ . With a band-width limiting capacitor of  $10 pF$ , a low pass filter with a “time constant” of up to one second would result. A sudden change of the input signal would result in the amplifier output lagging in time. To achieve an output that lies within 0.5% of the correct value, the amplifier would require a settling time of approximately 5 seconds. With dual or triple collector mass spectrometers, where the currents are simultaneously measured under constant conditions, this time delay does not pose a great problem. In fact, small variations in the signal are damped.

For a “dynamic” mass spectrometer such as the omegatron and continuous flow mass spectrometers and magnetic sector instruments that scan over a mass range, this delay can present some difficulties. During a measurement, these “dynamic” instruments require that the magnetic and electric fields and the performance of the electronic measurement equipment do not change. Short measurement times are more important for dynamic instruments. The omegatron has only one collector. To measure the isotope abundance ratio of two isotopes, the instrument must scan through a frequency range. During this time, any variation in the physical parameters such as the gas pressure, electron beam intensity, and the magnetic flux density can potentially change the measured ratio. It is thus important to quickly complete the measurement scan.

Rather than attempting to reduce the capacitance and increase the amplified noise, an integrating amplifier design has been constructed for use with the omegatron. The IVC102 integrating transimpedance amplifier (Burr Brown Corp.) is used. Since all of the solid state switches and capacitors needed for its operation are included in the IVC102, leakage of small currents across printed circuit boards

need not occur. Figure 4.13 shows the circuit that is contained within the IVC102. Several operating modes may be implemented with this design. The mode used for

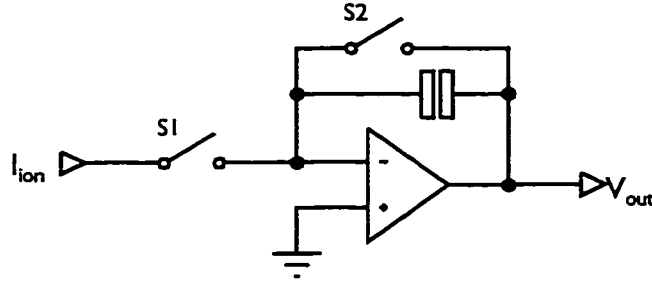


Figure 4.16: Operational schematic diagram of the IVC102 integrating trans-impedance amplifier.

the omegatron was chosen so that all ions striking the detector would contribute to the measured ion current. At the start of an integration, switch S2 is closed and switch S1 is in the open position. For a short period that is required to discharge the capacitor C1, ions striking the detector are building up charge on it. After switch S2 is opened and S1 is closed, the integration of the ion current starts. Next, switch S1 is opened again to allow a DC measurement of the output voltage. This voltage is proportional to the charge that accumulates on the capacitor,

$$V = \frac{Q}{C} \quad (4.4)$$

where V is the output voltage, Q is the accumulated charge, and C is the capacitance. The general expression for a time dependent ion current is given by

$$V = \frac{1}{C} \int_0^T I(t) dt. \quad (4.5)$$

Signals obtained with the omegatron are DC signals. A more specific expression in terms of a steady ion current therefore is more applicable.

$$V = \frac{T}{C}I, \quad (4.6)$$

where  $T$  is the integration period, and  $I$  the DC current. The gain of the amplifier may be expressed as  $G = T/C$ . The next cycle is started by closing the reset switch, S2. An advantage of using this method for amplifying small currents is that amplifier settling time does not affect measurements. The MS computer interface is not designed to sample synchronously with the integrating amplifier. To keep the amplifier compatible with the interface, a sample and hold circuit has been added as its final stage. A complete circuit diagram is shown in Appendix B, Figure B.1.

The timing signals for the amplifier switches are generated by the circuit shown in Appendix B, Figure B.2. The frequency of a 30720 Hz crystal oscillator found in most digital watches, is used for the timing signals. As the crystal oscillator frequency and thus the integration frequency are multiples of 60 Hz. Any 60 Hz, 120 Hz, 180 Hz, ... line noise is efficiently filtered by averaging over full cycles of these noise sources.

# Chapter 5

## Numerical Models

Recent developments in computer technology have enabled scientists to obtain solutions to more complicated numerical problems. J. Bijma [41] pioneered the computation of particle trajectories for an omegatron. Although his models include only a few revolutions and are missing more realistic features such as the electric field of the ionizing electron beam or slight damping that the particles experience, considering that Bijma was limited to analog computational equipment, the calculations he performed were a great achievement.

### 5.1 Methods of Solving Ordinary Differential Equations

Particle trajectories that were computed for this work, are based on the equations of motion, 3.25 and 3.26. The programming was done using Fortran 90 on two different computer systems. The shorter computations were performed on Pentium 166 microcomputers. Memory limitations of these micro-computers, while executing integrations well away from the cyclotron frequency of particles, forced the code to be migrated to an AIX mainframe. The numerical integration is performed using a NETLIB <sup>1</sup> package for ordinary differential equations, RKSUITE\_90 developed for FORTRAN 77 by Brankin *et.al.* [51], and ported to FORTRAN 90 by Brankin and Gladwell [52].

---

<sup>1</sup>NETLIB is a collection of mathematical software and papers on the Internet. Its URL is <http://www.netlib.org> .



A number of different fourth/fifth order Runge-Kutta algorithms were tested to find the particle trajectories, but numerical errors (most likely rounding errors) resulted in a phase shift between the test particles and the applied electric field after the particles had completed of the order of forty cycles. The RKSUITE library uses three different Runge-Kutta pairs<sup>2</sup> (4,5), (7,8), and a (2,3) pair, depending on the accuracy requirements of the solution. The (4,5) pairs were used for the computations presented in this work.

The basic idea of integrating (solving) an ordinary differential equation (ODE) as an initial value problem (IVP) numerically is to use the data available at an initial point, and extrapolate it to the endpoint. One method of doing this is to take the initial value of the function,  $f(\vec{x})$ , and determine the derivative of that function at the initial value to determine the function at the end point.

$$f(\vec{x}_o + \vec{h}) = f(\vec{x}_o) + \vec{h} \left[ \frac{\delta}{\delta \vec{x}} f(\vec{x}) \right]_{\vec{x}=\vec{x}_o} \quad (5.1)$$

In the above equation  $\vec{h}$  is the step size of the integration. By repeating this process, the problem may be integrated. This is the Euler method of integrating ODE's [53]. The main disadvantages of this method are low accuracy and stability. The next iteration would be to use the initial value  $\vec{x}_o$  to find a point half way between the  $f(\vec{x}_o)$  and the end-point of the interval  $f(\vec{x} + \vec{h})$ . This mid-point is used to evaluate the derivative at the mid-point. The derivative at the mid-point is then

---

<sup>2</sup>The pairs refer to the order.

used to advance the function over the interval such that

$$f(\vec{x}_o + \vec{h}) = f(\vec{x}_o) + \vec{h} \left[ \frac{\delta}{\delta \vec{x}} f(\vec{x}) \right]_{\vec{x}=\vec{x}_o + \frac{\vec{h}}{2}}. \quad (5.2)$$

This is referred to as a second order Runge-Kutta. The higher order Runge-Kutta algorithms extend this system to enhance the reliability and accuracy of the integrations. Computational time savings can be achieved by using adaptive step-size algorithms. These algorithms can determine how fast a function varies and adjust the step sizes used for the integrations accordingly.

## 5.2 Particle Trajectories

This section is organized much like the theory chapter. First, the most basic parallel plate capacitor is used to accelerate particles. Next, an electron beam at the centre distorts the electric field, and deflects the trajectories. The last part incorporates a damping term into the equation of motion. The number of cycles that particles are shown to travel have been reduced so that individual parts of the spiral can be seen.

### 5.2.1 Ion Trajectories in a Parallel Plate Capacitor

For these computations, equations 3.25 and 3.26 are used. The integration was started with the ions initially at rest at the origin. The ion collector was positioned on the positive x-axis,  $1.5 \text{ cm}$  from the origin. Ions were said to strike the detector if they reached the detector at  $x = 1.5 \text{ cm}$  and came to within a  $0.05 \text{ cm}$  vertical distance of the detector. The parameters for the integration are shown in table 5.1.

Magnetic Flux Density	$1\text{ T}$
RF Angular Frequency	$9.648\text{ s}^{-1}$
Ion Mass	$10^7 amu$
RF Electric Field	$2.5 \times 10^{-3}\text{ V/m}$
Charge	1 electronic charge

Table 5.1: Integration parameters for the omegatron modeled as an ideal parallel plate capacitor.

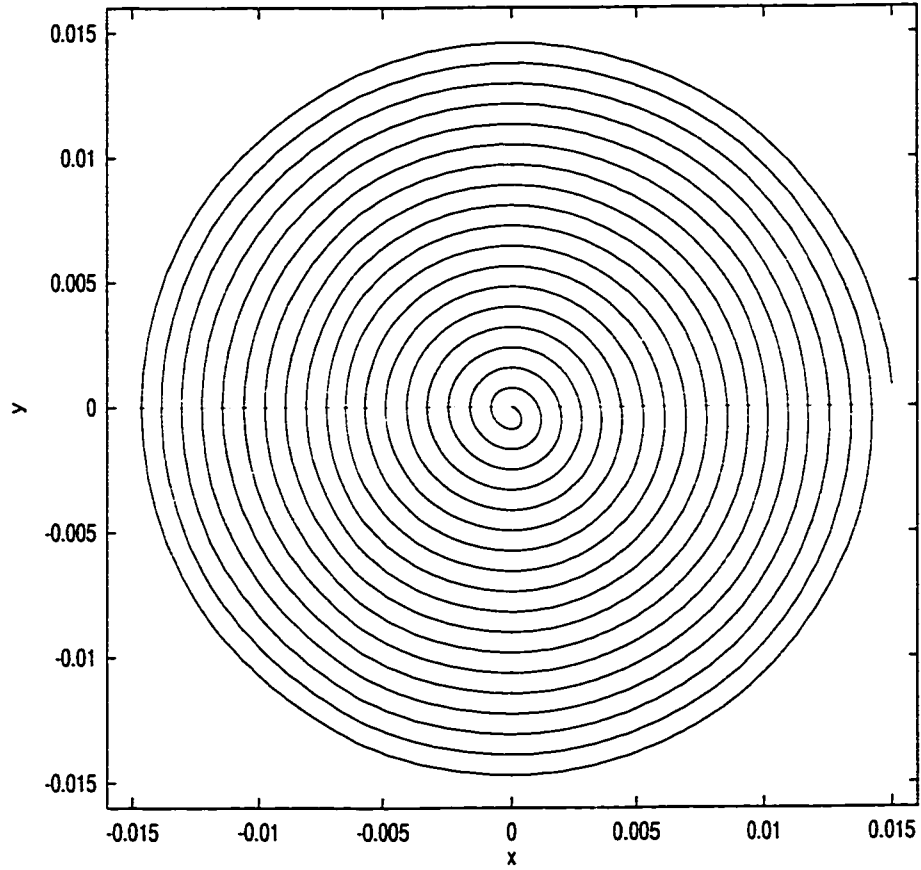


Figure 5.1: Trajectory of a resonant particle in the omegatron modelled as an ideal parallel plate capacitor.

A large ion mass was chosen, so that any rounding errors in the time steps for the integration would be small compared to the step size. A small mass requires a high radio frequency field. To integrate one whole revolution of the ion paths, between one hundred and one thousand time steps are required. High frequency oscillations have short periods. Further dividing these already small numbers by two or three orders of magnitude often makes the step size comparable to a computer's roundoff error. Figure 5.1 shows the trajectory of the particles. The spiral produced is evenly spaced and keeps increasing. This trajectory is of the same type as that determined from the exact solution in chapter 3, and proof that the code is working properly.

### **5.2.2 Ion Trajectories in a Parallel Plate Capacitor with a Central Electron Beam**

The more complex situation, when an electron beam (modelled as a column of charge) is present at the centre of the ideal omegatron, yields particle trajectories that are somewhat distorted from the previous situation. Table 5.2 shows the parameters that were used to create the trajectory. In Figure 5.2 one can see that the trajectory of the ions is "skewed" towards the detector side. The ions also require fewer revolutions to reach the detector. The radial electric field points toward the centre of the particles trajectories. Throughout its path, the electric field then causes a force toward the centre to be present. The particles are prevented from moving toward the centre by the magnetic field, and as a result a net acceleration occurs.

Although the particles start the spiral motion in phase to the RF electric field, after a short time, the particles will have a greater phase angle than the electric field. At that time, the electric field reduces the increase in the particle energy per

Magnetic Flux Density	$1\text{ T}$
RF Angular Frequency	$9.648\text{ s}^{-1}$
Ion Mass	$10^7\text{ amu}$
RF Electric Field	$2.5 \times 10^{-3}\text{ V/m}$
Charge	1 electronic charge
Trap Current	$2 \times 10^{-3}\text{ A}$
Beam Diameter	$0.3\text{ mm}$
Electron Energy	$100\text{ eV}$

Table 5.2: Integration parameters for the omegatron modelled as an ideal parallel plate capacitor with a column of charge at the origin, representing the electron beam.

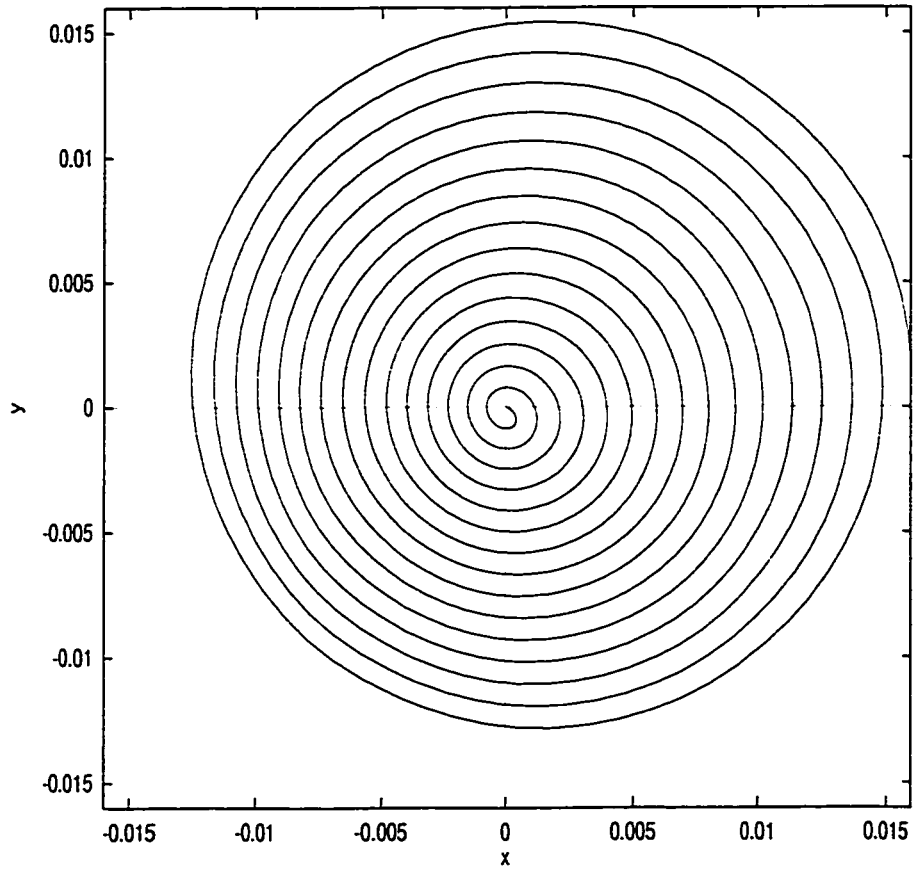


Figure 5.2: Trajectory of a resonant particle in the omegatron modelled as an ideal parallel plate capacitor with a column of charge at the origin of the x-y plane and aligned along the z-direction, representing the electron beam.

revolution. The natural frequency of precession about the magnetic field lines is altered by the presence of a radial electric field. Since the particles lead the RF electric fields, their new frequency of precession will be higher. A positive cylindrical charge distribution will cause the opposite effect, since the direction of the electric field lines is reversed. A slowing of the particles will result in a reduced effective frequency of precession. With space charge accumulating about the electron beam, a shielding effect may arise [54], [14]. The result is that a particle requires a finite frequency band to accelerate it instead of a discrete frequency. For the omegatron, a critical particle density must exist, which will broaden this frequency band sufficiently to effectively prevent the arrival of the ions at the detector.

### **5.2.3 Ion Trajectories in a Parallel Plate Capacitor with a Central Electron Beam and Long Range Forces damping the ion Motion**

Particles that experience long range interactions as described in section 3.3, as well as an electric field arising from a central charge distribution, are modelled in this section. Table 5.3 lists the parameters that were used to integrate the equations of motion. Figure 5.3 depicts the resulting trajectory. During the first few revolutions, the particles follow the same path that was seen in Figure 5.2. The damping of the motion starts being noticeable when the particles reach higher velocities than the thermal velocity range of the background atoms. Thus it is at greater radii that the particles gain less energy per revolution and the change in the radius becomes smaller from one revolution to the next. Since the particles experience a smaller energy gain per revolution, they have to perform a greater number of revolutions to reach the detector. Consequently, the particles' path length increases.

Magnetic Flux Density	$1\text{ T}$
RF Angular Frequency	$9.648\text{ s}^{-1}$
Ion Mass	$10^7\text{ amu}$
RF Electric Field	$2.5 \times 10^{-3}\text{ V/m}$
Charge	1 electronic charge
Trap Current	$2 \times 10^{-3}\text{ A}$
Beam Diameter	$0.3\text{ mm}$
Electron Energy	$100\text{ eV}$
Gamma	$0.05\text{ s}^{-1}$

Table 5.3: Integration parameters for the omegatron modelled as an ideal parallel plate capacitor with a column of charge at the origin, representing the electron beam and a damping term.

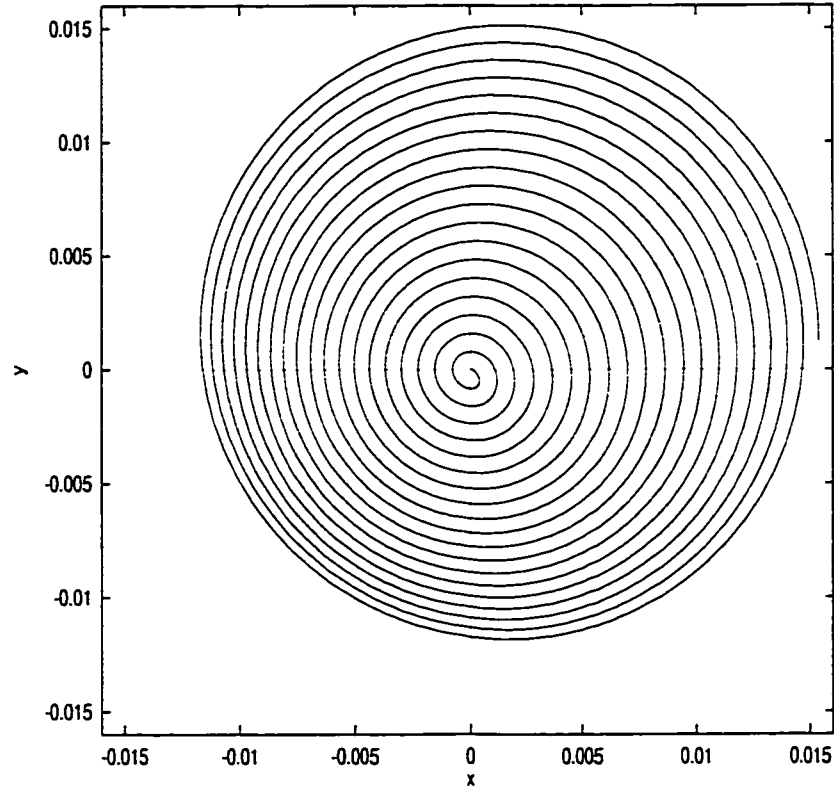


Figure 5.3: Trajectory of a resonant particle in the omegatron modelled as an ideal parallel plate capacitor with a column of charge aligned along the  $z$ -direction, representing the electron beam at the origin of the  $x$ - $y$  plane. Drag forces from ion-ion and ion-neutral interactions result in smaller changes of the radius at higher ion speeds (greater radii).

### 5.3 Theoretical Spectra

To determine the theoretical spectrum of ions, integrations like those that produced the trajectories in the previous section were performed. The only difference between the previous and the following integrations, is that instead of using a small number of revolutions that were previously used to display the changes in the trajectories, the ions were accelerated by a smaller electric field that resulted in at least 250 revolutions near the resonance. This scenario more closely resembles the true path that ions follow. Trajectories at frequencies significantly different from the cyclotron frequency resulted in an even greater number of revolutions. The path lengths that ions traverse in transit between their point of creation (the electron beam) and the collector, have been recorded. The path lengths can then be plotted as a function of frequency. To approximate the shape of the resonance spectrum, the path length was next used in equation 3.43 to determine the fraction of particles that arrive at the detector. By using this equation, direct collision of ions with the background gas are taken into account. Particles that collide are said to be lost from the ion beam, and cannot contribute to the ion current at the detector. Figure 5.4 shows the path length of ions as a function of frequency for three models of the omegatron. The ppc model represents the simplest configuration, where the omegatron is treated as an ideal parallel plate capacitor. The model named “ppc+beam”, has a column of charge added in the middle of the analyser region. The last model, “ppc+beam+damp” includes the damping terms that should be present to account for the interactions between the beam ions and the background gas. Near resonance at  $\omega_c = 9.6484 \text{ s}^{-1}$ , the ions travel a distance of approximately  $9 \text{ m}$ . As the difference between the radio



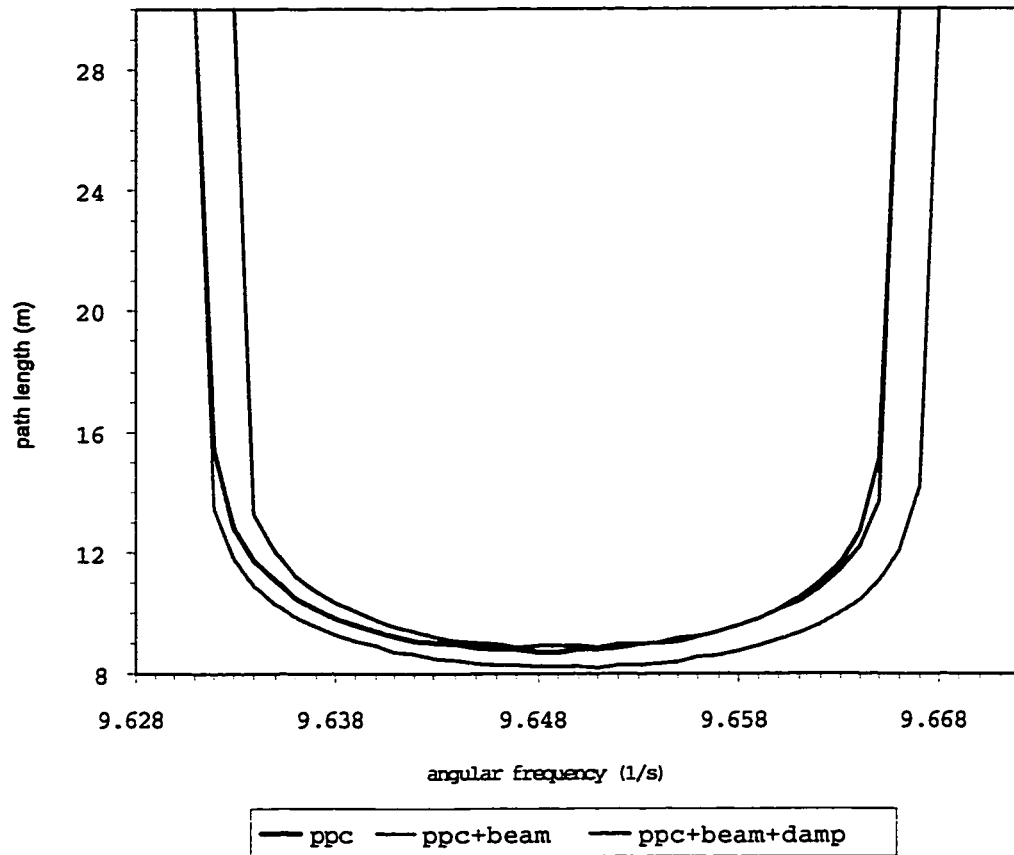


Figure 5.4: Graph showing the path length as a function of the applied angular frequency. Comparison of the ideal ppc in red, the ppc with the column of charge shown in green, and the ppc with the column of charge and the damping term in yellow.

frequency electric field and the resonance frequency,  $\kappa = |\omega_c - \omega_{RF}|$ , increases, the path length increases. This increase is gradual to the point where the path length almost doubles. For slightly greater values of  $\kappa$  the path length increases more rapidly. As one would expect, the ions no longer reach the detector when  $\kappa$  passes some critical value,  $\kappa_{crit}$ . The critical value depends on the amplitude of the electric field, the magnetic flux density, and the mass of the ions. To create a peak shape, this condition can be expressed as the ions having an infinitely long path length for  $\kappa > \kappa_{crit}$ . The models that include the column of charge show a shift away from the cyclotron frequency. This does not indicate that the ions now have a single new frequency of precession about the field lines. Since the electric field of the electron beam decreases with the distance that an ion is removed from it, the frequency to accelerate an ion at its resonance would also change throughout the trajectory. One does in fact need a frequency band (centered at the peak centre) to accelerate the ions at resonance. Figures 5.5 and 5.6 are two representations of the same peak shape calculations. The mean-free path for these models was taken to be 20% of the minimum path length of the “ppc” model. Figure 5.5 shows the relationship between the expected heights for the three models. As discussed earlier, the “ppc+beam” model, results in shorter trajectory path lengths, thus the probability of detecting these particles must be higher. The model that includes the damping term, still has the shifted resonance frequency but it shows that the damping results in an increase of the path length. Another notable difference, that is best seen in the normalized plot in Figure 5.6, is that the undamped motion with the electron beam results in a wider peak (lower resolution) than without the damping. Including damping into the model results in a narrowing of the peak as well as a reduction of the

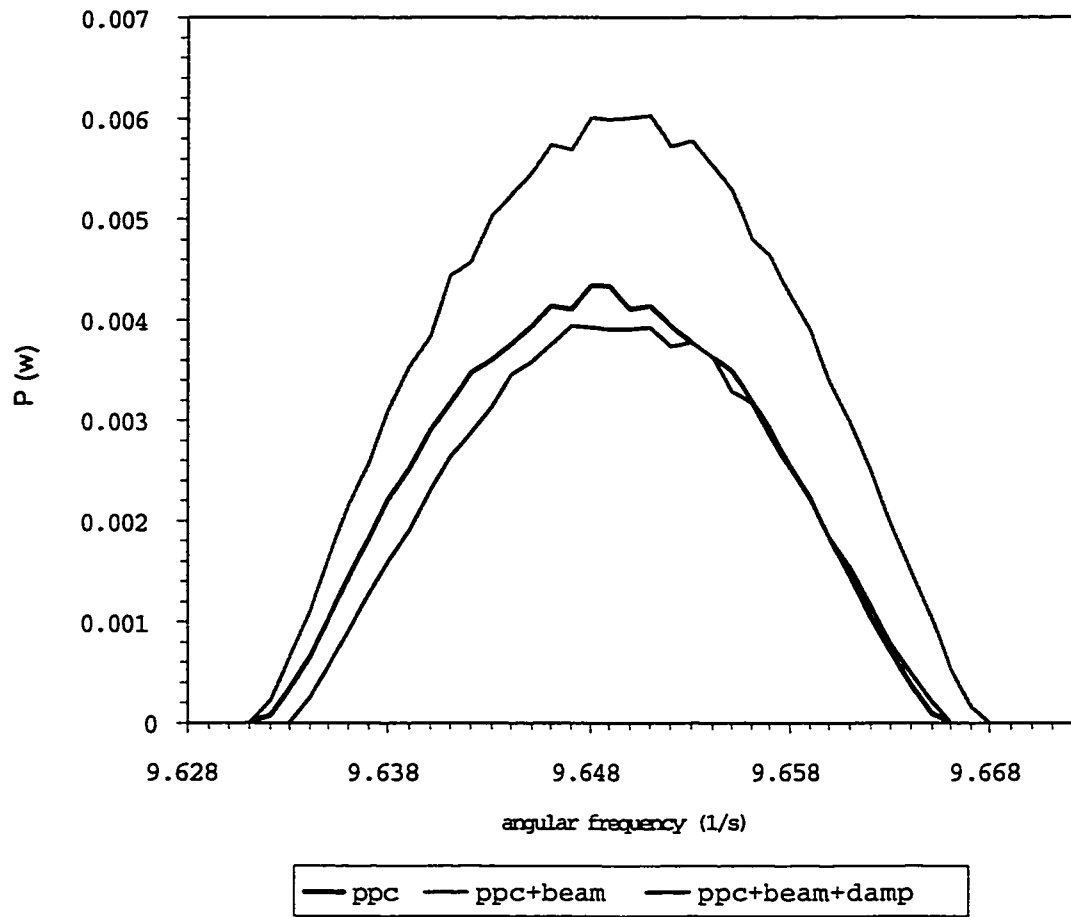


Figure 5.5: Probability of particles reaching the detector as a function of the applied angular frequency for a mean-free path that is 20% of the minimum path length. Comparison of the ideal ppc, the ppc with the column of charge, and the ppc with the column of charge and the damping term.

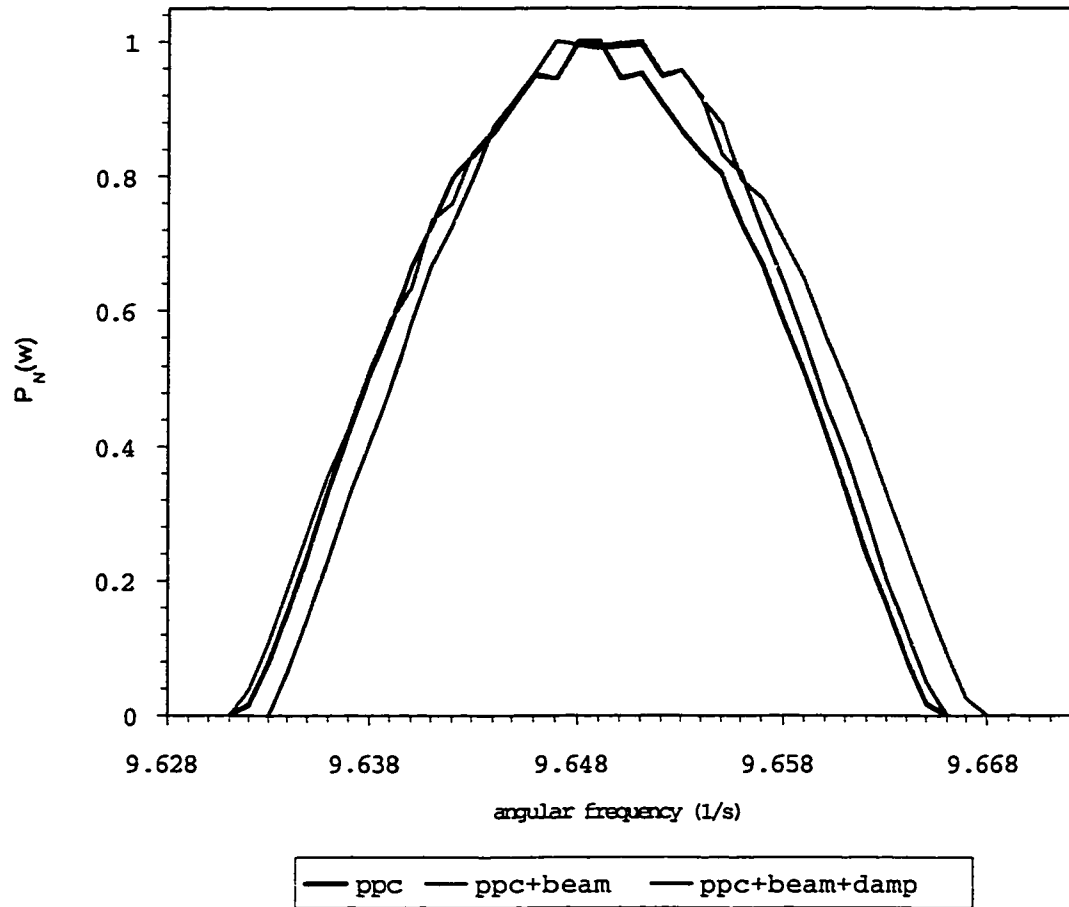


Figure 5.6: Normalized probability of particles reaching the detector as a function of the applied angular frequency for a mean-free path that is 20% of the minimum path length. Comparison of the ideal ppc, the ppc with the column of charge, and the ppc with the column of charge and the damping term.

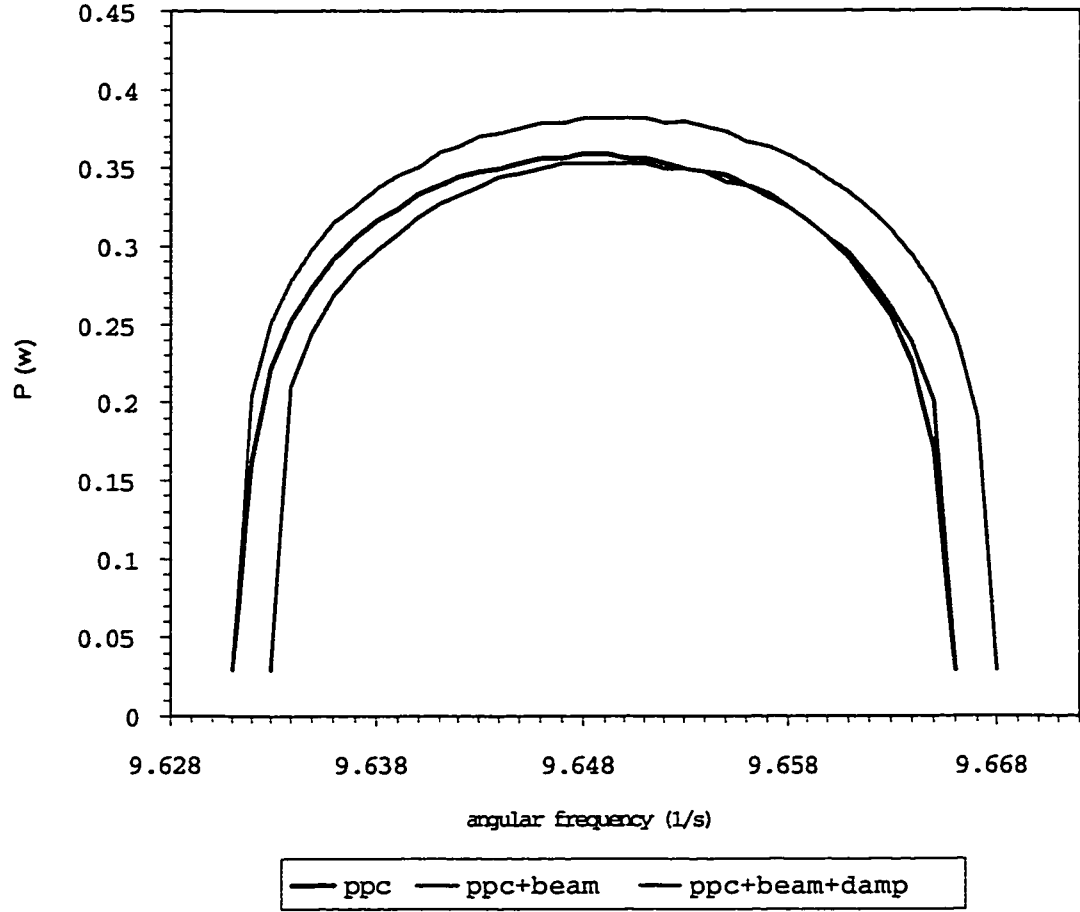


Figure 5.7: Probability of particles reaching the detector as a function of the applied angular frequency for a mean-free path that is 100% of the minimum path length. Comparison of the ideal ppc, the ppc with the column of charge, and the ppc with the column of charge and the damping term.

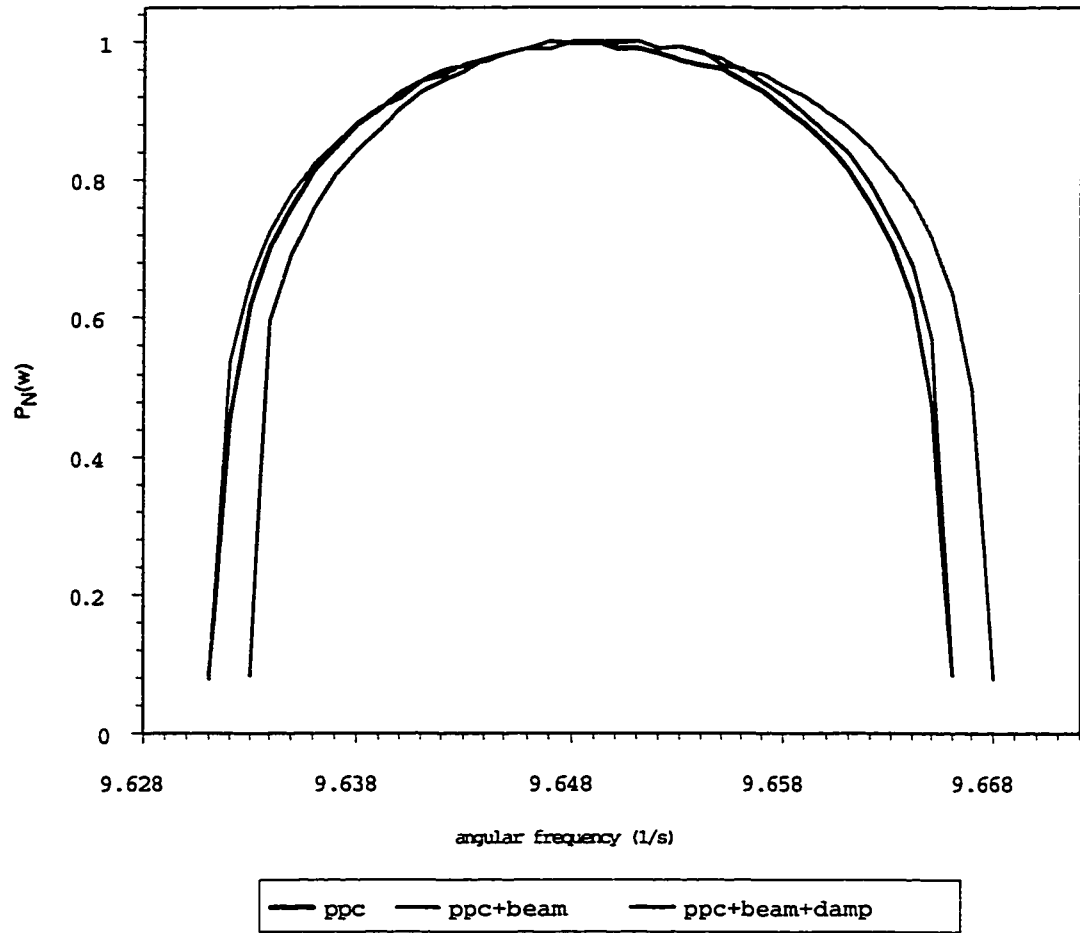


Figure 5.8: Normalized probability of particles reaching the detector as a function of the applied angular frequency for a mean-free path that is 100% of the minimum path length. Comparison of the ideal ppc, the ppc with the column of charge, and the ppc with the column of charge and the damping term.

probability of the particles reaching the detector. For the case that a collection of particles are part of the beam at all times, the reduced probability translates into a reduced ion current. If one defines the resolution to be the ratio of the full width of a peak at half maximum height and the centre frequency, then the resolution of the “ppc+beam” simulation is 402, the “ppc” peak has a resolution of 459, and the “ppc+beam+damp” shows a resolution of approximately 522. For the test particle of  $10^7$  atomic mass units, the next closest isotopes that would be resolved under the current conditions, would be  $2 \times 10^4$  mass units removed. A smaller accelerating voltage would further improve the resolution but it would also increase the path length and decrease the number of ions that reach the detector. Thus the sensitivity would be decreased.

A second situation, where the mean free path is of the order of the path length that the particles traverse is shown in Figures 5.7 and 5.8. The changes of the peak shape between the three models are comparable to those seen for the previous examples. The mean free path is now set equal to the minimum path length. The peaks are well rounded, and the sides of the peaks drop almost vertically. The resolution suffers in that the “ppc+beam” resolution has become 273, the “ppc” resolution became 295, and the “ppc+beam+damp” resolution was reduced to 309. These results are consistent with data that are obtained for small detector distances.

## 5.4 Realistic Electric Potential Fields

The omegatron is finite in extent, and deviations from the ideal field configuration are expected. In section 3.4, the electric potential field distribution for ideal parallel

plate capacitors is shown. The degree to which these deviations occur is a limiting factor to the maximum resolution that is attainable. This has been experimentally confirmed. When the detector mounting block was  $2.5\text{ cm}$  wide, it was not possible to resolve all the krypton isotopes. Upon milling away the bulk of the material, leaving a  $0.9\text{ cm}$  wide detector mount, the krypton isotopes were easily resolved. One can create accurate three-dimensional models of complicated electric potential fields with a number of algorithms. For this work, the VLUGR3<sup>3</sup> algorithm by Bloom and Verwer [55] was used. Although this program is able to solve time dependent IVP-ODE systems, for the purpose of this work, it was used as a time-independent boundary value solver in three dimensions with pre-defined grid sizes.

The VLUGR algorithm requires that the dimensions of any feature in the calculation volume span at least two grid points. Thus, the true dimensions of the omegatron were approximated for the program to properly interpret the information. For this reason, the detector size was over estimated by a factor of about 2, and the size of the detector mount was rounded to the nearest grid-points. For the x-direction, 31 grid points spanned the  $9\text{ cm}$  length of the omegatron, the  $4\text{ cm}$  height (y-direction) contained 41 grid-points, and the  $3\text{ cm}$  depth (z-direction) 16 grid-points. The coordinate system is not the same as that discussed in previous chapters. Rather, the axes are rotated so that the RF electric field points in the y-direction, with the magnetic field pointing in the z-direction.

The first computations with a large collector mount, revealed that the mount affected the electric potential fields strongly, and the field lines were curved far into the analyser region. Figure 5.9 shows the electric potential field lines at two central

---

<sup>3</sup>Algorithm 759, Transactions of Mathematical Science (TOMS), NETLIB.



planes through the omegatron. Along with the curvature of the fields, a second, undesired effect arises from the finite size of the omegatron. Along the y-direction, the distance between the electric field lines varies. Near the edges the distances are smaller than near the middle. The slice of the y-z plane shows why the field distribution is not uniform. Figure 5.10 shows how the electric potential fields have changed with the smaller collector mount. The curvature of the field lines is now significantly reduced. With this change, the resolution of the omegatron improved by a factor of about three.

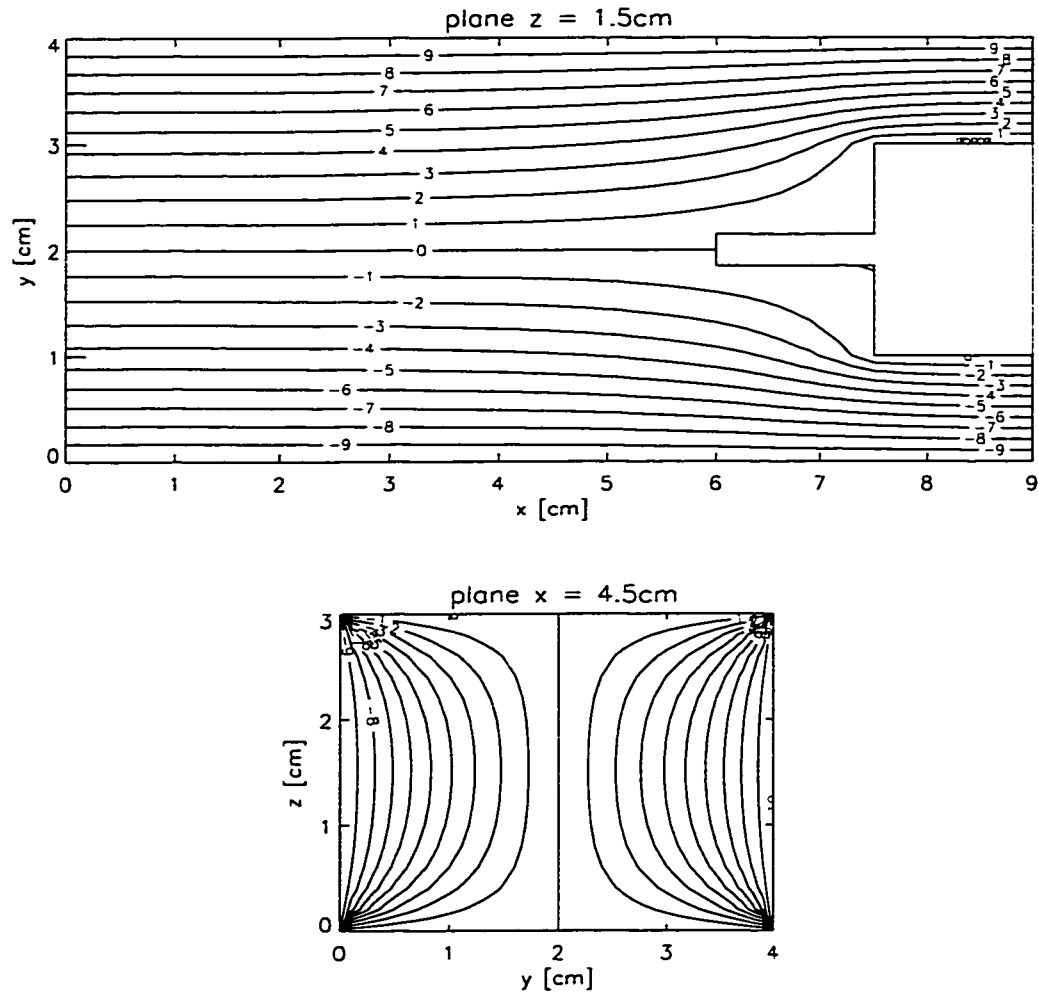


Figure 5.9: Contour plot of a cross section of the equipotential planes inside a finite three dimensional omegatron. The presence of the detector mount and the detector between the RF-plates (right side of top view), strongly distorts the equipotential planes. The numbers shown reflect the potential ( $V$ ).

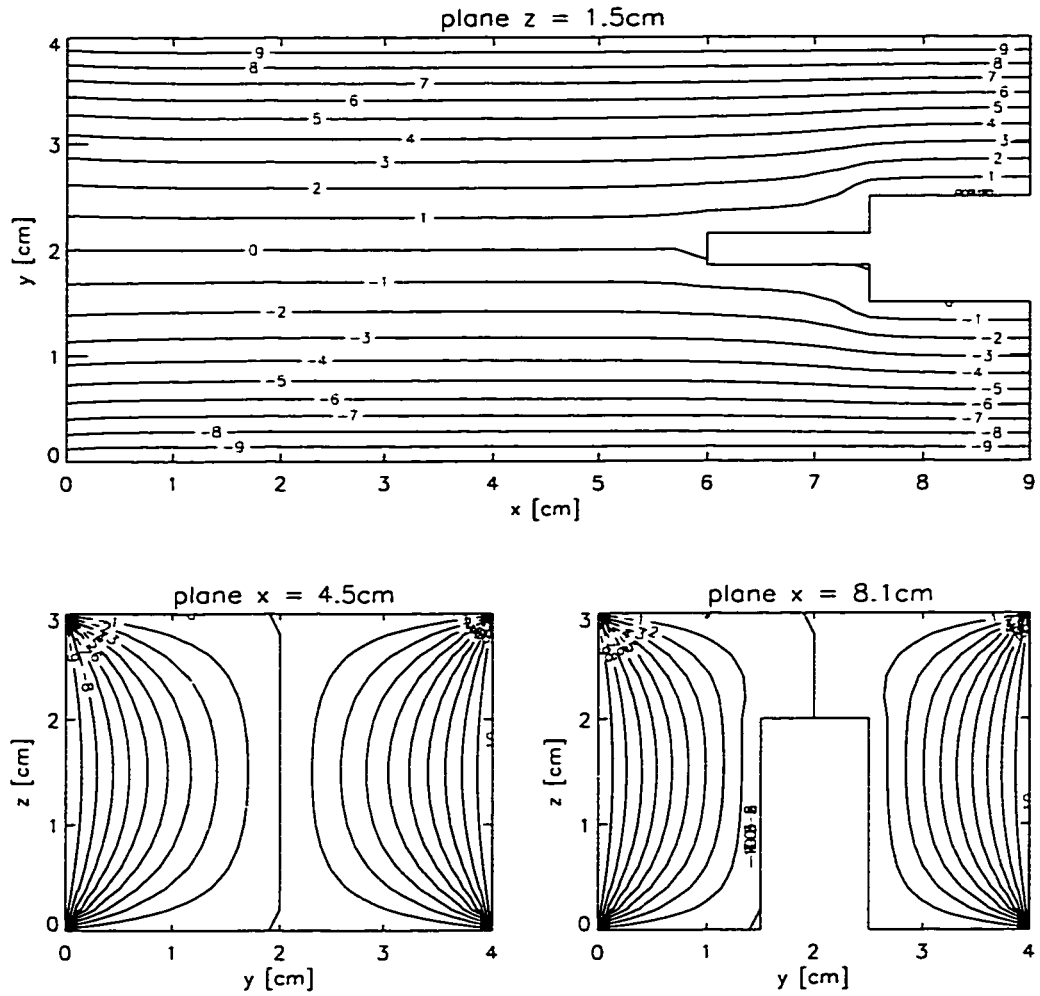


Figure 5.10: Contour plot of the equipotential planes inside a finite three dimensional omegatron. A smaller detector mount on the right side of the top view, results in the field geometry approaching that of the ideal omegatron. The non-linear distribution of the fields due to the finite extent did not change. The numbers shown reflect the potential ( $V$ ).

## Chapter 6

### Obtaining and Analysing Omegatron Spectra

The theory governing the operation of the ideal omegatron can explain the basic operation of the constructed instrument. Even with a very basic instrument there are procedures required including alignments of the electron beam parallel and the acceleration fields perpendicular to the magnetic field. Space charge effects and ion velocities parallel to the magnetic field should be addressed with additional experimental procedures in order to realize more effective operation.

#### 6.1 Alignment with the Magnetic Field

The initial, rough alignment of the omegatron was performed by visual inspection. Thereafter, the radio frequency accelerating voltage was set to the maximum (22 V), and the trapping potential was set to obtain a high ion current. Next the omegatron was moved until a maximum ion current was reached. The trapping potential and acceleration potentials were decreased and the alignment was adjusted to maximize the ion current again. This process was repeated until adjustment in any direction resulted in a decrease of the ion current.

## 6.2 Reducing Ion Loss due to Motion Parallel to the Magnetic Field

Thermal energy results in the ions possessing velocity components that are parallel to the magnetic field lines. Without constraining the motion of these ions within the analyser region, most of these ions would be lost, as their motion parallel to the fields would cause them to impact the walls of the omegatron. At  $300\text{ K}$ , the thermal motion of a nitrogen molecule would carry it across the  $3\text{ cm}$  depth of the analyser region in under  $0.1\text{ ms}$ . The cyclotron frequency of a molecular nitrogen ion is  $270\text{ kHz}$ . Thus, it takes the ion about  $4\text{ }\mu\text{s}$  to complete one revolution. Typically, to obtain good resolution, the ion must perform between one hundred and several thousand revolutions and travel for a duration of the order of milli-seconds. The thermal velocity of a large portion of the ions would cause them to be lost. An electric trapping potential parallel to the magnetic field [14], [40] and [42] may be used to trap the ions.

For this work, the trapping potential was adjusted for each sample and acceleration potential, to maximize the ion current. In this manner the conditions in the omegatron were optimized for each sample.

## 6.3 Reducing Space Charge Effects

Space charge buildup, that arises from the accumulation of non-resonant ions around the electron beam, has the potential to reduce the sensitivity of the omegatron. A number of different methods to reduce the space charge have been suggested [14], [56], and [45]. The two methods that may be applied with the current design are the

application of a DC voltage pulse between the RF acceleration plates to purge the analyser prior to ion current measurements and the second method is by applying a small DC voltage superimposed on the RF frequency signal to continuously drive non-resonant ions out of the region. These methods may be employed independently, or simultaneously, as conditions require.

## 6.4 Data Acquisition Procedure

The computer algorithm that controls the acquisition of the data, has been programmed for the Windows95 32-bit operating system. This operating system was chosen since it is relatively user friendly and allows the parallel execution of two routines (threads) within one program <sup>1</sup>. The use of threads provides an easier method to program a data acquisition routine that provides the user with a real-time interface to control the measurement process. To achieve this, the program has been coded such that the acquisition thread is continuously executed. A second thread contains the interface dialog that allows the user to intervene in the execution of the acquisition thread. The third thread updates the display, to show the progress of the measurements. Figure 6.1 is a flow chart of the information exchange between the threads of the program.

The acquisition thread is organized so that first, the mass spectrometer interface is initialized. This includes the initialization of the fiber-optic interface, the voltage to frequency converters, and the signal generator.

---

<sup>1</sup>The execution is not parallel in the sense that the program statements of both routines are not executed simultaneously. Simultaneous execution would require multiple micro-processors. Rather, the routines time-share the existing micro-processor.

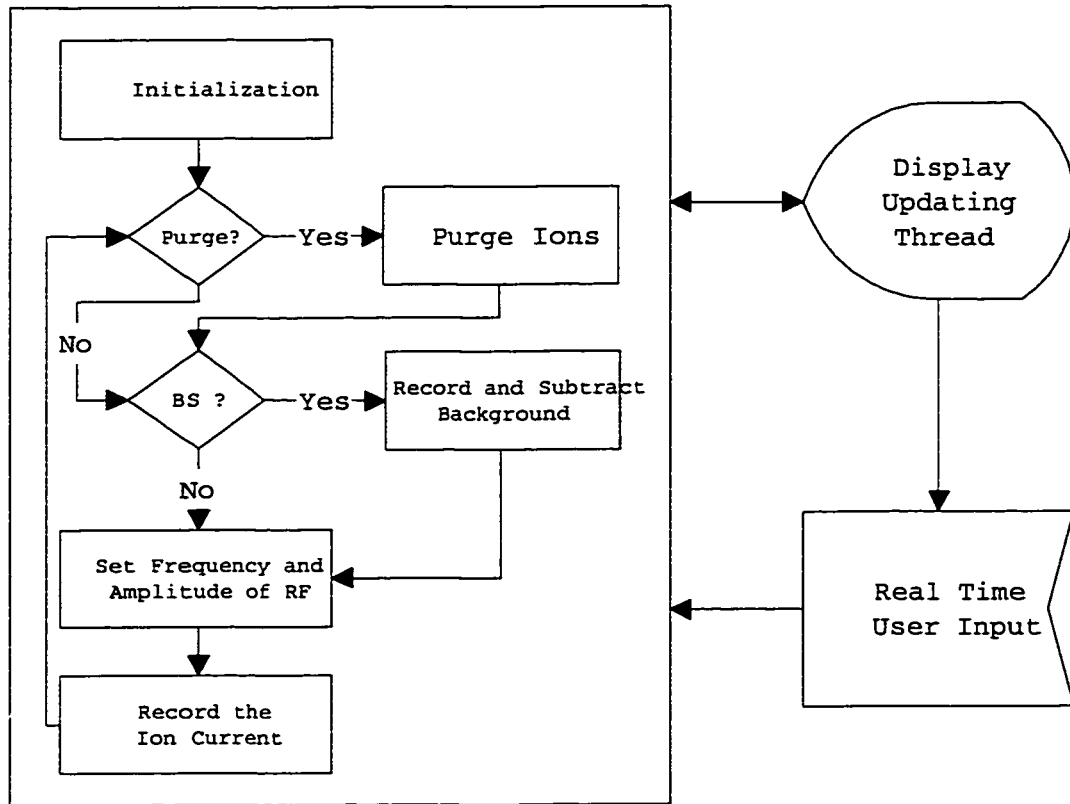


Figure 6.1: Flow chart showing the interaction and data flow paths between the acquisition, the real-time control, and the display update threads.

Before each measurement is started, a DC voltage of the order of  $20\text{ V}$  may be used to purge the analyser region of ions. Following this purging pulse, the background current that appears due to amplifier offset and noise may be measured and subtracted. Next, the frequency and amplitude of the RF signal are set. After a short delay to allow the signal generator to settle, the current measurement is started. The measurement is averaged over a set time, then the process is repeated at discrete frequency increments until the spectrum is scanned.

The frequency and a number proportional to the ion current at that frequency are recorded for each frequency step. During subsequent scans, the ion current data

are binned with the corresponding frequencies.

## 6.5 Data Analysis

The data consist of a number of frequency scans, where the ion current is recorded at discrete intervals. The data are binned according to their frequencies. Averages and standard deviations that are estimates of the precision of the measurements are calculated. Figure 6.2 shows successive frequency spectra gathered for neon. With these data, a suitable method of analysis must be found. The methods that

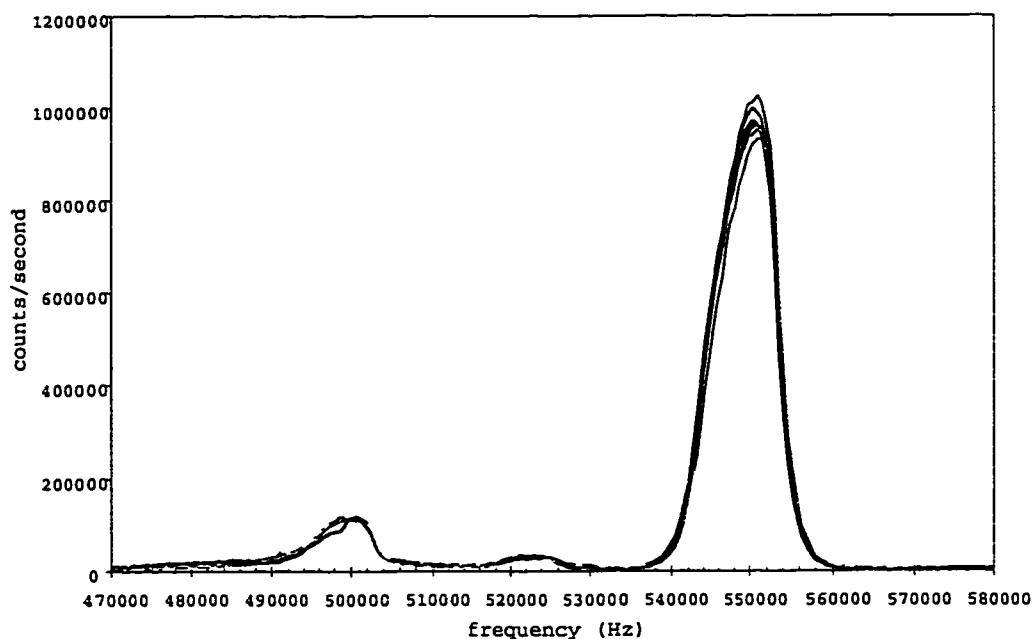


Figure 6.2: Diagram of successive frequency scans during the acquisition of a neon spectrum. Starting from the left, the peaks are  $^{22}\text{Ne}$ ,  $^{21}\text{Ne}$ , and  $^{20}\text{Ne}$

are available for the determination of the percent isotope abundances integrate the areas under the peaks and divide each by the sum of all peak areas. In an analogous fashion, the maximum height for each peak can be used to determine the abundances.



The latter method is employed for the determination of isotope abundance ratios in conventional magnetic sector mass spectrometers, where the peaks have a flat top (shown in Figure 4.4). Mass spectra that are obtained with the omegatron, do not have flat topped peaks. Typical shapes are seen in Figure 6.2. Locating the maxima of the peaks is not trivial. With the use of discrete frequency steps for a mass scan, it is not likely that one step will be located at the exact resonance frequency of a peak. Furthermore, the exact resonance frequency of a given charge to mass ratio is dependent on the magnetic field, trap current, and the gas pressure in the instrument. All these factors make it difficult to use the maximum peak height for the determination of isotopic abundance ratios.

The peak areas are not as dependent on the location of the frequency steps with respect to the peak centre. As more data are available with this method, the precision with which one can determine the abundances is better.

To determine the area under a peak, one needs to know two parameters. The easiest to determine is the background level. The background may be determined by averaging the ion current on both sides of a peak. A more difficult parameter is the peak width. For a finite, clearly defined peak (dark shaded region of Fig. 6.3), the tail regions are quite small and determining the area under the peak is trivial. Integrating the area under the peak and subtracting the background area yields the correct results. Inspections of the peaks in Fig. 6.2, shows that the peaks are unsymmetric with extended tail regions and noise is present. The start and end of a peak now becomes a judgment call. For peaks such as these, a variety of criteria are used to determine the peak-width. Spectroscopists sometimes use the full-width at half maximum height, at other times the width of a peak is said to

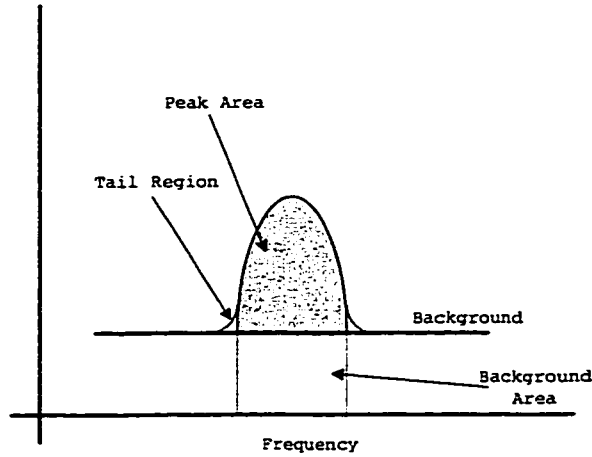


Figure 6.3: Diagram of the approximate peak shape. Calculation of the peak-area involves consistently defining the background and tail regions.

be the point at which the peak reaches one percent of its maximum height. The start and end of a peak may also be determined using statistical criteria. Given the noise levels present in the omegatron data, using a greater portion of the peak statistically reduces measurement errors. A problem arises when one approaches the background and noise is mistaken for data. To balance these considerations, the data are analysed such that the peak-width is defined by the two points where the peak decreases to 10 percent of its maximum height with respect to the background.

To estimate the precision of a ratio, one may use the variances of the measurements collected for each frequency. The data obtained are paired as a number that represents the average ion current at one frequency,  $x_i$ , and the standard deviation,  $\sigma_{x_i}$ , of the currents at that frequency. To calculate the area,  $A_k$ , of a peak of isotope,  $k$ , one adds the data

$$A_k = \sum_i x_i, \quad (6.1)$$

where  $i$  are the frequency bins that comprise the peak width. An estimate of the

maximum error of the data may be obtained by expanding the previous equation as a Taylor series and taking the sum of the squares of the first order terms to be the variance of the peak area,

$$\sigma_A^2 = \sum_i \sigma_{x_i}^2. \quad (6.2)$$

Although calculating the peak areas in this manner may introduce significant systematic errors, these are virtually eliminated with the use of the  $\delta$ -scale. Abundance ratios and their errors required for the calculation of  $\delta$ -values are given by

$$R_{k,l} = \frac{A_k}{A_l} \quad (6.3)$$

$$\sigma_{R_{k,l}} = \sqrt{\left(\frac{\sigma_{A_k}}{A_l}\right)^2 + \left(\frac{A_k \sigma_{A_l}}{A_l^2}\right)^2}, \quad (6.4)$$

where  $A_k$  and  $A_l$  are the two peak areas. By the same method, an error estimate for  $\delta$ -values is

$$\sigma_\delta = 1000 \frac{R}{R_{ref}} \sqrt{\left(\frac{\sigma_R}{R}\right)^2 + \left(\frac{\sigma_{R_{ref}}}{R_{ref}}\right)^2}, \quad (6.5)$$

where the  $R_{ref}$  is the isotope abundance ratio of the reference (standard), and  $\sigma_{R_{ref}}$  is its error estimate and  $R$  and  $\sigma_R$  are the abundance ratio and error estimate of the sample.

## Chapter 7

### Results and Discussion

In this chapter, the performance of the omegatron is described in terms of consistency with theory and limitations imposed by components and other phenomena in the instrument. Higher resolution is achieved at lower masses as derived by Sommer *et. al.* [14],

$$\frac{M}{\Delta M} = \frac{qB^2r}{2E_{RF}m}. \quad (7.1)$$

This concept was tested by trying to resolve  $H_3^+$  and  $HD^+$  at mass 3. To evaluate the instrument in more general terms, spectra of rare gases were obtained since they offer several advantages. Chemical interactions should be minimal and a wide range of masses is available. Adjacent isotopes (as found for Kr and Xe) allow better estimates of resolution. An unexpected outcome was production of  $KrH^+$ .

#### 7.1 Performance Limitations Imposed by the Quality of the Components and Other Phenomena

For any instrument, performance is limited by the most unstable component. For example, the latter's characteristics may be altered significantly by changes in temperature, humidity, and line voltage. An instrument may also be stable but possess undesirable qualities such as non-linearity.

Stability of any mass spectrometer can be considered in terms of two aspects (1)

stability of electric and magnetic fields which is important for mass determinations and resolution and (2) stability of ion currents which is important for isotope abundance measurements. The latter may be influenced by the former as is the case of overlap of ions with nearly the same  $q/m$  ratio e.g.  $T^+$ ,  $HD^+$ ,  $H_3^+$ ,  $^3He^+$ .

The frequency of the electric field was adjustable by 0.1  $Hz$  increments, implying that the stability is better than this. Thus for the case where the lowest frequency used is about  $10^5 Hz$ , the uncertainty in frequency should be better than 1 in  $10^6$ . The field homogeneity of the electromagnet according to the manufacturer's specifications, should be better than 1 in  $10^5$  over the analyser region. The stability of the external magnetic field over time is of the same order. Experimentally at mass 3, a shift of 3 parts in 20000 for the resonant frequency (Figure 7.1) corresponds to an uncertainty of 2 parts in  $10^5$  for the magnetic field.

The integrating transimpedance amplifier was compared to a typical operational amplifier (LM128) used on conventional sector isotope ratio mass spectrometers. On the basis of comparing the DC source settings with digital multimeter output readings, departures from linearity were less than 1 part in  $10^4$  over the input range of  $10^{-14} A$  to below saturation ( $10^{-8} A$ ) [57]. Without gas present, the maximum variation in the electron beam current was  $\pm 0.2\%$ . This specification should be put into the context of the electron current being only  $10^{-6} A$  i.e. the regulation [58] is to  $\pm 10^{-9} A$ . The requirement of the low electron current to minimize electric field distortion is therefore the limitation in abundance measurement precision. It is noted that the magnetic field of the electron beam is of the order of  $10^{-6}$  of that of the applied field and is therefore not a significant factor. It is also interesting to note that with this emission control design the percentage variability of electron beams

(up to  $500\ \mu\text{A}$ ) in a magnetic sector mass spectrometer is much lower.

The uncertainties in ion currents can be reduced by repeated frequency scans as shown in the next section.

Measurement of sensitivity was thwarted by problems in pressure measurement. To measure the pressure inside the vacuum chamber, a Penning gauge was attached to it using a 1.33" flange and a 10" long 3/4" diameter stainless steel pipe. Penning gauges directly rely on a magnetic field to perform pressure measurements. The 12" Harvey Wells electromagnet that provides the magnetic field for the omegatron, produced a stray magnetic field that interfered with the operation of the gauge (Magnetic fields sufficient to affect the operation of a computer monitor were observed as far as 1.5 metres from the magnet). Since a pressure gauge attached by a long narrow pipe to the chamber would not correctly display the chamber pressure, a longer tube was not used. It is the author's understanding that any device that ionizes a part of the gas in a chamber and measures the current, such as Penning gauges and Ionization gauges will be susceptible to magnetic fields. Instruments which might not be affected, such as thermocouple gauges and capacitance manometers are not capable of measuring pressures in the high and ultra high vacuum ranges. Thus pressures and changes thereof could only be crudely estimated.

Pressure changes of the gas inside the omegatron affect its operation by changing the mean free path of the ions. As the pressure changes, the radio-frequency and the trapping potentials may need to be adjusted for optimum operation. The numerical solutions suggest that any change to the mean free of the ions will affect the peak shape and the peak height. The effects of pressure change are not due solely to collision phenomena. Schuchhardt [37] suggested that the density and thus

the pressure of the gas determines the nature of a cloud of space charge generated upon ionization by the electron beam. This cloud of charge can interfere with the operation of the omegatron. Interestingly, Engelmann *et. al.* [45] state that the resolution reducing effects of the electron beam may be offset and even balanced by the space charge. At a critical pressure, electrostatic shielding of the space charge should negate the electric field of the electron beam. An additional problem with the space charge is that it causes diffusion of charged-particles normal to the magnetic field. This implies that as this charge density changes, so will the diffusion of charged-particles. The motion of particles normal to the magnetic field contributes to the background current that can be measured with and without the application of the radio frequencies to the omegatron. The combination of all of these phenomena reduces the reproducibility of measurements.

## 7.2 Resolution of $H_3^+$ and $HD^+$

It is well known that in electron impact sources of magnetic sector mass spectrometers,  $H_3^+$  is formed during ionization of  $H_2$  and increases with  $H_2$  pressure. Its current is typically 10% of that of  $HD^+$ .  $H_3^+$  is also generated in omegatrons but in much larger relative quantities (approximately 2:1 in Figure 7.2). These two species are ideal for determining resolution at low mass. With his available instrument, Gentsch [54] could detect  $H_3^+$  but it was not satisfactorily resolved from  $HD^+$ . Engelmann *et. al.* [45] resolved doublets of  $H_2^+$ ,  $D^+$  and  $D_2^+$ ,  $HT^+$  but did not examine  $H_3^+$ .

With the omegatron described in this thesis, the doublet is clearly resolved as shown by the “corrected” spectrum in Figure 7.1. The masses of the two species

are  $3.0235 \text{ amu}$  for  $H_3$  and  $3.0218 \text{ amu}$  for  $HD$ . To completely resolve the two ion species, a resolution of at least 1952 at mass 3 is required. With the electric and magnetic field settings used for Figure 7.1, the instruments FWHM resolution was 6300. Higher resolutions are achievable if sensitivity is sacrificed. Figure 7.2 shows

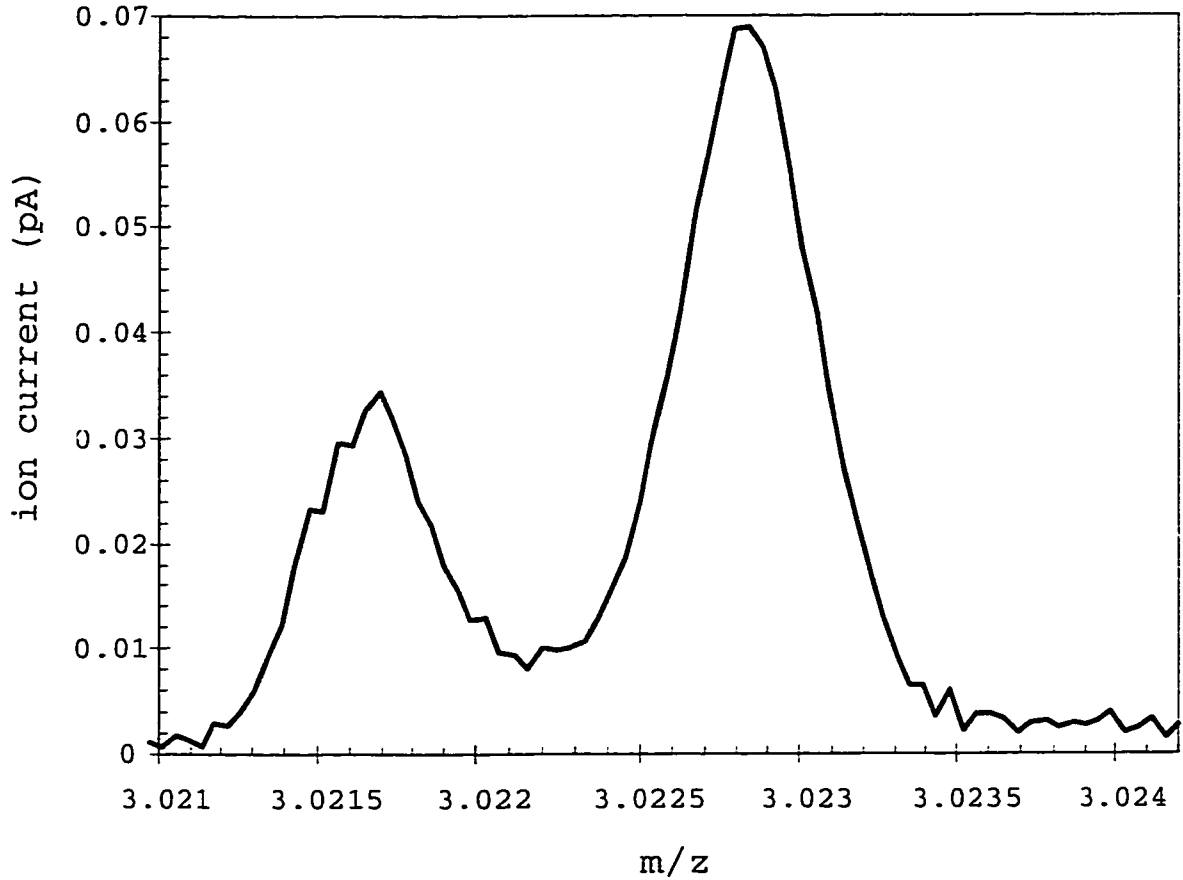


Figure 7.1: Plot of the  $H_3^+$  and  $HD^+$  mass peaks resolved by the omegatron with a magnetic flux density of approximately  $1.12 \text{ T}$  and a radio frequency accelerating electric field of  $125 \text{ V/m}$ .

the individual frequency scans that were averaged to obtain the spectrum shown in Figure 7.1. A correction was applied to compensate for the frequency “drift” of the spectra and align the peaks. The “drift” appears to stem from a gradual change in



the magnetic field. This change is likely a result of the extremely long times required for the magnet and power (both have large thermal masses) supply to reach thermal equilibrium when operating near maximum capacities ( $B = 1.2\text{ T}$ ). A decrease of the

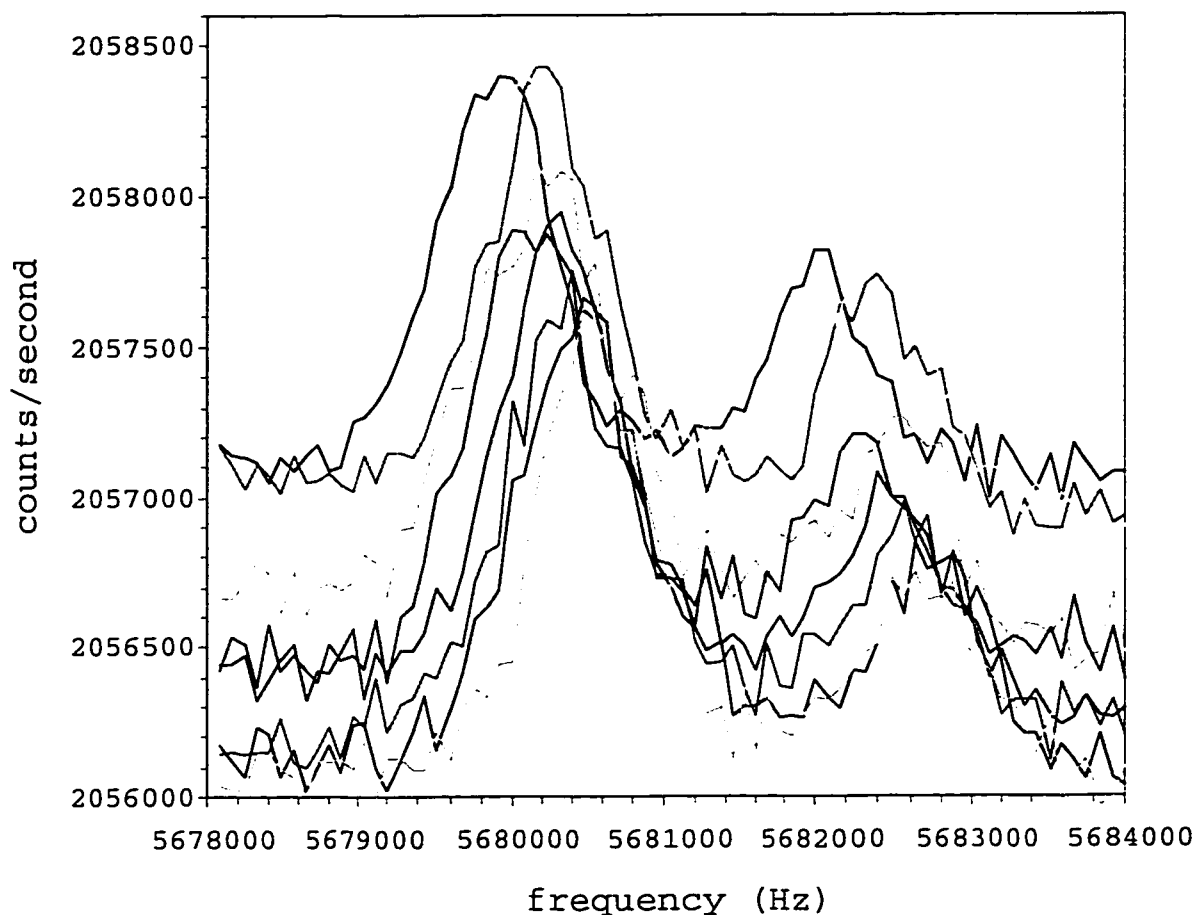


Figure 7.2: Example of the frequency shift observed due to a slow drift of the magnetic field for  $H_3^+$  and  $HD^+$  peaks.

baseline and corresponding increase of the peak height is also seen with time. These changes are a result of a slight decrease of the pressure of the sample gas, since the vacuum chamber was continuously pumped, and the sample was leaked through a capillary into the instrument. This is evidence that at lower pressure there are fewer

collisions with the ions and hence more reach the detector.

It is also important to note that the separation between  ${}^3\text{He}^+$  and  $\text{HD}^+$  is about three times that between  $\text{HD}^+$  and  $\text{H}_3^+$ . However,  $\text{T}^+$  separation from  ${}^3\text{He}^+$  requires about 25 times the resolution obtained to date.

## 7.3 Mass Spectra of Noble Gases

Up to now, the mass spectrum of  $\text{He}$  was not obtained because  ${}^3\text{He}$  has an average abundance of only  $10^{-6}\%$ . In principle, detection of  ${}^3\text{He}^+$  should be possible by increasing the amplitude of the RF during its analysis and decreasing the RF amplitude during detection of  ${}^4\text{He}^+$ .

### 7.3.1 Neon

Neon spectra are easily resolved at magnetic flux densities as low as  $0.4\text{ T}$  and electric field strengths of the order of 25 to  $225\text{ V/m}$  (Figure 7.3). Lower electric field strengths can be used, but are only needed if other interfering mass peaks are present and must be resolved.

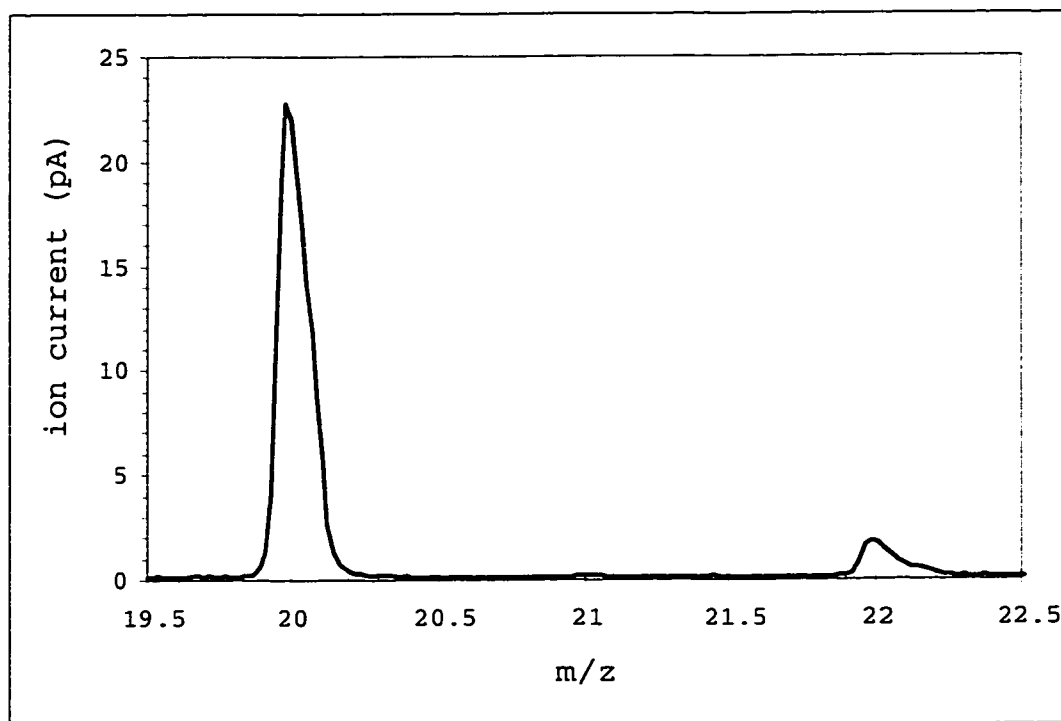


Figure 7.3: Neon isotope spectrum. All three stable isotopes are visible even though the  $^{21}\text{Ne}^+$  peak almost vanishes in the background, and the peaks are asymmetric.

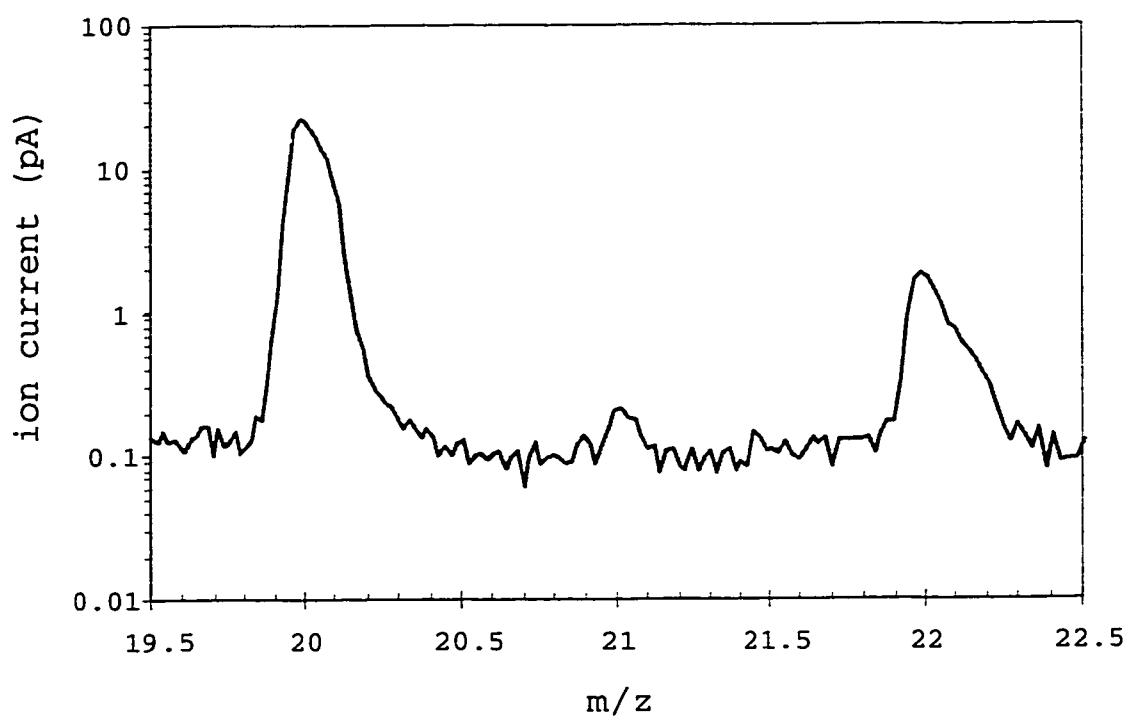


Figure 7.4: Semi-logarithmic graph of the neon spectrum shown in Figure 7.3. Here the  $^{21}\text{Ne}^+$  peak is clearly visible.

### 7.3.2 Argon

Argon isotopes were also readily resolved with magnetic flux densities as low as  $0.4\text{ T}$  and electric field strengths of  $25$  to  $225\text{ V/m}$ . The logarithmic plot of the spectrum of the Figure 7.6 makes the  $^{36}\text{Ar}^+$  ( $0.327\%$  abundant) peak more evident whereas the peak of  $^{38}\text{Ar}^+$  ( $0.063\%$ ) is lost in the noise. Selective changes to the radio frequency acceleration potential can enhance the mass  $^{36}\text{Ar}^+$  and  $^{38}\text{Ar}^+$  peaks. Although it cannot be stated for certain, the clearly visible peak at mass  $41$  may be  $\text{ArH}^+$  since  $\text{ArH}$  and other noble gas hydrides are known to exist. See also section 7.4.

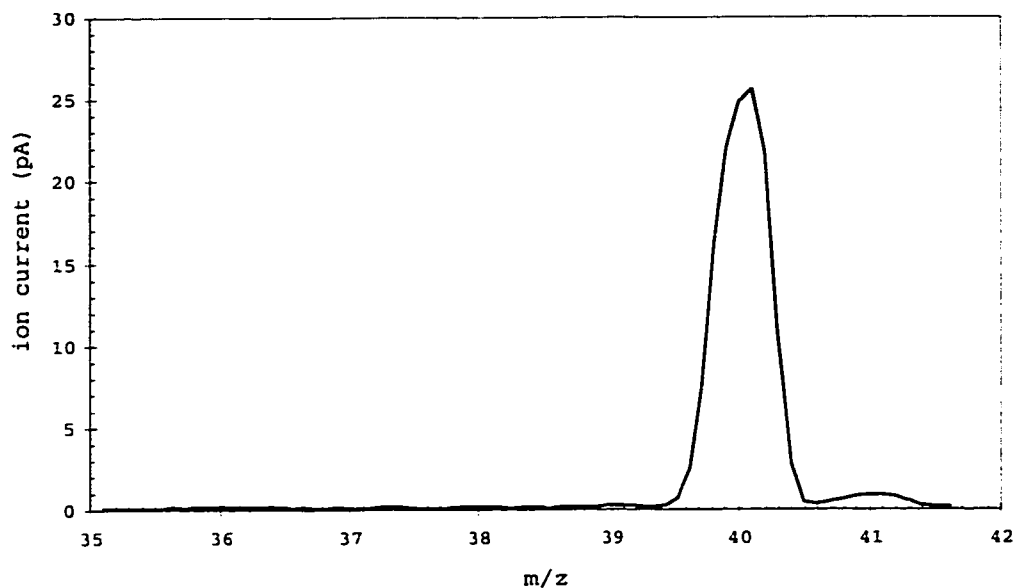


Figure 7.5: Mass spectrum of Argon. Only the dominant  $^{40}\text{Ar}$  peak is clearly visible for the particular instrumental settings.

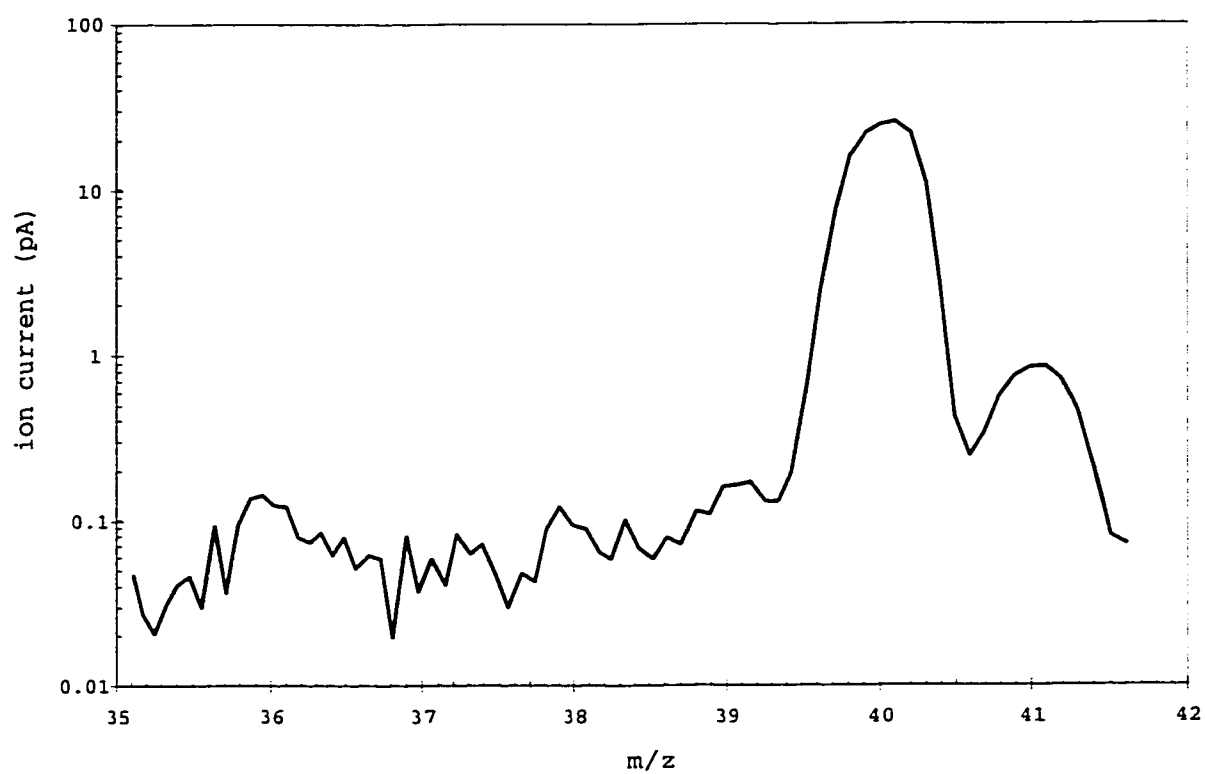


Figure 7.6: Semi-logarithmic graph of the argon spectrum shown in Figure 7.5. The  $^{36}\text{Ar}^+$  peak is barely visible.

### 7.3.3 Krypton

Isotopes of krypton could be readily resolved with a magnetic flux density of  $1\text{ T}$  and lower electric field strengths ( $1$  to  $10\text{ V/m}$ ). Computational models in chapter 5 showed that the peak shapes are dependent on the mean-free-path of resonant ions in the instrument. The predictions of these computations were verified with  $Kr^+$  spectra. The spectrum in Figure 7.7 was obtained with a small collector distance and hence a relatively short path length to reach the detector. The shapes of these peaks is comparable to those theoretically generated in Figure 5.8 in that the tops of the peaks are rounded and the sides are very steep. With the collector set at a

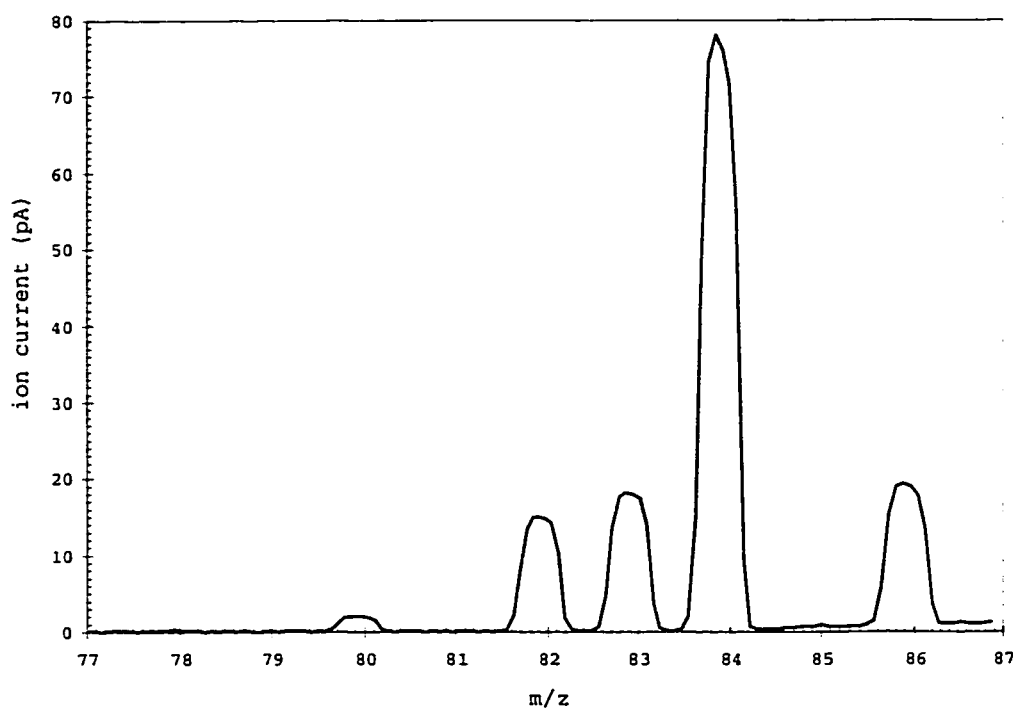


Figure 7.7: Krypton isotope spectrum measured with an ion collector distance of  $1.3\text{ cm}$  from the electron beam. The peak tops are rounded and the sides rise rapidly.

distance of  $1.8\text{ cm}$  from the centre of the analyser the krypton spectrum seen in Figure

7.8 was obtained. The noteworthy changes are a substantial decrease in the peak height, narrower resonance peaks, and a more triangular peak shape that compares well to those modelled in Figure 5.5 where the path length is long compared to the mean-free-path.

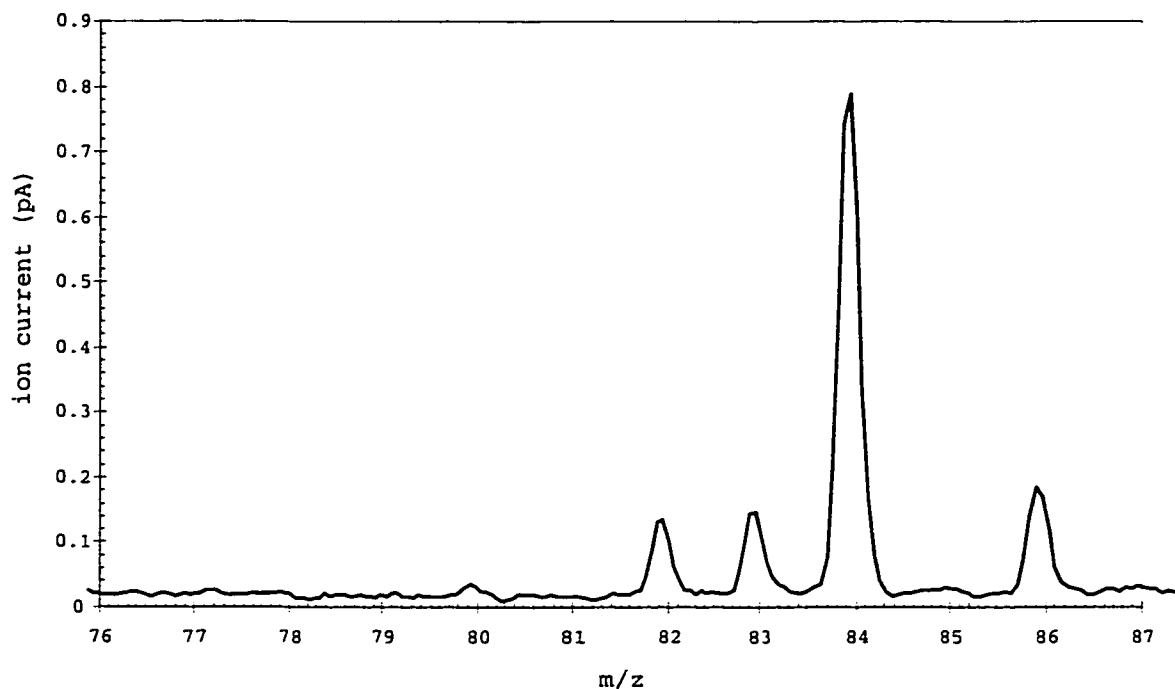


Figure 7.8: Krypton isotope spectrum with the ion collector at a distance of 1.8 cm from the electron beam. Sharp peak tops with smoothly rising sides are observed.

As found with Ne, a plot of the logarithm of the ion currents enhanced the visibility of a very low abundant peak, in this case  $^{78}\text{Kr}$  (0.35 %) as shown in Figure 7.9.



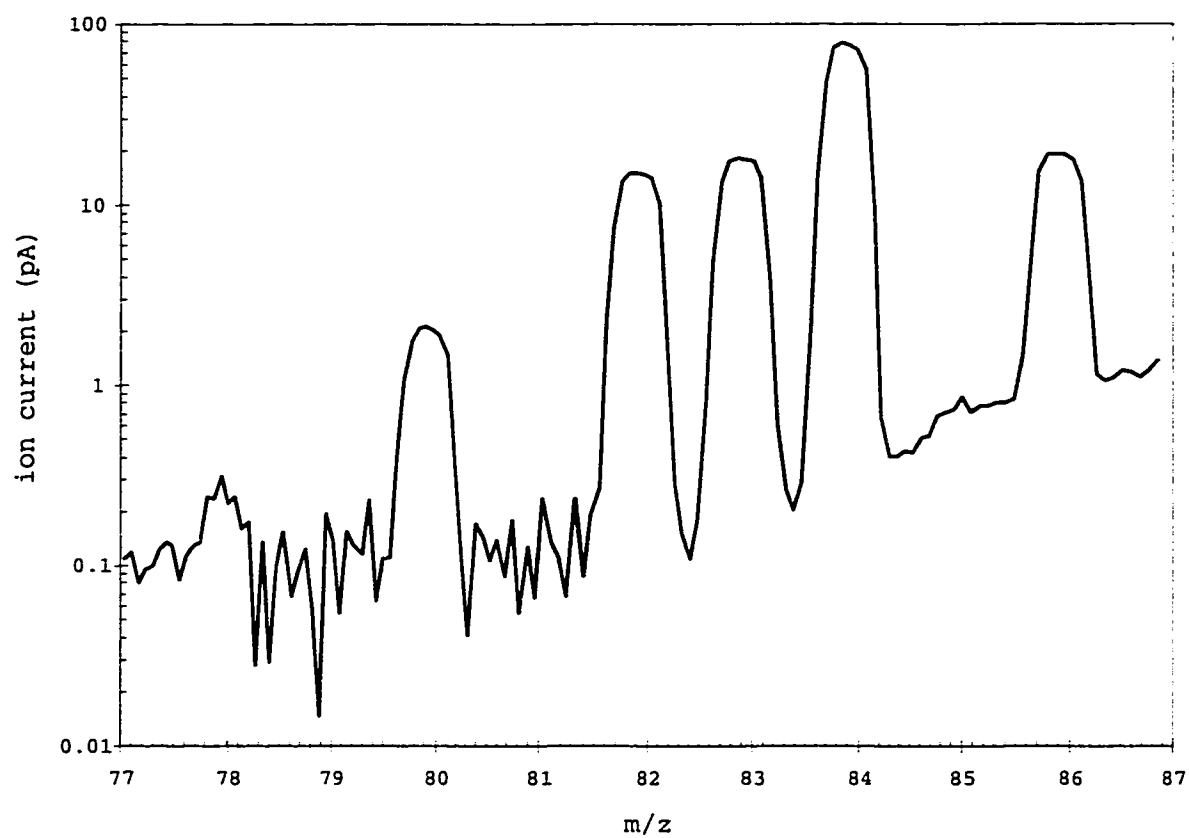


Figure 7.9: Semi-logarithmic graph of the krypton isotope spectrum shown in Figure 7.7. The change in scale, allows the identification of the  $^{78}\text{Kr}$  mass peak.

### 7.3.4 Xenon

The xenon isotopes were almost completely resolved using a magnetic field of  $1.12\text{ T}$  and electric field strengths of  $1$  to  $10\text{ V/m}$  (Figure 7.10). The lowest abundance

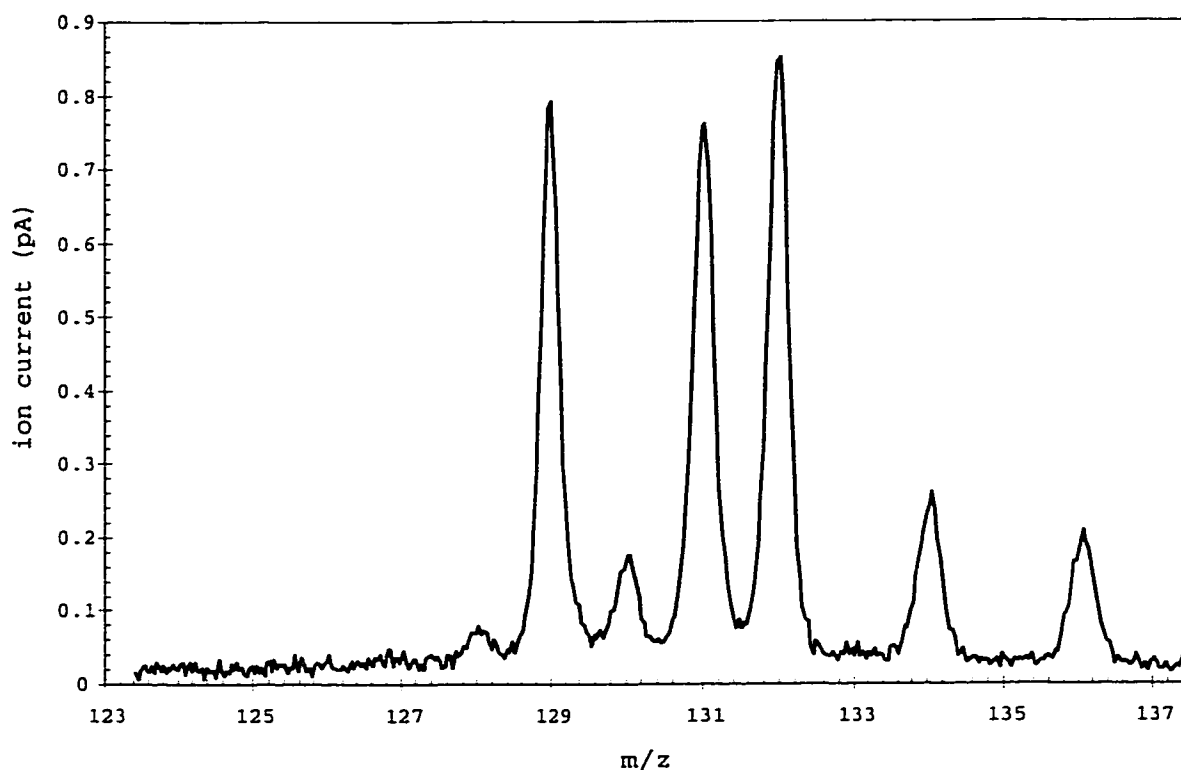


Figure 7.10: Xenon isotope spectrum. At high magnetic flux densities ( $1.12\text{ T}$ ) and low acceleration potentials the Xenon isotopes are almost completely resolved.

peaks ( $^{124}\text{Xe}^+$ ,  $0.1\%$ ;  $^{126}\text{Xe}^+$ ,  $0.09\%$ ) cannot be detected in the baseline noise with these instrumental settings.

## 7.4 Formation of $\text{KrH}^+$

An extremely interesting spectrum was obtained by admitting krypton gas that had previously been in contact with water into a chamber that had previously held

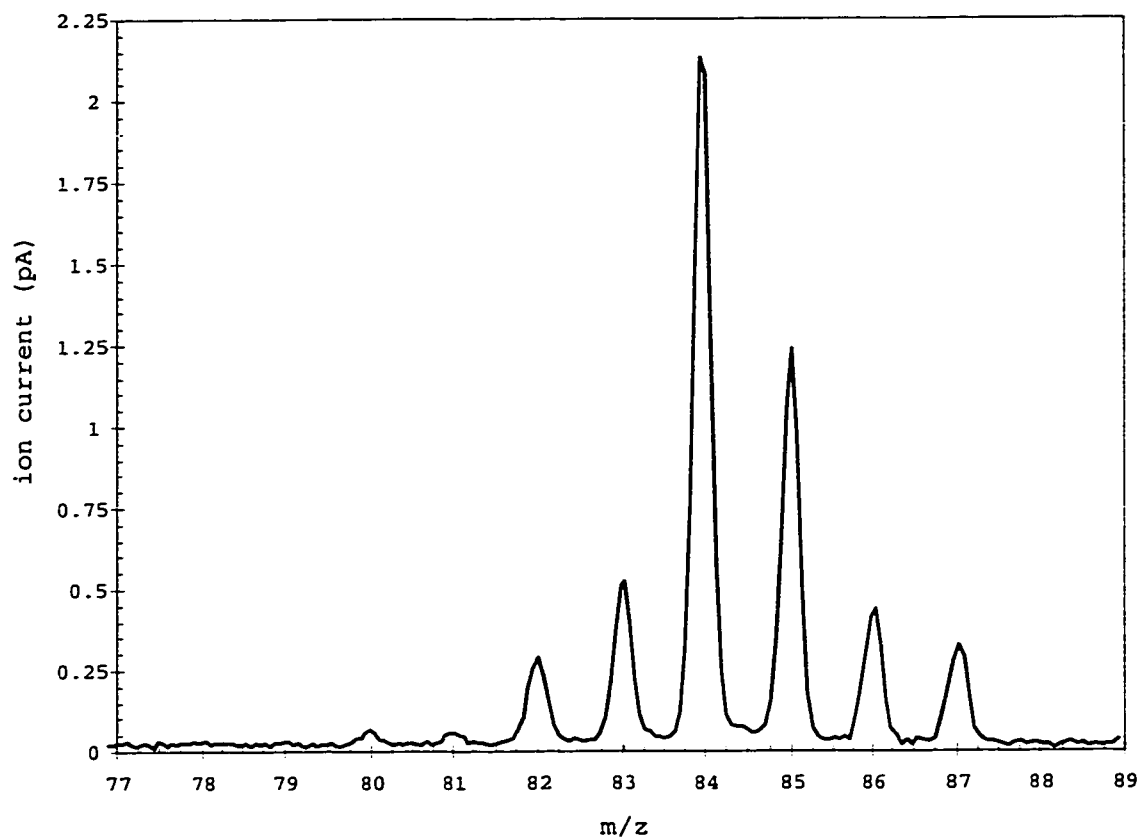


Figure 7.11: Spectrum observed after admitting krypton gas that contained some water vapour into the sample storage bellows and vacuum chamber that previously contained hydrogen gas. The additional peaks that occur one atomic mass unit higher than the krypton isotopes suggest that this mass spectrum most likely corresponds to a mixture of  $Kr^+$  and  $KrH^+$ .

$H_2$  (Figure 7.11). It is likely that significant levels of  $H_2$  were still present, as a turbo molecular pump was being used temporarily to evacuate the instrument. These pumps are well known for back streaming of hydrogen (motion opposite to the direction of pumping). Examination of the spectrum reveals that (1) some of the mass peaks of krypton at masses 83 and 84 are not present in the usual proportions relative to the peaks at mass 80 and 86 and (2) additional mass peaks that are heavier by one mass unit are present. The explanation for this spectrum must be

that krypton chemically combined with  $H_2$  (and/or<sup>1</sup>  $H_2O$ ) at some time between being admitted to the system and reaching the collector. In view of the observation of the high relative abundance of  $H_3^+$  (section 7.2), when  $H_2$  was analysed, it would appear that  $H_2$  is quite reactive in the omegatron and was more likely the source of  $KrH^+$  than  $H_2O$ . If the krypton-hydride ( $KrH^+$ ) formed during the travel time of the ions from the electron beam to the collector, a broadening of the peaks at mass 81, 85, and 87 should be observed. The data do not show a significant change in the peak widths. It may thus be safe to assume that the molecules formed before, during or very shortly after ionization near the electron beam. Furthermore, peaks whose mass is two mass units heavier than those of krypton were not detected. This could indicate that  $KrH_2^+$  is not a stable ion.  $KrD^+$  was probably present but not detected because of the low abundance of deuterium. Historically the noble gases were considered as unreactive, and prior to the middle of this century there was no evidence or knowledge of noble gas compounds. In the 1960's, the discovery of noble gas compounds ignited a flurry of research [59], [60]. Hydrides are not stable in their ground states but potential energy minima in their excited electronic states allow their existence. Deprotonation energies for singly and multiprotonated species have been calculated by Boldyrev and Simons [61]. Spectroscopic studies on  $HeH^+$ ,  $NeH^+$ ,  $ArH^+$ ,  $KrH^+$ ,  $KrD^+$ ,  $XeH^+$ , and  $XeD^+$  have been performed by Johns [62], Dabrowski *et. al.* [63], and Dabrowski and Herzberg [64].

If one assumes that approximately 40% of the measured krypton reacted with

---

<sup>1</sup>Analyses performed between the writing of this thesis and the thesis defense suggest that the  $KrH^+$  was formed from the  $H_2$  gas. The same "wet" Kr gas was admitted into the analyser that had been evacuated for more than one week (the  $H_2$  was removed). Mass spectra thus obtained did not show high  $KrH^+$  generation.

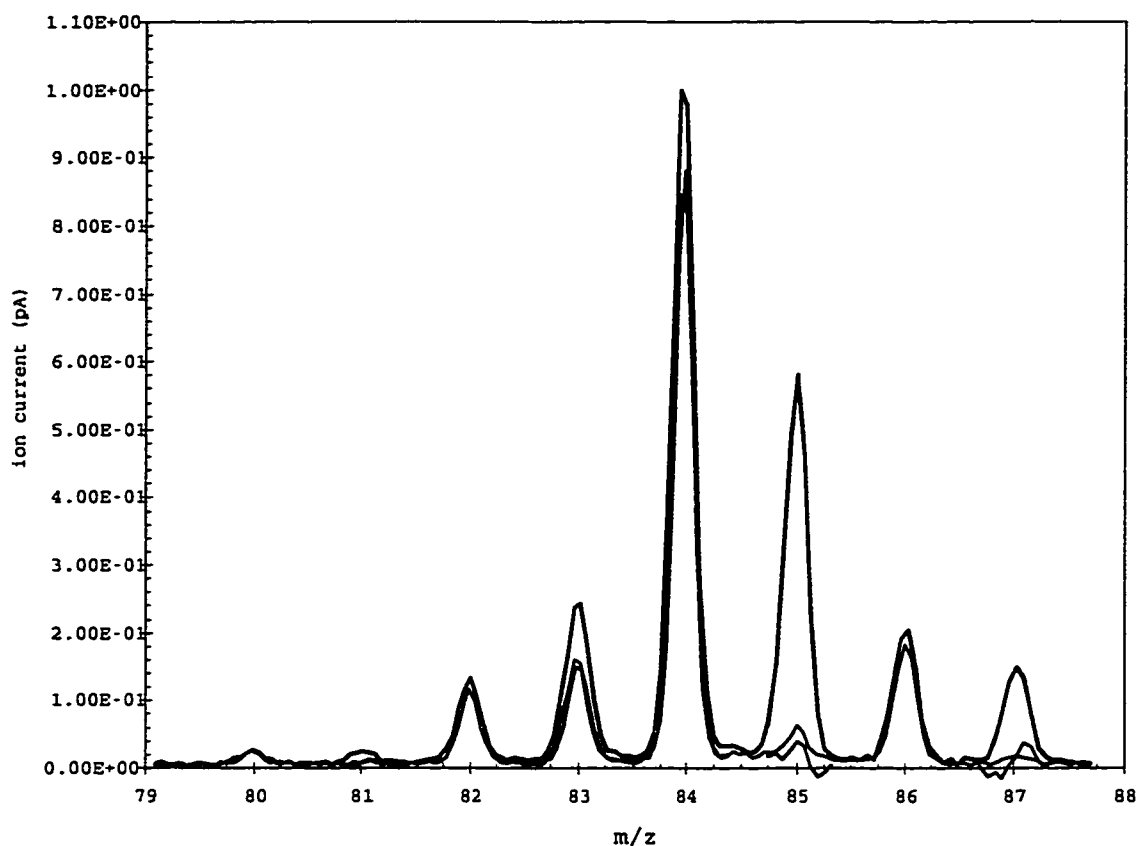


Figure 7.12: Comparison of  $Kr^+$  and  $KrH^+$  spectra. The spectrum in blue corresponds to the mixture of  $Kr^+$  and  $KrH^+$  ions. The spectrum in purple is that of  $Kr^+$  obtained earlier. The peaks coloured in green were obtained by assuming that 40% of the Kr reacted with the  $H_2$  and subtracting this contribution from the spectrum of the mixture.

hydrogen, one can perform a subtraction of the  $KrH^+$  data from the combined spectrum to see how closely the calculated abundances relate to those measured previously. Figure 7.12 shows the results of one such calculation. The spectrum coloured in green agrees quite closely with that coloured in purple. Slight differences in the resolution of the two spectra caused mismatch-errors at masses 85 and 87. Thus one can state with certainty, that the peaks are those of  $KrH^+$ .

The solubility of rare gases in water has been a matter of debate. Because of their

chemical inertness, the concept of water molecule “cages” (clathrate formation) has been postulated. In view of the above, one can ask whether inert gas hydride ions occur in water.

## Chapter 8

### Conclusions and Future Possibilities

Omegatrons have been built and theoretically analysed previously. Omegatron performance has also been compared to that of magnetic sector instruments. The question arises as to what is different and/or novel in this thesis.

This instrument has incorporated features of several different omegatron designs. Separately, open designs without end plates, simple designs without guard rings, and collectors located in the mid-plane between the radio frequency plates have been used. Another difference is that this instrument has superior electronics to those built three to four decades ago. The quartz crystal stabilized electron emission supply and transimpedance amplifier are innovations developed in the Stable Isotope Laboratory at the University of Calgary. Also of great importance is the interfacing of the instrument to a computer to realize unprecedented instrument control and data acquisition.

One desirable consequence of the computer interfacing is that theoretical modelling of performance can be compared to actual operation in greater detail than hitherto realized. Evaluation of modifications to the instrument can be accomplished with relative ease.

In terms of comparison of the omegatron with magnetic sector instruments, it is appropriate to note that the instrument of this thesis was built in a laboratory with three decades of experience in building and operating the latter (with a supervisor having over four decades of such experience).

The computational peaks are a reasonable approximation to those observed. The tails of the peaks are wider in the observed spectra. These might be explained by a model that includes collisions where the beam ions are not electrically neutralized, but are accelerated for a second time (with a different center of motion) in the region between the electron beam and the collector. Such ions, could still reach the detector even if the frequency difference between the applied electric field and the ion's resonance frequency is large. Determining computational spectra that include the more realistic potential fields, may yield insight into the asymmetries of resonance peaks.

The electric fields within the instrument are critical to its operation. Reducing the size of the collector mounting block resulted in a great improvement in the instrument's resolution. It stands to reason that further reducing the size of this mounting block would increase the maximum achievable resolution, provided that the collector is mechanically rigid. The thickness of the insulators that are inserted into the block present a lower limit to its size.

From Figure 5.10 one can see that due mainly to the finite size of the omegatron, the electric potential lines are not homogeneous. Creating a network of potential dividers that present discrete voltage steps near the walls along the y-direction would remove the complex pattern that is visible in the y-z plane and make the fields more homogeneous. Any curvature of these fields that is created by the collector mount would still be present. By placing a part of this potential divider in front of the mount, the analysing region could be shielded. These improvements would allow resolution of masses heavier than xenon (136 amu).

Higher resolutions are attainable by reducing the electric field (Equation 7.1) but



the reduction of the sensitivity causes low abundance mass peaks to vanish in the baseline noise. For the purpose of abundance determinations this is not appropriate. For mass determinations and identification of interfering mass peaks this may at times be useful.

An interesting feature of the operation of the instrument concerns the trapping potential that is applied parallel to the magnetic field (Section 6.2). Larger peak heights (instrumental sensitivity) at large electric field strengths are observed at lower trapping potentials (between 1 and 1.5 volts). When smaller electric fields are used to accelerate heavier ions, this trapping voltage must be increased to approximately 4.5 volts for maximum sensitivity. The optimum trapping potential is also dependent on the sample pressure and the electron beam [54],[40],[65], [43]. Quantitative data for these parameters is not supplied because exact pressure measurements were not possible (see below).

Of all the trapping schemes described in the literature, one stands out in that it is possible to discriminately trap ions of certain charge to mass ratios, whereas other ions are ejected from the analyser region [56]. Instead of a DC trapping potential, an AC trapping potential is used. The ions oscillate in harmonic motion parallel to the magnetic field. An AC trapping field of the same frequency as that of the harmonic motion will trap specific ions. Those with different charge to mass ratios will not have the same frequency of motion and are ejected. Adapting the current instrument to this type of trapping would provide a greater mean-free-path of the beam ions. A reduction of the baseline noise may also be achieved by modulating the radio-frequency electric field [66], and using a phase sensitive detector to de-modulate the ion beam signals. Another alternative is to modulate the electron beam.

For measurements of isotope abundance ratios and of small quantities of gas, it is advisable to operate the omegatron such that it is isolated from the vacuum pumps, with the sample contained in the vacuum chamber that houses the instrument. This static mode of operation requires that no vacuum leaks are present. Even in the absence of leaks the pressure inside the analyser is likely to rise. The tungsten-alloy electron emission filament is known to produce  $H_2$ ,  $H_2O$ , and  $CO_2$  [42]. Fragmentation of these molecules will also produce  $H^+$ ,  $C^+$ ,  $O^+$ ,  $OH^+$ , and  $CO^+$ . The metal surfaces of the stainless-steel vacuum chamber are also known to outgas. Keeping the pressure low may be accomplished with a getter pump that will trap the reactive gases. Inert gases will not react chemically with the getter-material e.g. titanium. As a third alternative, one may reduce the problem by increasing measurement speeds at the cost of precision and sensitivity.

The suitability of omegatrons to isotope abundance measurements has been confirmed by Galkin and Fedorov [67]. To be able to isotopically compare standards to unknowns, both must be admitted alternately into the omegatron under the same conditions. To achieve this, a switchable dual inlet system with two stainless steel bellows that can store samples and change their pressures may be used as done successfully with magnetic sector mass spectrometers for over four decades.

In terms of measuring small differences in isotope abundance ratios for many elements, traditional as well as more recently developed continuous flow IRMS (Isotope Ratio Mass Spectrometry) featuring simultaneous collection of two or more ion currents in a magnetic sector instrument, is superior. Such instruments are usually set up with fixed collector slits for analyses of particular gases such as  $H_2$ ,  $N_2$ ,  $CO_2$ , and  $SO_2$ .

With an element containing many isotopes such as xenon, simultaneous collection of all ion species would unlikely be considered. The physical requirements of the individual slit assemblies would require a large high resolution instrument. Hence it is much more likely that mass spectra would be generated by scanning the magnetic field or the source electric field using a single collector. The former is slow because of hysteresis. Scanning the source electric field changes the energy of the ions which is acceptable if only one element is examined. However this proves problematic if there is a need to scan a wide mass range such as *He* up to *Xe*. A combination of magnetic and electric field scanning would be required.

It is in the measurements of chemical and isotope abundances of several elements over a wide mass range that the omegatron becomes competitive and in some ways surpasses the capabilities of the magnetic sector instruments. The latter are fixed in resolution as determined geometrically by the source and collector slit widths and ion path radius (Equation 4.3).

The omegatron is unique in that its resolution is inversely proportional to the mass of the ions being analysed. Resolution of  $^3\text{He}^+$ ,  $\text{HD}^+$ ,  $\text{H}_3^+$ , etc., and hence determinations of *H* and *He* isotopes without interference, is realizable in a small sized instrument. Another distinct advantage of the omegatron is that “tradeoffs” among resolution, peak shape, and sensitivity can be realized electronically whereas physical changes inside the sector instruments are required to change these parameters.

In the case of rare gases there are large variations in the abundances of radiogenic isotopes. Hence the precision realized for omegatron ion current measurements is adequate. An obvious improvement for the current instrument would be higher magnetic fields. One could realize higher resolution which depends upon  $B^2$  (Equa-

tion 7.1) or alternately use larger RF electric fields to obtain higher sensitivity.

Thus, a few improvements have the potential to make the omegatron constructed for this work suitable to a wide variety of experiments and measurements with adequate precision.

## Bibliography

- [1] Piperov, N.B., Kamensky, I.L., and Tolstikhin, I.N., Isotopes of the light noble gases in mineral waters in the eastern part of the Balkan peninsula, Bulgaria, *Geochimica et Cosmochimica Acta*, **58**, No. 8, 1889-1898, 1994.
- [2] Hunziker, J.C. and E. Jäger, Potassium argon dating, **Lectures in Isotope Geology**, Springer-Verlag Berlin Heidelberg, pp. 51-76, 1979.
- [3] Dallmeyer, R.D., E. Jäger, and Hunziker, J.C.,  $^{40}\text{Ar}/^{39}\text{Ar}$  dating: principles, techniques, and applications in orogenic terranes, **Lectures in Isotope Geology**, Springer-Verlag Berlin Heidelberg, pp. 77-104, 1979.
- [4] von Grosse, A., On the origin of the actinium series of radioactive elements, *Physical Review*, **42**, 565, 1932.
- [5] Zartman, R.E. and Wasserburg, G.J., Helium, argon, and carbon in some natural gases, *Journal of Geophysical Research*, **66**, No 1, 277-306, 1961.
- [6] Schultz, L. and Kruse, H., Helium, neon, and argon in meteorites - A data compilation, *Meteoritics*, **24**, 155-172, 1989.
- [7] Hipple, J. A. , Sommer, H. ,and Thomas, H. A. , A precise method of determining the faraday by magnetic resonance, *Phys. Rev.*, **75**, 1877-1878, (1949).
- [8] Lichtman, D., Use of the omegatron in the determination of parameters affecting limiting pressures in vacuum devices, *Journal of Applied Physics*, **31**, No. 7, 1213-1220, 1960.

- [9] Rehkopf, C.H., Omegatron analysis of residual gases in receiving-type tubes., *Supplemento al Nuovo Cimento*, **1**, No. 2, 758-769, 1963.
- [10] van der Waal, J., Analysis of residual gases in T.V. picture tubes with the aid of an omegatron, *Supplemento al Nuovo Cimento*, **1**, No. 2, 760-769, 1963.
- [11] Della Porta, P., Giorgi, T, and Michon, L., The measurement of residual gases in electron tubes, *Supplemento al Nuovo Cimento*, **1**, No. 2, 458-469, 1963.
- [12] Batrakov, B.P. and Kobzev, P.M., Omegatron for high vacuum, *Pribory i Tekhnika Eksperimenta*, No. 4, 112-115, 1963.
- [13] Bloom, J.H., Ludington, C.E., and Phipps, R.L., The omegatron vs. a sector-type mass spectrometer for residual gas studies., *Supplemento al Nuovo Cimento*, **1**, No. 2, 442-451, 1963.
- [14] Sommer, H., Thomas, H.A., and Hipple, J.A., The measurement of  $e/M$  by cyclotron resonance, *Physical Review*, **82**, No. 5, 697, 1951.
- [15] Rankama, K., **Isotope Geology**, McGraw-Hill Book Co. Inc., London: Pergamon Press Ltd., p. 7, 1954.
- [16] Rolfs, C.E., and Williams, S.R., **Cauldrons in the Cosmos**, The University of Chicago Press, Chicago, 1988.
- [17] Burbidge, E.M., Burbidge, G.R., Fowler, W.A., and Hoyle, F., Synthesis of the elements in stars, *Rev. Mod. Phys.*, **29**, p. 547-648, 1957.
- [18] Gehrels, N. and Paul, J., The new gamma-ray astronomy, *Physics Today*, **51**, no.2, 26-32, 1998.

- [19] Rankama, K., **Progress in Isotope Geology**, John Wiley and Sons, New York, pp. 223-260, 1963.
- [20] Shukolyukov, Yu.A., Ashkinadze, G.Sh., Verkhovskiy, A.B., Dang Vu Min, Komarov, A.N., Levchenkov, O.A., Ovchinnikova, G.V., Pavshukov, V.V., Sprintson, V.D., and Yakovleva, S.Z., Isotope studies on the natural nuclear reactor, *GeoKhimiya*, No. 7, pp. 976-991, 1977.
- [21] Signer, P. and Nier, A.O., The distribution of cosmic-ray- produced rare gases in iron meteorites, *Journal of Geophysical Research*, **65**, No. 9, 2947-2964, 1960.
- [22] Linde, D.R., **CRC Handbook of Chemistry and Physics**, **74**, CRC Press Inc., Boca Raton, Florida, 1993.
- [23] Chen, F.F., **Plasma Physics and Controlled Fusion**, Vol.1: Plasma Physics, Ed.2, Plenum Press, NY, pp 176-183, 1984.
- [24] Zill, Dennis, G., **A First Course in Differential Equations with Applications**, PWS Publishers, Boston, pp. 160-170, 1986.
- [25] Anton, H., **Calculus**, Ed. 2, John Wiley and Sons, NY., pp. 532-555, 1984.
- [26] Jackson, J.D., **Classical Electrodynamics**, John Wiley and Sons, New York, N.Y., pp. 68-141, 1975.
- [27] Spitzer, L., **Physics of Fully Ionized Gases**, John Wiley and Sons, New York, pp. 121-153, 1962.
- [28] Goldston, R.J. and Rutherford, P.H., **Introduction to Plasma Physics**, Institute of Physics Publishing, London, pp. 147-246, 1995.

- [29] Duckworth, H. E. ,Barber, R. C. , and Venkatasubramanian, V. S. . *Mass Spectroscopy 2nd Ed.*,pp 45-48, Cambridge University Press, NY, 1990.
- [30] Langmuir, I. and Kingdon, K. H. , Thermionic effects caused by vapours of alkali metals, *Proceedings of the Royal Society of London, A*, **107**, 61, 1924.
- [31] Kanno, H. , Isotopic fractionation in a thermal ion source, *Bulletin of the Chemical Society of Japan*, **44**, 1808-1812, 1971.
- [32] Moore, L. J. , Heald, E. F. , Filliben, J. J. , , and Daly, N.R., An isotopic fractionation model for the multiple filament ion source, *Advances in Mass Spectrometry*, Vol 7A, pp. 448-473, 1978.
- [33] Bleakney, W. , A new method of positive ray analysis and its application to the measurement of ionization potentials in mercury vapor, *Physical Review*, **34**, 157-160, 1929.
- [34] Kerwin, L., Improved magnetic focusing of charged particles, *Rev. Sci. Instr.*, **20**,36, 1949.
- [35] Metcalf, G.F. and Thompson, B.J., A low grid-current vacuum tube, *Physical Review*, **36**, 1489, 1930.
- [36] Klopfer, A. and Schmidt, W., An omegatron mass spectrometer and its characteristics, *Vacuum*, **10**, 363-372, 1960.
- [37] Schuchhardt, G., Ion movements in an omegatron, *Vacuum*, **10**, 373-376, 1960.
- [38] Masica, B., A simple omegatron with additional trapping voltages, *Supplemento al Nuovo Cimento*, **1**, No. 2, 435-441, 1963.



- [39] Wang, E.Y., Schmitz, L., Ra, Y., LaBombard, B., and Conn, R.W., An omega-tron mass spectrometer for plasma ion species analysis., *Rev. Sci. Instr.*, **61**, No. 8, 2155-2158, 1990.
- [40] von Gentsch, H., Inertes Zyklotronresonanz-Massenspektrometer (Omegatron), *Vakuum-Technik*, **36**, No. 6/7, 224-229, 1987.
- [41] Bijma, J., The influence of a nonuniform RF field on the ion trajectories in an omegatron III: experimental verification, *Journal of Physics E: Scientific Instruments*, **6**, 759-764, 1973
- [42] Marklund, I. and Danielsson, M., Influence of collection efficiency on omegatron measurements., *The Review of Scientific Instruments*, **37**, No. 3, 319-325, 1966.
- [43] Brubaker, W.M. and Perkins, G.D., Influence of magnetic and electric field distribution on the operation of the omegatron, *The Review of Scientific Instruments*, **27**, No.9, 720-725, 1956.
- [44] Petley, B.W. and Morris, K., An Omegatron with linear orbit drift giving improved resolution without loss of sensitivity, *J. Sci., Instrum*, **42**, 492-494, 1965.
- [45] Engelmann, U., Glugla, M., Penzhorn, R.-D., and Ache, H.J., Application of an omegatron type high resolution mass spectrometer for the analysis of mixtures of hydrogen and helium isotopes., *Nuclear Instruments and Methods in Physics Research*, A302, 345-351, 1991.
- [46] Steckelmacher, W. and Buckingham, J.D., The design of a precision omegatron system, *Supplemento al Nuove Cimento*, **1**, No.2, 418-433, 1963

- [47] Alpert, D. and Burtiz, R.S., " Ultra-High Vacuum. II. Limiting factors on the attainment of very low pressures", J. Appl. Phys., **25**, 202-209, 1954.
- [48] Friedmann, J.B., Shohet, J.L. and Wendt, A.E., Ion-cyclotron-resonance mass spectrometry with a microwave plasma source, IEEE Transactions on Plasma Science, **19**, No. 1, 47-51, 1991.
- [49] Wieser, M.E., **Negative Ion Solid Source Mass Spectrometry of Boron Isotopes**, MSc. Thesis, The University of Calgary, 1994.
- [50] Berg, K., Wieser, M., Amerl, P., and Matlock, P., An inexpensive versatile multi-task PC interface for controlling isotope ratio mass spectrometers and preparation equipment, and data processing., The International Association of Geochemistry and Cosmochemistry Second International Applied Isotope Geochemistry Symposium, Lake Louise, Alberta, Canada, 1997.
- [51] Brankin, R.W. Gladwell, I., and Shampine, L.F., RKSUITE: a suite of Runge-Kutta codes for the initial value problem for ODEs, Softreport 92-S1, Department of Mathematics, Southern Methodist University, Dallas, Texas, U.S.A, 1992.
- [52] Brankin, R.W. and Gladwell, I., A Fortran 90 Version of RKSUITE: An ODE Initial Value Solver, Annals of Numerical Mathematics, **1**, pp. 363-375, 1994.
- [53] Press, W.H., Teukolsky, S.A., Vetterling, T.W., and Flannery, B.P., **Numerical Recipes in C**, Cambridge University Press, New York, N.Y., , 707-724, 1992.
- [54] von Gentsch, H., Ein Verbessertes Omegatron vom Alpert-Typ mit Elektroden

- zum Ableiten der nichtresonanten Ionen., *Vakuum-Technik*, **14**, No. 6, 149-157, 1965.
- [55] Bloom, J.G., and Verwer, J.G., VLUGR3: a vectorizable adaptive grid solver for PDEs in 3D, Part I: Algorithmic aspects and applications., *Applied Numerical Mathematics*, **16**, 129-156, 1994.
- [56] McIver, R.T., ed. Hartmann, H. and Wanczek, K.P., ICR Studies with a One-Region Trapped Ion Analyzer Cell, **Lecture Notes in Chemistry; Ion Cyclotron Resonance Spectrometry**, **7**, pp.97-135, Springer-Verlag Berlin Heidelberg New York, 1978.
- [57] Amerl, P.V. and Irwin, P., Transimpedance amplifiers; an inexpensive alternative for IRMS ion current measurement?, *The International Association of Geochemistry and Cosmochemistry Second International Applied Isotope Geochemistry Symposium*, Lake Louise, Alberta, Canada, 1997.
- [58] Amerl, P.V. and Irwin, P., Quartz crystal stabilized electron emission supply for gas source mass spectrometers., *The International Association of Geochemistry and Cosmochemistry Second International Applied Isotope Geochemistry Symposium*, Lake Louise, Alberta, Canada, 1997.
- [59] Claassen, H.H., **Topics in Modern Chemistry: The Noble Gases**, D.C. Heath and Company, pp. 34-, 1966.
- [60] Asimov, I., **The Noble Gases**, Basic Books, Inc., New York, pp. 96-, 1966.

- [61] Boldyrev, A.I. and Simons, J., Ab initio study of geometrically metastable multiprotonated species:  $MH_n^+$ , J. Chem. Phys., **99**, 769-770, 1993.
- [62] Johns, J.W.C., Spectra of the protonated rare gases, J. Mol. Spectr., **106**, 124-133, 1984.
- [63] Dabrowski, I., Herzberg, G., Hurley, B.P., Lipson, R.H., Vervloet, M., and Wang, D.-C., Spectra of rare gas hydrides; I.  $^2\Pi - ^2\Sigma$  and  $^2\Sigma - ^2\Sigma$  transitions of  $KrH$  and  $KrD$ , Mol. Phys., **63**, No. 2, 269-287, 1988.
- [64] Dabrowski, I. and Herzberg, G., Spectra of rare gas hydrides; II.  $^2\Pi - ^2\Sigma$  and  $^2\Sigma - ^2\Sigma$  transitions of  $XeH$  and  $XeD$ , Mol. Phys., **63**, No. 2, 289-298, 1988.
- [65] Edwards, A.G., Some properties of a simple omegatron-type mass spectrometer, Brit. J. Appl. Phys., **6**, 44-48, 1955.
- [66] Makeev, V.S. and Yastrebov, A.A., and Zhuravlev, G.I., Improved sensitivity in omegatron gas analysis from amplitude modulation of the high-frequency field, Pribory i Tekhnika Eksperimenta, No.5, 138-140, 1973.
- [67] Galkin, M.A. and Fedorov, V.V., Use of an RMO-4S omegatron for determining isotopic composition of nitrogen, oxygen, carbon, and sulfur., Pribory i Tekhnika Eksperimenta, No.5, 191-193, 1976.
- [68] Gertsenshtein, M.E. and Klavdiev, V.V., Relaxing the requirements on magnetic field uniformity for cyclotron resonance in ion beams, Sov. Phys. Tech. Phys, **29**, No. 12, 1386-1387, 1984.

- [69] Berry, C.E., Ion Trajectories in the omegatron, *Journal of Applied Physics*, **25**, No.1, 28-31, 1954.
- [70] Bliven, C.M. and Polanyi, T.G., The removal of nitrogen in an omegatron mass spectrometer, *supplemento al Nuovo Cimento*, **1**, No. 2, 452-457, 1963.
- [71] Rayleigh, J.W.S., Theoretical considerations respecting the separation of gases by diffusion and similar processes., *Phil. Mag.*, **42**, 493-498, 1896.

## Appendix A

### Software Interface for the Omegatron.

The instrument was designed so that the complete data acquisition, apart from the sample preparation and admission, could be performed from the computer control program. Several key concepts must be understood to use the instrument efficiently. The computer interface is programmed for two tasks that can be performed independently. The smaller of these programs is used to calculate the approximate resonance frequencies of ions. The second and larger program is used to control the instrumentation. The omegatron scans a preset region of frequency space and records the ion currents over that region. The reason that frequencies are specified rather than mass numbers is that at this time, the computer interface cannot measure the magnetic flux density and calculate the correct frequency to use for the measurements. To perform a frequency scan, the data program needs a initialization file that contains information on how the data acquisition is to be performed.

#### A.1 Calculating Omegatron Frequencies

The calculation of the frequencies is performed with the program OmCalculator that is shown in Figure A.1. To find the frequency that a given ion will be found at, enter the mass (for  $^{12}\text{C}$  enter 12) and charge of the ion (singly charged=1, doubly charged=2). Also enter the magnetic flux density that is being used for the tests. After performing these steps, click on the circle to the right of the frequency edit

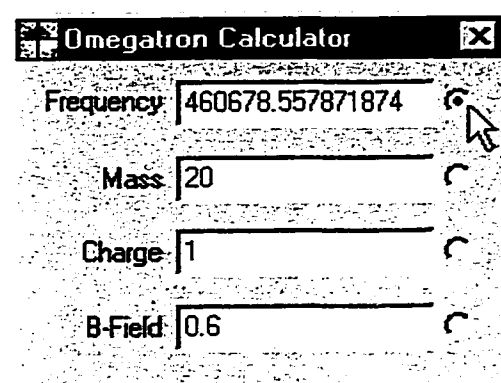


Figure A.1: The omegatron frequency and mass calculator.

box. Calculating the mass of an unknown peak may be performed similarly. One enters the frequency of the peak-center, and then clicks on the circle to the right of the mass specification.

## A.2 Controlling The Omegatron

The screen display presented when the Omegatron Control Center (OCE) is started is shown in Figure A.2. Thereafter one must tell the program which frequencies need to be scanned. This task is accomplished by selecting the initialization command shown in Figure A.3.

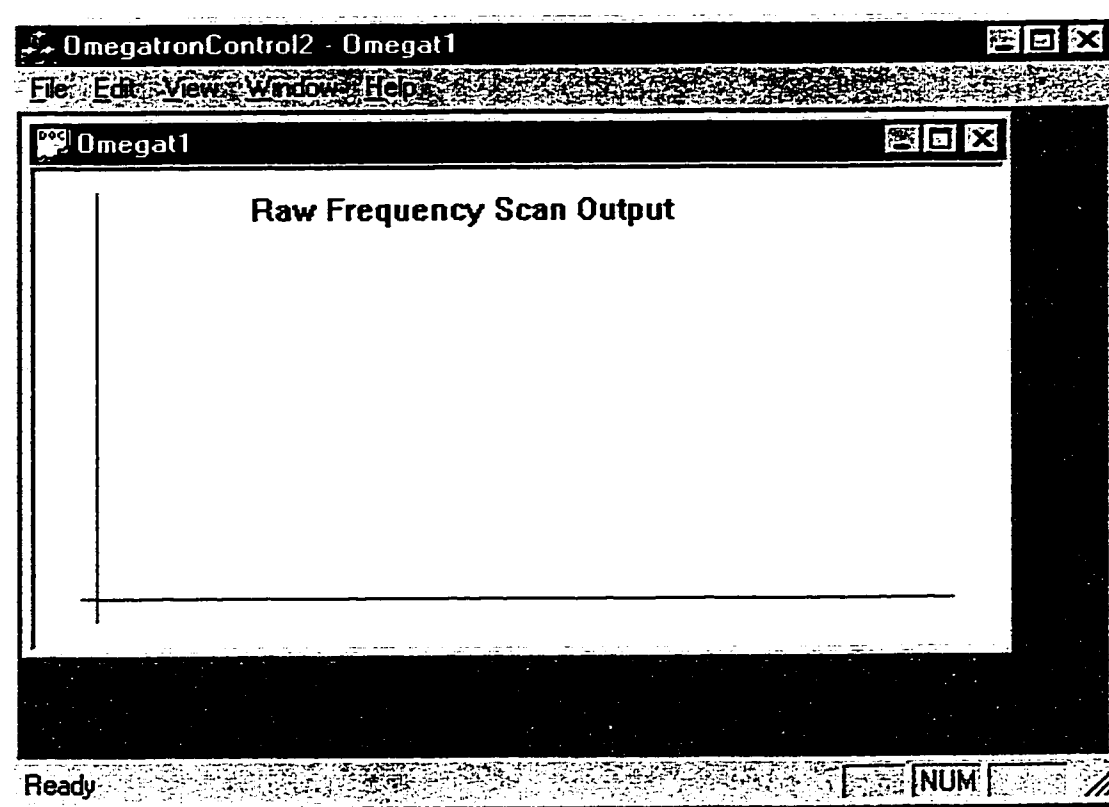


Figure A.2: Data acquisition program just after it has been started.



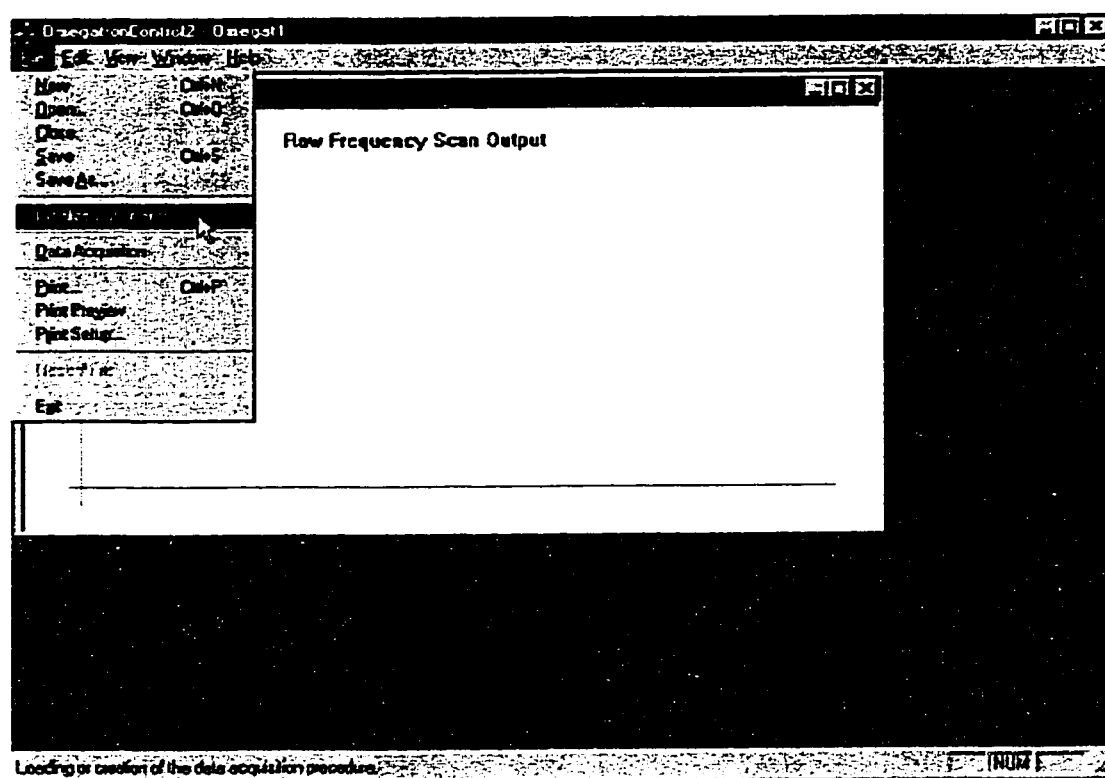


Figure A.3: Starting the initialization of the data acquisition procedure.

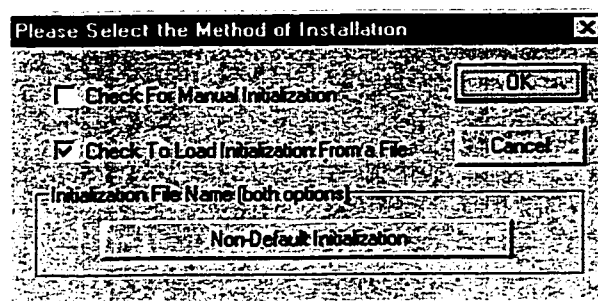


Figure A.4: Display of the dialog box that allows the selection of a manually configured data acquisition procedure, or a previously stored acquisition procedure.

There are two ways that the initialization may proceed. One may enter the data by hand or use an old initialization file by clicking the appropriate check-box. In either case the name by which the initialization file is to be stored must be selected by pressing the “Non-Default Initialization” button shown in Figure A.4. The next dialog box that is visible is shown in Figure A.5. Here the location and name of the initialization should be specified. **Caution!** If manual initialization has been selected previously, then the program will overwrite an old file if you accidentally choose the same file name again.

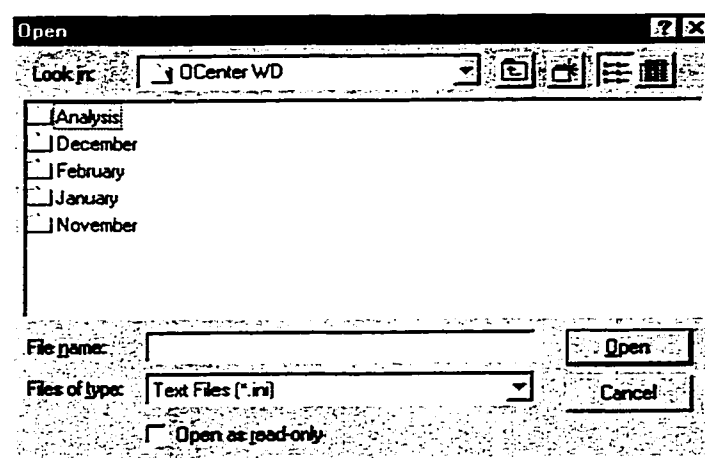


Figure A.5: Selecting the initialization file from the available files. If the file does not exist (manual configuration), it will be created.

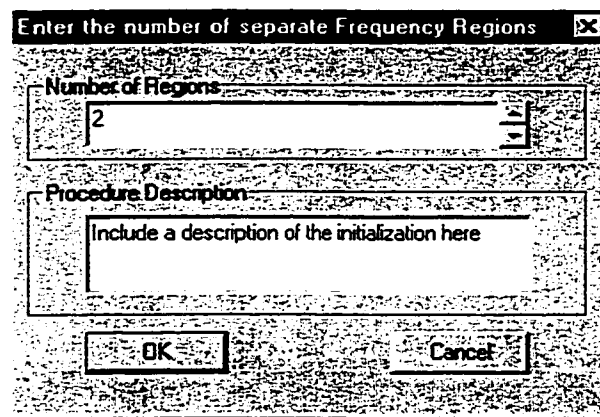



Figure A.6: Specification of the number of frequency ranges. If the same frequency range is to be scanned repeatedly three times, the range should be entered as three regions.

After specifying the filename, and pressing the "OK" button, one will once again see the dialog box shown in Figure A.4. If the manual option has been selected, pressing "OK" will result in the next dialog box shown in Figure A.6. Enter the number of frequency regions that the data acquisition sequence is to have, and a description of the procedure. Then click on the "OK" button. The next view will be of Figure A.7. Here, the frequencies, amplitudes, amplification settings of the voltage to frequency converters, and purging settings must be set.

Please select the Settings for the Frequency Region 

Region Number

Frequency Settings

Starting Frequency

Final Frequency

Frequency Step Size

Step Duration (ms)

Amplifier Gain

☐ 1 x

☒ 5 x

☐ 10 x

☐ 28 x

Amplitude and Grid Offset Settings

Amplitude

Grid Offset

☐ Inverted  
Purging  
Polarity

☐ Ion Purging  
Enabled

Figure A.7: The starting and end frequencies, the frequency step size, amplitude, and other parameters for one frequency sweep are entered using this dialog box.

To start acquiring data, select the “Data Acquisition” option from the “File” menu. This step is shown in Figure A.8. The “Real Time Control” dialog, shown in Figure A.9, will appear on the screen. To start the measurements press the “Start” button. At times it may be convenient to stop a measurement by clicking

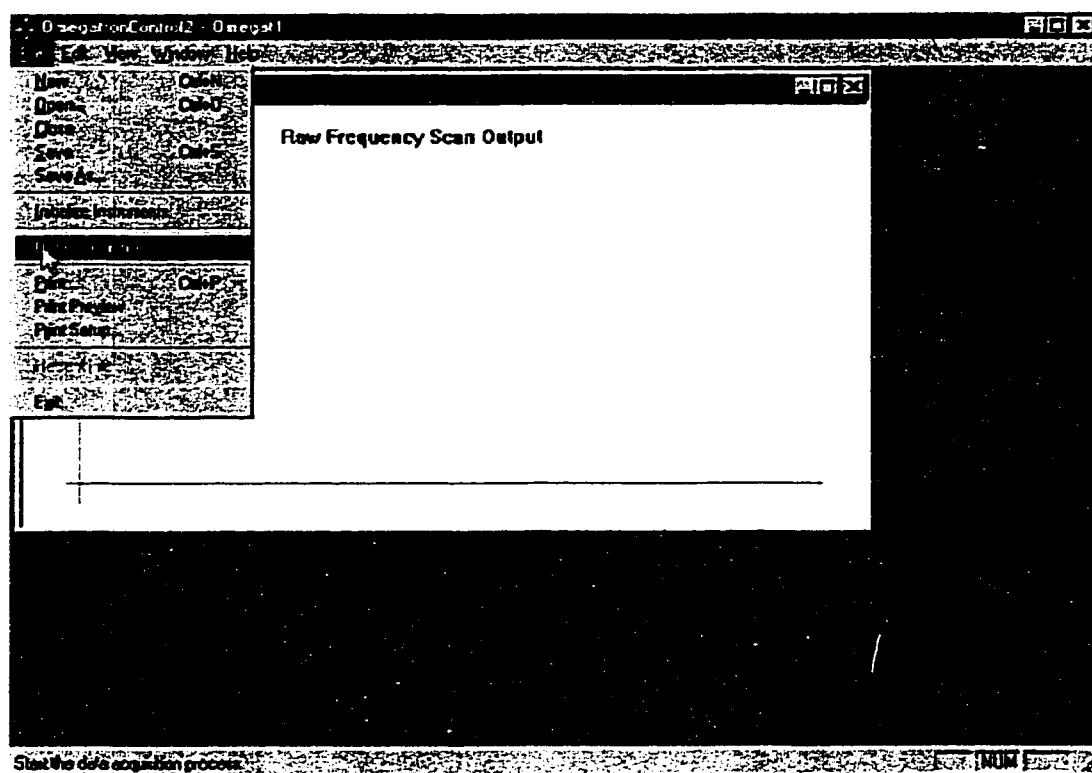


Figure A.8: To start a data acquisition, the Data Acquisition option must be selected from the file menu.

on the “Stop” button. The same measurement may be restarted by clicking the “Start” button again. The buttons labelled “Abort Seg’t” and “Abort Exp’t” will abort a single frequency sweep, and all of the measurements respectively. To save intermediate results while the measurements are being gathered, one may choose the “Save” command under the “File” menu. To save the acquired data after the measurements are complete, click on the “Exit” button and close the document

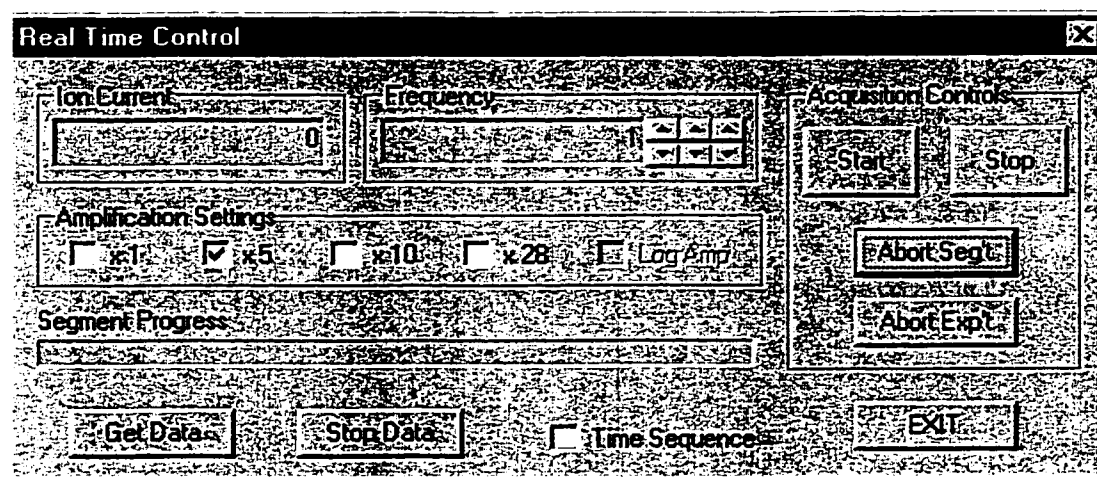


Figure A.9: Control panel that allows direct control of the omegatron. During a data acquisition sequence, the user may intervene to halt the program, abort a segment, or change the voltage to frequency converter gain.

window that displays the raw frequency scan output. Figure A.10 shows the output while measurements are being taken. The graphic display shows the average of the data gathered at each frequency step. Auto-scaling in the vertical dimension is used so that all of the data is displayed at all times. The graph shows the lowest frequency on the left side, and the highest frequency on the right. This scale corresponds to masses decreasing in the direction from left to right.

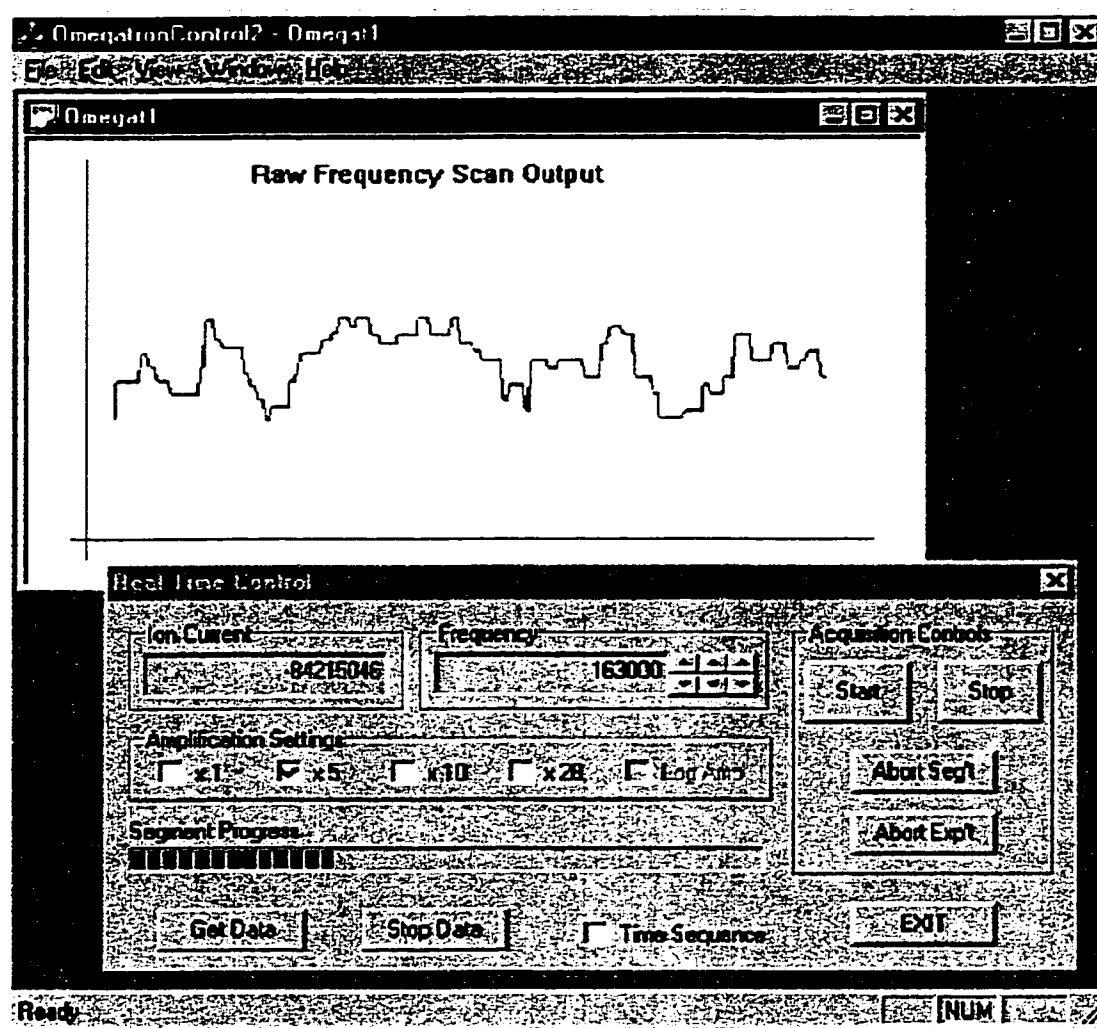


Figure A.10: View of the program as it acquires data. The progress bar shows the current frequency location relative to the end points of the frequency scan.



## Appendix B

### Circuit Diagrams

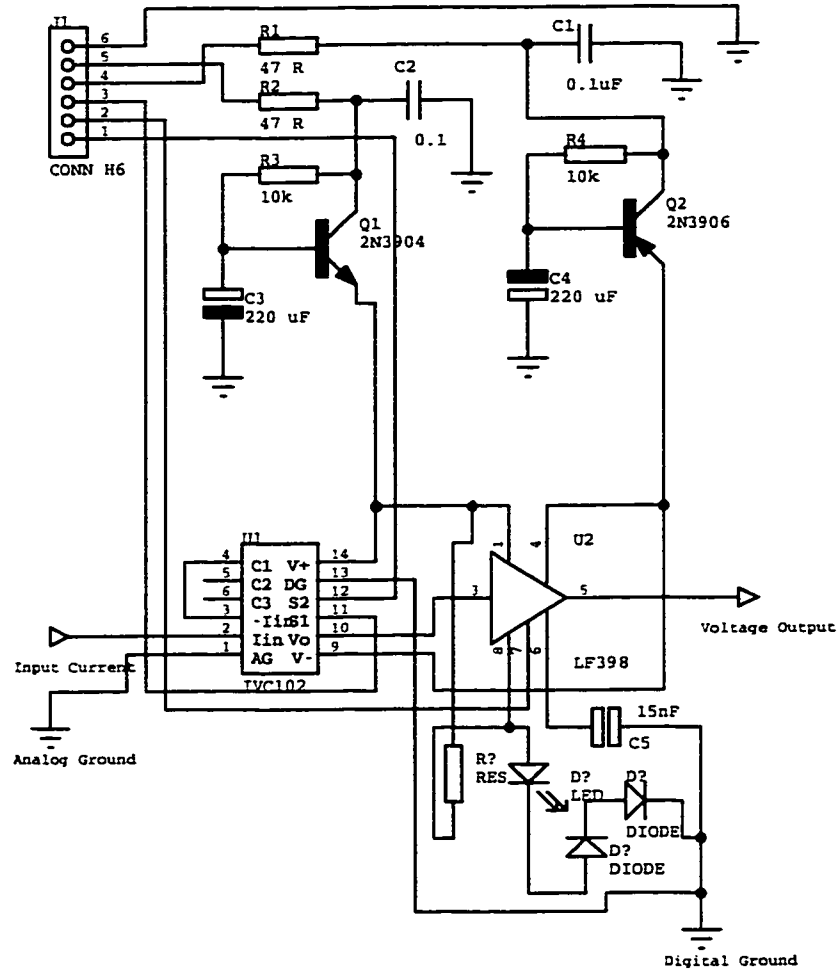


Figure B.1: Schematic diagram of the integrating transimpedance amplifier with a sample-and-hold circuit to give a continuous voltage output.

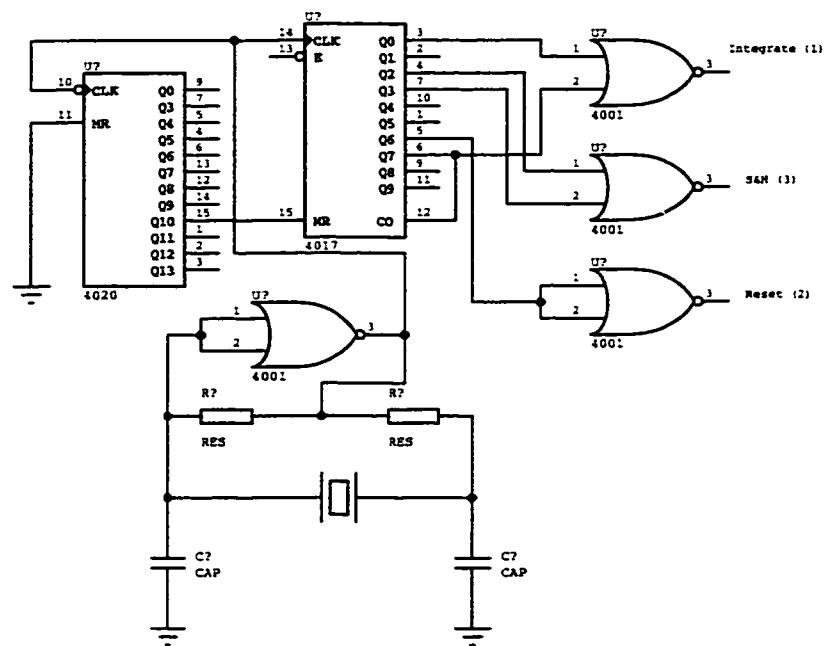


Figure B.2: Switch timing circuit for the integrating transimpedance amplifier.

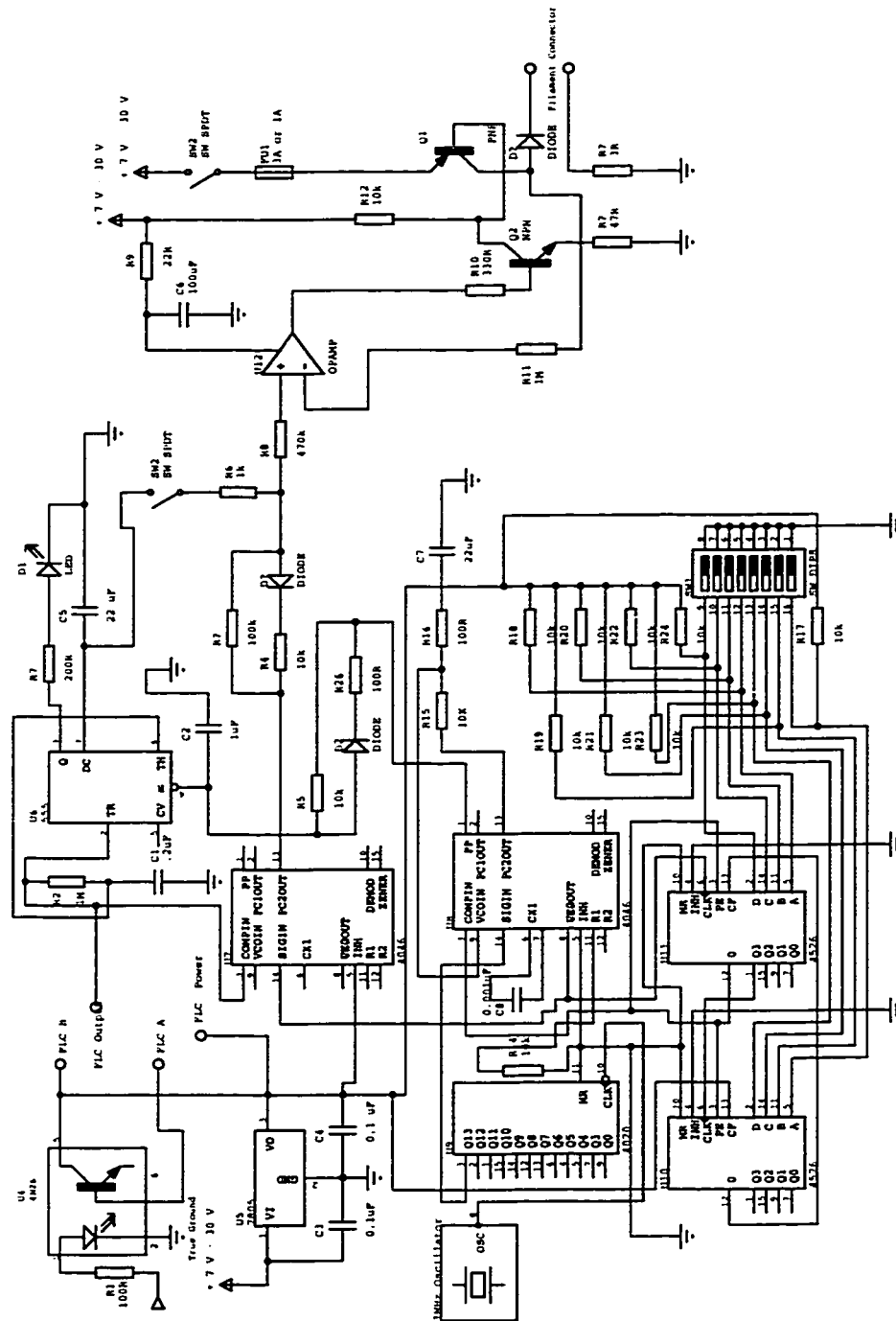


Figure B.3: Electron emission current controller

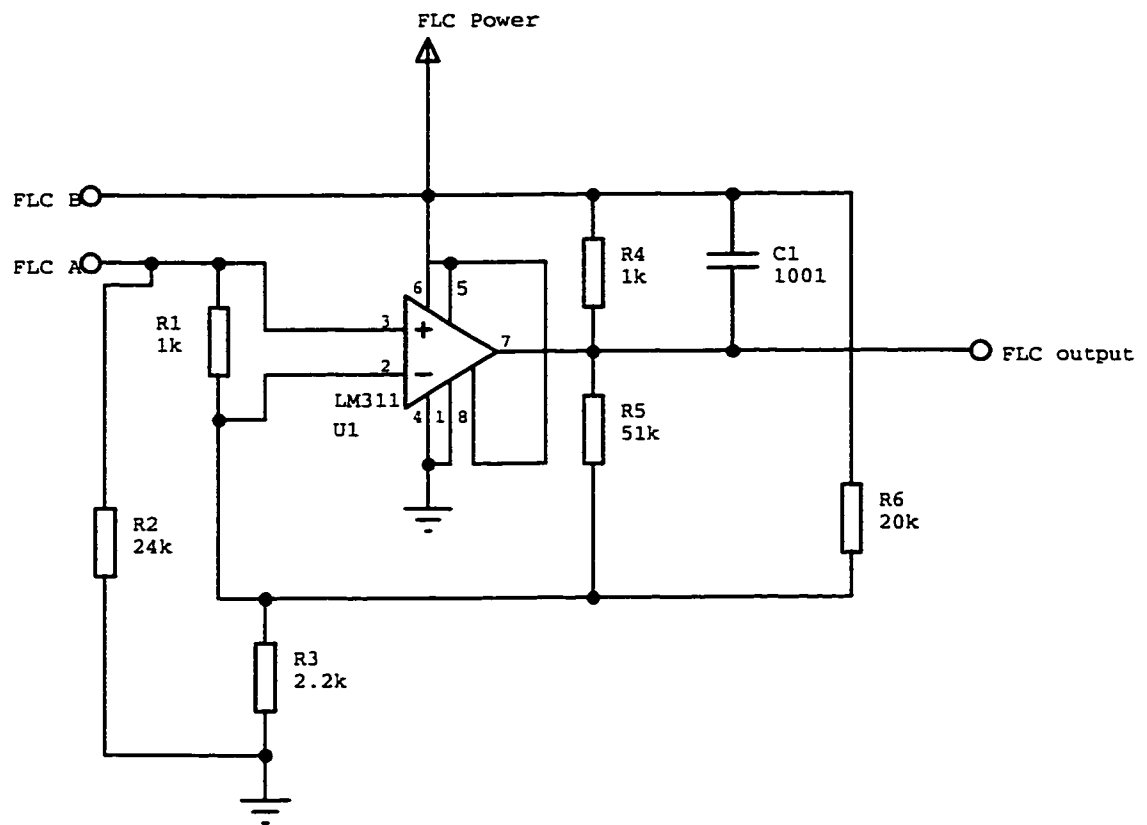


Figure B.4: Feedback signal conditioner for the electron emission supply.

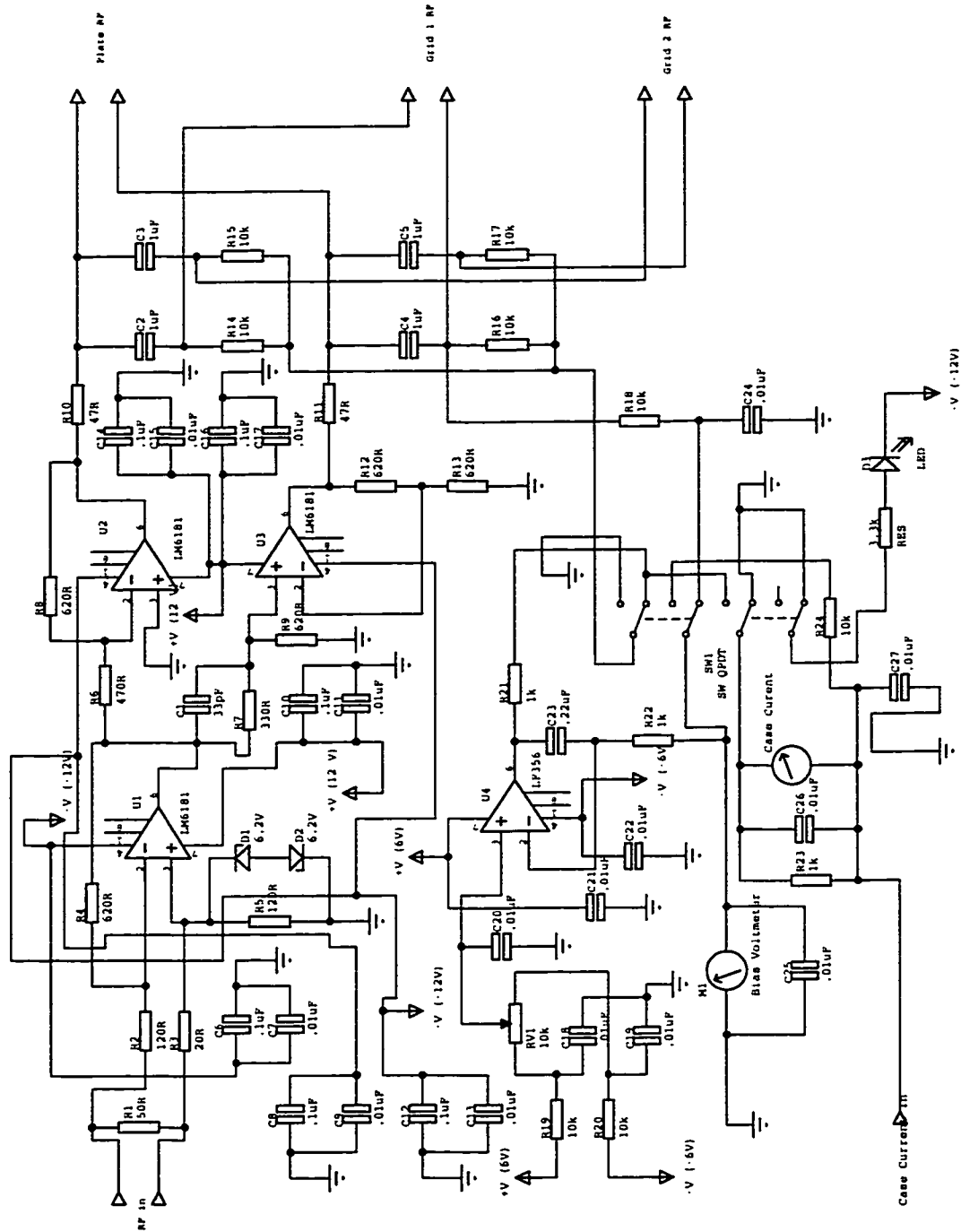


Figure B.5: Radio frequency driver schematic diagram

## **Appendix C**

### **Conference Presentations and Abstracts based on this Thesis**

#### **Short Paper**

Amerl, P.V., Krouse, H.R., Halas, S., and Irwin, P., The omegatron: an improved radio frequency isotope ratio mass spectrometer., RMZ-Materials and Geoenvironment (Formerly Rudarsko-Metalurski Zbornik), **45**, 5-7, 1998.

#### **Conference Presentations**

Amerl, P.V., Krouse, H.R., Halas, S., and Irwin, P., The omegatron: an improved radio frequency isotope ratio mass spectrometer., European Society for Isotope Research., Isotope Workshop IV, Portoroz, Slovenia, July 1-4, 1998.

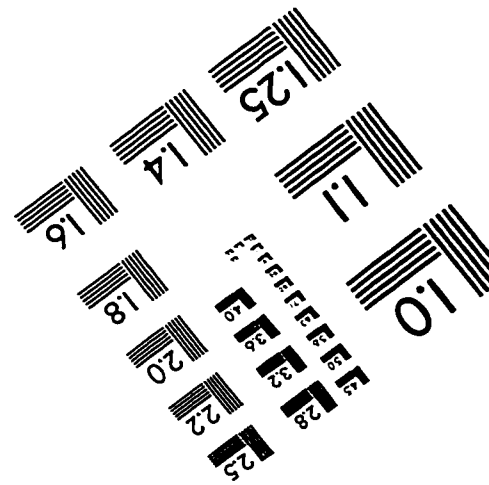
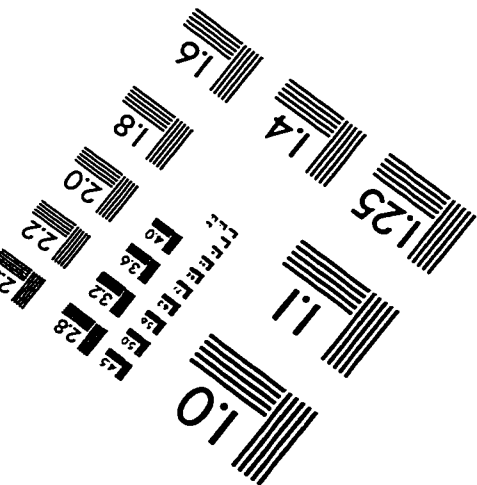
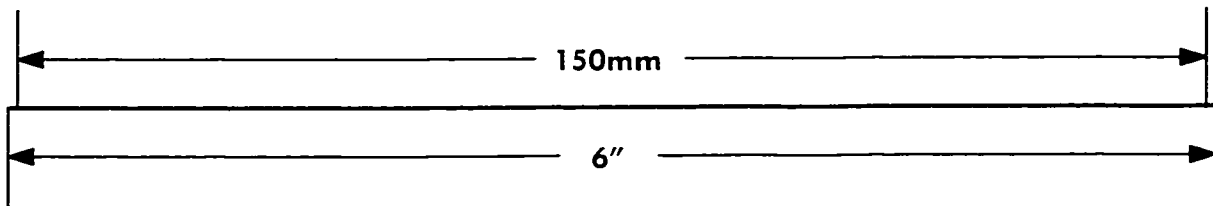
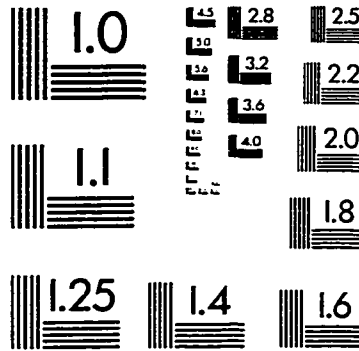
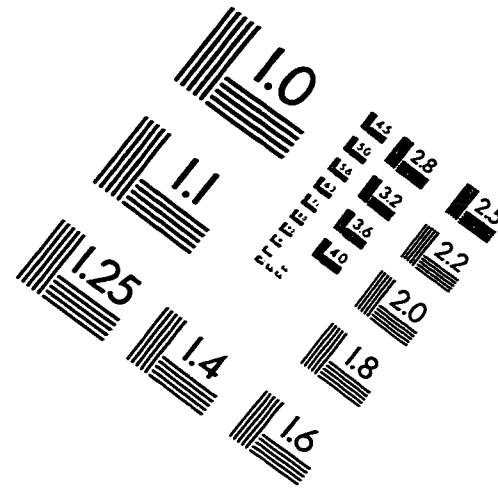
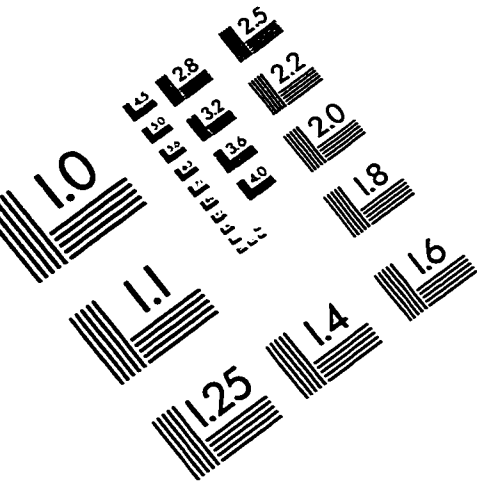
Amerl, P.V. and Irwin, P., Quartz crystal stabilized electron emission supply for gas source mass spectrometers., The International Association of Geochemistry and Cosmochemistry Second International Applied Isotope Geochemistry Symposium, Lake Louise, Alberta, Canada, 1997.

Amerl, P.V. and Irwin, P., Transimpedance amplifiers; an inexpensive alternative for IRMS ion current measurement?, The International Association of Geochemistry and Cosmochemistry Second International Applied Isotope Geochemistry Symposium, Lake Louise, Alberta, Canada, 1997.

Berg, K., Wieser, M., Amerl, P., and Matlock, P., An inexpensive versatile multi-

task PC interface for controlling isotope ratio mass spectrometers and preparation equipment, and data processing., The International Association of Geochemistry and Cosmochemistry Second International Applied Isotope Geochemistry Symposium, Lake Louise, Alberta, Canada, 1997.

# IMAGE EVALUATION TEST TARGET (QA-3)



APPLIED IMAGE, Inc.  
1653 East Main Street  
Rochester, NY 14609 USA  
Phone: 716/482-0300  
Fax: 716/288-5989

© 1993, Applied Image, Inc., All Rights Reserved